Department of Physics and Astronomy, University of Canterbury,
Private Bag 4800, Christchurch, New Zealand

Implementation of 2-Step Intensity Modulated Arc Therapy

Jidi Sun

A thesis submitted in partial fulfilment of the requirements for the degree of Master of Science in the University of Canterbury

2 Feb 2009 – 1 Feb 2010

Supervisor: Dr. Jürgen Meyer
Co-supervisor: Dr. Theam Yong Chew

Abstract

Intensity modulated arc therapy is a novel treatment technique that has shown great potential to be superior to conventional intensity modulated radiotherapy, both in terms of treatment plan quality as well as treatment delivery. Based on previous literature, a simplified technique called two-step intensity modulated arc therapy (2-step IMAT) was implemented into a treatment planning system. In order to automatically generate treatment plans for this technique, a beam portal shaping method was developed to generate beam segments. A sensitivity analysis was carried out on a geometric phantom to determine optimal parameters for the 2-step IMAT implementation for that particular phantom. The segment weights were optimized using the dose-based and dose-volume-based objective functions. The optimal solution search was based on the gradient-descend algorithm. The dose-based objective function was implemented using a so-called lambda-value-dose-based objective function developed in this work in order to increase both speed and flexibility of the optimization. The successful implementation demonstrated the feasibility of automatic 2-step IMAT treatment planning.

A comparison of conventional arc therapy and 2-step IMAT showed improvements in the target dose uniformity by about 50% for both geometric phantom and clinical paraspinal tumor case, whilst also improving the organ sparing. The comparisons between the lambda-value-dose-based and dose-volume-based optimizations showed a speed advantage of the former by a factor of over five in the phantom study.

The current beam portal shaping approach can be improved by optimizing the segment width and including multiple organs-at-risk in the segment generation algorithm. Future work will also include the implementation of a stochastic optimization to minimize the chance of getting trapped in local minima during the segment weight optimization. In summary, the work of this research showed that the automatic 2-step IMAT planning is a viable technique that can result in highly conformal plans while keeping the treatment planning and delivery simple and straightforward.

Acknowledgements

I would like to first thank to my supervisors, Dr. Jürgen Meyer and Dr. Theam Yong Chew for their supervision. Thanks to Dr. Jürgen Meyer for his guidance and for keeping me on track. I also delightedly appreciate his help in the radiotherapy part of this thesis and his help in contacting the University of Washington and the University of Würzburg to setup the treatment planning system and to obtain a clinical case for this research. The discussion with him on the radiotherapy techniques and treatment planning optimization built a foundation of the radiotherapy knowledge for me.

Thanks to Dr. Theam Yong Chew for his help in the programming part of this research, his expertise in Common Lisp language ensured the success of the program developed in this research. I also appreciate the conversation and discussion with him on the topic of computer programming and artificial intelligence areas, which I found quite interesting.

I also would like to thank to the University of Canterbury for providing the equipments and facilities for my research this year. Thanks to the researchers at the University of Washington for developing the Prism Treatment Planning System, which provided a great convenience for the implementation in this research. Also thanks to the researchers at the University of Würzburg for providing a clinical paraspinal tumor case, based on which our implementation was tested.

I appreciate the Department of Physics at the University of Canterbury and the Cancer Society of New Zealand for supporting me to present our work at the EPSM-ABEC Conference in 2009. Thanks also go to James Talbot, a friend who assisted me with the LaTeX writing.

Finally, I would like to give my immense gratitude towards my family members, especially my father and my mother, Ye Sun and Yan Lin. I thank them for providing me the opportunity to study overseas. I appreciate deeply in my heart their financial and emotional supports over these years of my study.

Contents

Abstract i

Acknowledgements iii

Table of Contents v

List of Figures x

List of Tables xi

1 Introduction 1
- 1.1 Conformal Radiotherapy . . . 1
- 1.2 Intensity Modulated Radiotherapy . . . 2
- 1.3 Intensity Modulated Arc Therapy . . . 5
- 1.4 2-Step Intensity Modulated Arc Therapy . . . 6
- 1.5 Outline of Thesis . . . 8

2 Treatment Planning System 9
- 2.1 PRISM . . . 9
- 2.2 2-Step IMAT Implementation . . . 10
  - 2.2.1 Graphical User Interface . . . 11
  - 2.2.2 Beam Portal Generation . . . 12
  - 2.2.3 PTV Coverage . . . 14
- 2.3 Concluding Remarks . . . 16

3 Optimization 18
- 3.1 Introduction . . . 18
- 3.2 Volume Definition . . . 19
- 3.3 Dose Calculation . . . 20
- 3.4 Objective Function Definition . . . 21
  - 3.4.1 Dose-Volume Objectives . . . 21
  - 3.4.2 Lambda Optimization Algorithm . . . 24
- 3.5 Optimal Solution Search Algorithm . . . 28
- 3.6 Implementation in MATLAB . . . 29

3.7 Prism and MATLAB Data Interaction 30
3.8 Concluding Remarks 31

4 Analysis of Setup Parameters **32**
4.1 Phantom 32
4.2 Grid Size Analysis 33
4.3 Angle Step Size Analysis 38
4.4 Segment Weight Ratio Analysis 43
4.5 Second Segment Width Analysis 45
4.6 Rotation Number Analysis 48
4.7 Concluding Remarks 51

5 Segment Weight Optimization **53**
5.1 Aim 53
5.2 Method 53
5.3 Results and Discussion 54
5.4 Concluding Remarks 60

6 Clinical Study **62**
6.1 Method 62
6.2 Results and Discussion 63
6.3 Concluding Remarks 71

7 Discussion and Conclusion **72**
7.1 Discussion and Future Work 72
7.2 Conclusion 74

A EPSM-ABEC Conference Abstract **76**

References **81**

List of Figures

1.1 MLC conforms around the target in the BEV to form the beam portal (or aperture). 2
1.2 Illustration of 1D modulated beam intensity profiles in an IMRT treatment. The intensity modulated radiation beams are delivered to the prostate from three possible gantry angles in this cross section image [1]. 3
1.3 Illustration of continuous 2D intensity map. The intensity contour map in the BEV with four levels can be generated with four beam fields [2]. 4
1.4 Discrete 2D intensity matrix. There are three intensity levels in this nine element matrix. 4
1.5 Three possible beam fields combination consisting of three segments. Each combination generates the same 1D intensity profile as shown in (a) [3]. . . . 5
1.6 Illustration of (a) 2-step IMAT beam segmentation and (b) intensity profile. Reproduced based on Bratengeier's literatures [4]. 6
1.7 Photon beam is modulated by a filter before irradiating the cylindrical target [5]. 7
1.8 Intensity profile and dose distribution comparison of without (left) and with (right) filter modulation [5]. (Curve 1 is the beam intensity profile, curve 2 is the dose distribution and curve 3 is the fractional dose contribution resulted by the filter). 7

2.1 A desktop screenshot with some of the Prism TPS panels. 11
2.2 The GUI developed in this work to automatically generate 2-step IMAT treatment plan. 12
2.3 An illustration of the ray-tracing technique for beam portal generation. The leftside diagram shows the organ layout in the beams-eye-view with uniform points matrix (black points are within the PTV and white points are outside the PTV). The rightside diagram shows the transversal view of the setup. It can be seen from the left diagram that the spatial resolution of the point matrix influences the determination of the MLC setup [6]. 13
2.4 Illustration of the 2-step IMAT beam portal setup. The left diagram shows a transversal plane of the PTV, the OAR and the radiation beam. The right diagram shows the beams-eye-view. The PTV and OAR points are the boundary points on the corresponding contours, and the MLC leaves are pushed to these points to form a beam portal which provides the beam shown on left. . 15

2.5 Illustration of the ideal beam intensity profiles. The geometry shown here provides two possible beam portals at this gantry angle, each portal is on one side of the OAR. Ideally, one wants to deliver both portals at the same time to reach the maximum efficiency and dose coverage [7]. 15
2.6 Graph of the beam intensity versus gantry angle and MLC position in an ideal arc therapy. The purpose of the middle sine wave shape intensity valley is in order to spare the OAR [7]. 17
2.7 Graph of the beam intensity versus gantry angle and MLC position in a sinlge-arc therapy. Since only one side of the intensity "bank" can be delivered during one rotation, the other side of the intensity "bank" becomes null as the MLC leaves shadows from the edge of the OAR [7]. 17

3.1 A discrete 3D matrix is created surrounding the organ, the voxels whose center points are located within the organ contour are used to represent the partial volume of the organ and the dose deposited into those voxels are the dose received by that organ. 20
3.2 Ideal PTV and OAR DVH curves (1 & 2) and typical real PTV and OAR curves (3 & 4). 22
3.3 Three points can be used in the dose-volume-based optimization to increase the PTV dose uniformity and the OAR sparing. 22
3.4 Illustration of the implementation of the dose-volume objective point in the optimization. 23
3.5 The conventional dose-based optimization penalizes the full dose range on the DVH. The d_{pres} in this example is the prescribed tolerant dose to the OAR. . 25
3.6 Illustration of the dose penalization using the lambda-value-dose-based objective function. The algorithm penalizes (a) the doses greater than the prescribed dose in order to reduce hot spot in an organ and (b) the doses less than the prescribed dose in order to reduce the cold spot in an organ. λ is the ratio of $d_n - d_{pres}$ to $d_{max} - d_{pres}$ in (a) and $d_{pres} - d_n$ to $d_{pres} - d_{min}$ in (b). 25
3.7 Illustration of the dose-volume-based and lambda-value-dose-based objective function optimization. The difference lies on the calculation of the value d_n to determine the dose range in the objective function calculation. 27
3.8 A randomly generated one-variable, non-convex function with the global minimum at $x = 7$. 29
3.9 The flowchart to illustrate the working structure of the complete treatment plan generation process in both Prism and MATLAB. 31

4.1 Transverse view of the geometric phantom (yellow: PTV, red: OAR, green: external contour). (Regenerated based on Bratengeier's paper [4]). 33
4.2 The number of points inside the PTV and the dose calculation time versus voxel sizes from $0.4cm$ to $2.5cm$. 35
4.3 The dose calculation time and the RMS difference versus PTV voxel size. . . 36
4.4 The number of points inside the OAR and the normalized matrix calculation time versus voxel size. 36

4.5 OAR DVHs plotted using the voxel sizes from $0.2cm$ to $0.5cm$. Although about 5cGy difference of the maximum OAR dose between the $0.2cm$ and $0.4cm$ DVHs, the $0.4cm$ is the smallest OAR voxel size that does not run out of memory during the calculation involving both the PTV and the OAR. . . 37
4.6 The normalized matrix calculation time and the RMS versus OAR voxel size. 37
4.7 Comparison between the RMS difference of the PTV and the OAR. 38
4.8 Dose calculation time and the number of beams decreases as the angle step size increases. 40
4.9 The homogeneity indices approach unity as the angle step size decreases. . . 40
4.10 The homogeneity index difference approaches to approximately zero as the angle step size decreases. 41
4.11 Graph of dose calculation time versus homogeneity index difference. The homogeneity index difference does not improve much as the angle step size smaller than 5°. 41
4.12 DVH comparison between 2° and 5°. (100% dose =100cGy) 42
4.13 DVH comparison between 5°, 10° and 15°. 42
4.14 Linear relationship between the total MU and the segment weight ratio. . . . 44
4.15 Decrease of the PTV mean dose as the segment weight ratio increases. . . . 44
4.16 Changes in the HI_{max} and HI_{min} as the beam segment ratio increases. 45
4.17 The difference of HI_{max} and HI_{min} as a function of beam segment ratio. . . . 45
4.18 Decreasing trend of the total MU as the second segment width increases. . . 46
4.19 Mean PTV dose versus the second segment width. 47
4.20 OAR mean dose decreases as the second segment width increases. 47
4.21 Effects of the change in second segment width on the homogeneity indices. . 48
4.22 DVH comparison between the $1.5cm$ and $1.8cm$ 2^{nd} segment width plans. (100% dose =100cGy) 48
4.23 The "single side" plan (a) only irradiates one side of the PTV, while the "double side" plan (b) irradiates both sides of the PTV. For a 2-step IMAT, each segment requires one gantry rotation to deliver. 49
4.24 PTV and OAR DVH comparison of the "single side" and "double side" treatment plans. (100% dose =100cGy) 50
4.25 Dose distribution of the "single side" plan (a) and the "double side" plan (b). The improved symmetry can be observed. (red: 107cGy, green: 100cGy, blue: 95cGy, white: 90cGy, purple: 75cGy, yellow: 50cGy, cyan: 30) 51
4.26 The dose distribution of a 2-step IMAT treatment plan from Bratengeier's paper [4]. The asymmetrical distribution of 70% to 80% isodose lines can be observed. 51

5.1 DVH comparison between non-optimized plan and the plan optimized using dose-based objective function. ($\lambda = 1$) (100% dose =100cGy) 55
5.2 DVH comparison between non-optimized plan and the plan optimized using dose-volume-based objective function. (100% dose =100cGy) 55
5.3 MU distribution of the plan optimized using the dose-volume-based objective function. 56

5.4 MU distribution of the plan optimized using the dose-based objective function. ($\lambda = 1$) 56
5.5 MU difference of the dose-volume-based and dose-based optimization. 57
5.6 Dose distribution of the dose-volume-based optimized plan. (red: 107cGy, green: 100cGy, blue: 95cGy, white: 90cGy, purple: 75cGy, yellow: 50cGy, cyan: 30) 57
5.7 Dose distribution of the dose-based optimized plan ($\lambda = 0.5$). (red: 107cGy, green: 100cGy, blue: 95cGy, white: 90cGy, purple: 75cGy, yellow: 50cGy, cyan: 30) 58
5.8 Dose distribution of the dose-based optimized plan ($\lambda = 1$). (red: 107cGy, green: 100cGy, blue: 95cGy, white: 90cGy, purple: 75cGy, yellow: 50cGy, cyan: 30) 58
5.9 DVH comparison between dose-volume-based optimized plan and the plan optimized using dose-based optimization. ($\lambda = 0.5$) (100% dose =100cGy) . 59
5.10 DVH comparison between the plans optimized using dose-based optimization. ($\lambda = 0.5$ and $\lambda = 1$) (100% dose =100cGy) 59
5.11 DVH comparison between the plans optimized using dose-based optimization ($\lambda = 0.5$) with different weighting factor settings. (100% dose =100cGy) . . . 60
5.12 Dose distribution of the dose-based optimized plan ($\lambda = 0.5$, $\omega_{PTV} = 0.7$ and $\omega_{OAR} = 0.3$). (red: 107cGy, green: 100cGy, blue: 95cGy, white: 90cGy, purple: 75cGy, yellow: 50cGy, cyan: 30) 61

6.1 The transverse view of the PTV (cyan contour) and the spinal cord (green contour). 62
6.2 DVH comparison between the conventional arc therapy, 2-rotation and 4-rotation 2-step IMAT plans optimized by dose-volume-based objective function. 64
6.3 DVH comparison between the conventional arc therapy, 2-rotation and 4-rotation 2-step IMAT plans optimized by lambda-value-dose-based objective function. (λ=0.5) 65
6.4 DVH comparison between the conventional arc therapy, 2-rotation and 4-rotation 2-step IMAT plans optimized by lambda-value-dose-based objective function. (λ=1) 65
6.5 Dose distribution of the conventional arc therapy in the transverse plane. (red: 107cGy, green: 100cGy, blue: 95cGy, white: 90cGy, purple: 75cGy, yellow: 50cGy, cyan: 30) 66
6.6 Dose distribution of the 2-rotation 2-step IMAT in the transverse plane. (red: 107cGy, green: 100cGy, blue: 95cGy, white: 90cGy, purple: 75cGy, yellow: 50cGy, cyan: 30) 67
6.7 Dose distribution of the 4-rotation 2-step IMAT in the transverse plane. (red: 107cGy, green: 100cGy, blue: 95cGy, white: 90cGy, purple: 75cGy, yellow: 50cGy, cyan: 30) 67
6.8 Dose distribution of the conventional arc therapy in the coronal plane. (red: 107cGy, green: 100cGy, blue: 95cGy, white: 90cGy, purple: 75cGy, yellow: 50cGy, cyan: 30) 68

6.9 Dose distribution of the 2-rotation 2-step IMAT in the coronal plane. (red: 107cGy, green: 100cGy, blue: 95cGy, white: 90cGy, purple: 75cGy, yellow: 50cGy, cyan: 30) 68
6.10 Dose distribution of the 4-rotation 2-step IMAT in the coronal plane. (red: 107cGy, green: 100cGy, blue: 95cGy, white: 90cGy, purple: 75cGy, yellow: 50cGy, cyan: 30) 69
6.11 Dose distribution of the conventional arc therapy in the sagittal plane. (red: 107cGy, green: 100cGy, blue: 95cGy, white: 90cGy, purple: 75cGy, yellow: 50cGy, cyan: 30) 69
6.12 Dose distribution of the 2-rotation 2-step IMAT in the sagittal plane. (red: 107cGy, green: 100cGy, blue: 95cGy, white: 90cGy, purple: 75cGy, yellow: 50cGy, cyan: 30) 70
6.13 Dose distribution of the 4-rotation 2-step IMAT in the sagittal plane. (red: 107cGy, green: 100cGy, blue: 95cGy, white: 90cGy, purple: 75cGy, yellow: 50cGy, cyan: 30) 70

List of Tables

4.1 Results for the PTV with voxel sizes between $0.3cm$ and $2.5cm$. The calculation time of $0.3cm$ voxel size is missing because the computation run out of memory. . . . 35
4.2 Results of the OAR with voxel sizes between $0.2cm$ and $2.0cm$. . . . 35
4.3 Results of the angle step analysis. . . . 39
4.4 Results of the segment weights ratio analysis. . . . 43
4.5 Results of the second order beam segment width analysis. . . . 46
4.6 Results of the rotation number analysis. . . . 50

5.1 Dose-volume-based objective parameters setup. Name of parameters refers to Equations 3.5-3.7. . . . 53
5.2 The lambda-value-dose-based objective function parameter setup, the value of λ is set to 1 or 0.5. . . . 54
5.3 Results of the non-optimized plan (Non-Opt) and the plans optimized using dose-volume-based optimization (DV Opt) and dose-based optimization (D Opt). . . . 54
5.4 Results of plans optimized using dose-based optimization ($\lambda = 0.5$) with different weighting factor setups. . . . 60

6.1 Dose-volume-based objective function parameters setup. Name of parameters refers to Equations 3.5-3.7. . . . 63
6.2 The lambda-value-dose-based objective function parameter setup, the value of λ is set to 1 or 0.5. . . . 63
6.3 Conventional arc therapy after the dose-volume-based optimization and dose-based optimizations. . . . 63
6.4 2-rotation 2-step IMAT treatment plan after the dose-volume-based and dose-based optimizations. . . . 64
6.5 4-rotation 2-step IMAT treatment plan after the dose-volume-based and dose-based optimizations. . . . 64

Chapter 1

Introduction

Ionizing radiation is one of main methods currently used to treat cancer. Unlike surgery and chemotherapy, radiation therapy is neither invasive nor painful to the patients. Nearly all types of cancer are treated with radiotherapy as the sole or adjuvant treatment method to eliminate cancer cells [8]. The linear accelerator (linac) is most commonly used to deliver photon or electron beams to the patient [9, 10, 11]. In this work only photon therapy will be considered. During the radiation treatment, the patient lies on a treatment table and the linac irradiates the patient from different angles. To reduce treatment errors due to patient movement, the patient may be immobilized by e.g. a vacuum bag, a frame or masks during the treatment. Using highly attenuating material, the radiation beams are shaped individually to the shape of the target volume in the beams-eye-view (BEV). Thus, irradiation to radiosensitive organs is blocked to minimize the complications, thus prolonging the lifespan of the patient. Common radiation treatment techniques include conformal radiotherapy, intensity modulated radiotherapy and intensity modulated arc therapy. Each technique will be introduced in the following sections.

1.1 Conformal Radiotherapy

The aim of the conformal radiotherapy (CRT) is to irradiate the tumor uniformly while at the same time keeping the normal tissue exposure to a minimum level. Originally, the radiation beams were shaped using physical cerrobend blocks [2, 11]. The shape of the beams, and hence the cerrobend blocks are patient specific. As the shape of the target in the BEV changes while the linac gantry rotates to different angles, it is impractical to manufacture different block shapes for each beam and each patient. In modern treatments the cerrobend blocks are replaced by the multi-leaf collimator (MLC) mounted onto the linac. The MLC consists of two banks of attenuating leaves, typically made of tungsten, that slide parallel to each other. By sliding each individual leaf towards or away from its opposing leaf, the device is able to form irregular shapes as shown in Figure 1.1. The advantage of using an MLC over conventional blocks is that the MLC has the ability to change the beam shape to most irregular shapes freely during the treatment. Therefore, the process of manufacturing individual blocks is eliminated. This makes it a more practical approach when the beams are delivered from different angles and the target is irregularly shaped. An initial survey conducted by Klein *et al* showed that more than one third of facilities that

used MLC, suggested that they could treat more patients with MLC machines and more than 90 percent facilities could reduce the workload of therapist [12].

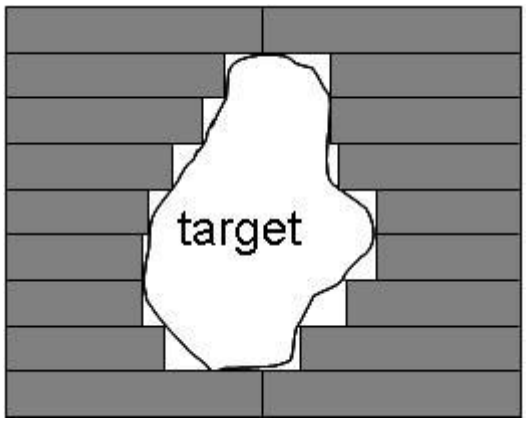

Figure 1.1: MLC conforms around the target in the BEV to form the beam portal (or aperture).

The conformal radiation treatment using MLC was introduced by Takahashi in 1965 [13]. The beams are shaped around the tumor depending on the geometry of the organs and the beam angle. The radiation treatment using the 3D organ information to shape the beams is called the 3-dimensional conformal radiotherapy (3D CRT). The availability of three-dimensional (3D) volumetric information of the organs from the modern imaging modalities increases the accuracy of the MLC setup.

Typically a certain number of beam directions are used for treatment. The beam arrangements are based on the experience of the clinician. It may be optimized manually or automatically [6]. In this so-called "forward planning" process, the beam portals are firstly generated. During this process, the planner then changes the relative beam weight of each beams by the trial-and-error method in order to achieve a conformed treatment plan. 3D CRT is able to reduce the radiation damage to the healthy tissues better than the conventional techniques without 3D volume information. However, with a uniform beam intensity profile of each beam it is sometimes difficult to deliver a conformal dose distribution around the target tumor whilst at the same time spare the normal tissues. In particular, if the target volume is concavely shaped and a radiosensitive organ is located in the concave region of the tumor, healthy tissue sparing has to be compromised in order to achieve a reasonable tumor dose coverage. This in turn limits the dose that can be safely delivered to the tumor. In this situation, uniform beams are not sufficient and beam intensity modulation may be required.

1.2 Intensity Modulated Radiotherapy

Intensity modulated radiotherapy (IMRT) is an advanced form of 3D CRT. For IMRT, treatment plan is generated using "inverse planning" method. Rather than manually trying different beam weights to find a desired dose distribution, the plan objectives are initially defined and an ideal fluence distribution of the beam intensity is obtained.

The most significant feature of IMRT is that the beam intensity at each angle is modulated to achieve a conformal dose distribution in the target volume. Figure 1.2 shows an example of the treatment of prostate cancer using IMRT from three angular directions. Note that the three beam directions are only used to illustrate the principle of IMRT, different angle combinations would be used clinically. The target in this case is a tumor with two concave regions, each of which is adjoined by a radiosensitive organ, the bladder and the rectum. In order to maximize the sparing of the healthy tissues, the intensity profiles of the three beams are modulated as shown in Figure 1.2. Since there is no critical tissue on its path, the beam irradiating from the lateral side of the patient has a high peak profile so that the prostate receives maximum radiation from this angle. In contrast, the anterior beam has low intensity at the center of the profile in order to reduce the radiation delivered to the rectum. In summary, the intensity profiles from all gantry angles are modulated differently so that the target receives a conformal dose whilst the healthy tissues are spared.

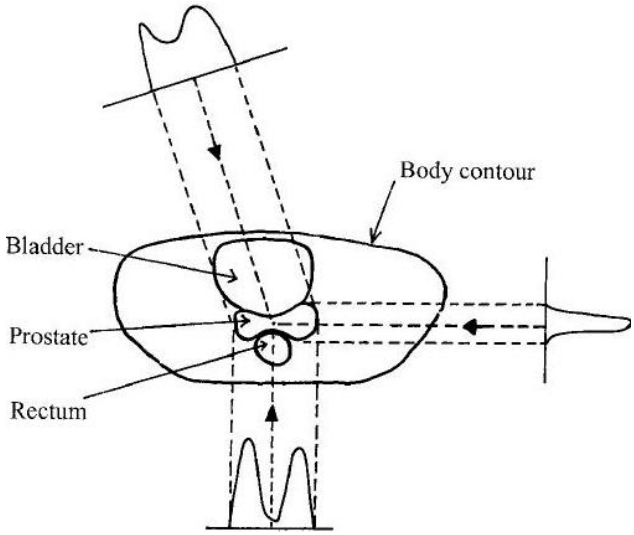

Figure 1.2: Illustration of 1D modulated beam intensity profiles in an IMRT treatment. The intensity modulated radiation beams are delivered to the prostate from three possible gantry angles in this cross section image [1].

The MLC plays an important role in generating non-uniform intensity profiles during IMRT treatment. In Figure 1.2 ideal 1D intensity profiles are shown for one cross section of the patient. In the BEV, the intensity profile is a 2D distribution as shown on the right side of Figure 1.3. The intensity profile in Figure 1.3 can be delivered through four different beam segments. Each beam segment is shaped using the MLC in order to deliver the contour of each intensity level. To approximate the continuous 2D intensity contour map, a discrete representation is used (see Figure 1.4). The matrix is a discrete representation and each unit area (or element of the matrix) is called "bixel". The intensity profile of the beam is approximated by assigning each bixel with an intensity value, each represents the height of the intensity in the perpendicular direction from the 2D plane. The matrix is then used as a guide for the MLC to shape beam segments in order to produce a desired 2D intensity profile.

The non-uniform intensity profile characteristic of IMRT is able to produce a more conformal dose distribution while sparing healthy tissues. This achievement comes with the

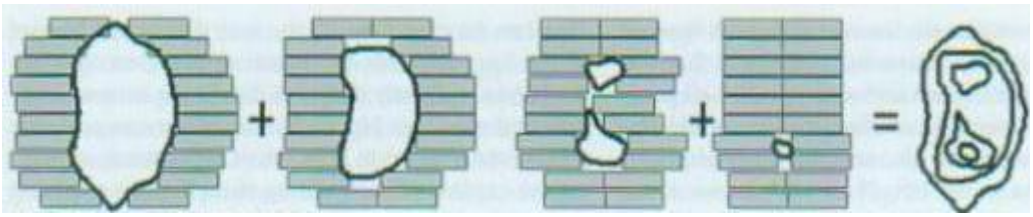

Figure 1.3: Illustration of continuous 2D intensity map. The intensity contour map in the BEV with four levels can be generated with four beam fields [2].

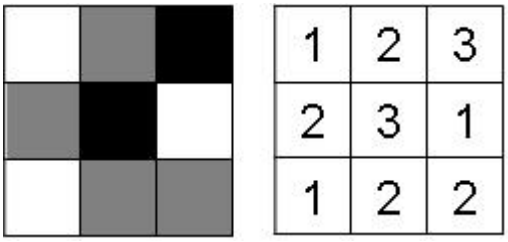

Figure 1.4: Discrete 2D intensity matrix. There are three intensity levels in this nine element matrix.

compromise of complicating the planning process. In order to achieve a given intensity profile, there are many possible solutions to setup the beam fields for each intensity level. One simple illustration is shown in Figure 1.5 [3]. In the same paper, Yu derived that for a single-peak profile, there are $(N!)^2$ possible MLC beam field setups in a one-dimensional case with N intensity levels. The figure shows three of thirty-six possible beam field setups in order to achieve the same intensity profile for one pair of the MLC leaves. The possible solutions will increase when considering a two-dimensional intensity map (all pairs of the MLC leaves) and the problem will become more complicated as certain physical restrictions of the MLC setup need to be taken into account, such as the maximum overtravel distance of the MLC [2]. In addition, the complexity of the intensity maps complicates the treatment plan physically. The more intensity levels a beam profile has the more beam segments are required to generate such a profile, thus the larger the beam penumbra effects on the quality of the treatment plan [11, 14].

Comparing conventional 3D CRT and IMRT, the former is simpler in planning and delivery, thus the time to plan and deliver is shorter. On the other hand, IMRT is able to create more sophisticated quality plans, especially in complicated cases that involve a concave-shaped target. However, the compromise of a more conformal IMRT plan is the longer time for planning and delivery and so is the higher equipment requirements. In order to reduce the treatment time and improve the efficiency of the treatment delivery, a rotational irradiation technique was developed and has recently become available commercially. Both Varian (Palo Alto, USA) and Elekta (Stockholm, Sweden), have implemented the so-called "intensity modulated arc therapy" and branded it as $RapidArc^{TM}$ and VMAT (Volumetric Modulated Arc Therapy), respectively.

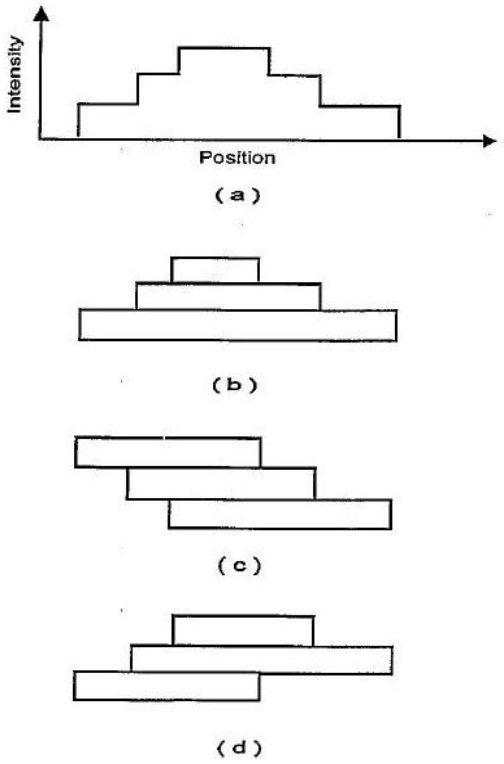

Figure 1.5: Three possible beam fields combination consisting of three segments. Each combination generates the same 1D intensity profile as shown in (a) [3].

1.3 Intensity Modulated Arc Therapy

Intensity modulated arc therapy (IMAT) was first introduced by Yu in 1995 [3]. IMAT is a rotational treatment, which irradiates the target while the gantry rotates around the patient. The beam segments and even the dose rate may be changed continuously [15, 16, 17]. Both the shape and the relative weight of each segment are obtained from inverse planning. Unlike conventional 3D CRT and IMRT with limited number of fixed gantry angles, radiation is continuously delivered during gantry rotation in the IMAT treatment [15, 16]. This provides a more completed directional coverage of the target.

Although the overall benefit of IMAT over the former two techniques is still subject of debate [7, 15, 18, 16, 19, 20], there are two definite advantages of the IMAT technique. The continuous irradiation during the gantry rotation is more efficient than the IMRT techniques in terms of radiation delivery. Recent studies have showed the delivery time advantage of IMAT over IMRT for different treatment sites [21, 22, 23, 24]. For example, a study done by Cozzi *et al* compared IMRT and $RapidArc^{TM}$ for treating cervical cancer. Their work showed that IMRT may take as long as 15 minutes to deliver one fraction of radiation treatment, while IMAT only required one to two minutes to do so [21]. Furthermore, the increased number of irradiating angles reduces the intensity modulation required for each beam. Overall, the dose deposited to the surrounding normal tissues decreases [21].

1.4 2-Step Intensity Modulated Arc Therapy

In this work a treatment technique called 2-step intensity modulated arc therapy (2-step IMAT) is implemented into a computerized treatment planning system. The 2-step IMAT technique was first introduced by Bratengeier in 2001 [4]. The radiation beams are delivered to the target tumor continuously during two gantry rotations [4, 25, 26, 27, 28, 29]. Radiation is delivered to the planning target volume (PTV) through two beam segments, called the 1^{st} order and 2^{nd} order segments. They were defined as the 1^{st} and 2^{nd} order segments in Bratengeier's paper [4]. The beam shaping and the resulting intensity profile are illustrated in Figure 1.6a and b, respectively. Each segment is delivered during one continuous gantry rotation. All beam segments avoid the organs-at-risk (OAR), so that it can be spared. Although the beam intensity profile of each segment is uniform, the sum of the two segments from each angle produces a non-uniform intensity profile shown in Figure 1.6b. The resulting beam intensities are therefore modulated.

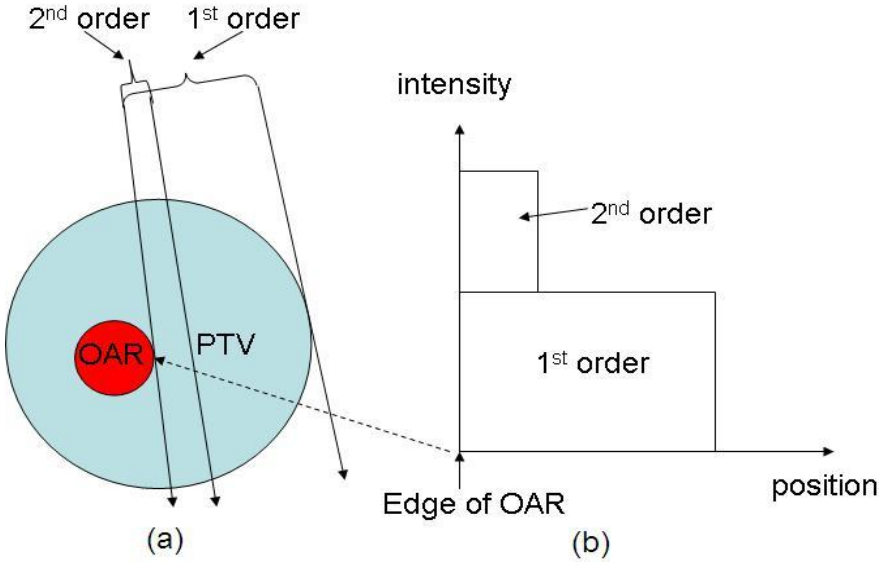

Figure 1.6: Illustration of (a) 2-step IMAT beam segmentation and (b) intensity profile. Reproduced based on Bratengeier's literatures [4].

Irradiating the PTV region near to the OAR during the second gantry rotation may seem contradictive to the aim of the radiotherapy, which is to maximally spare the OAR. However, this can be explained by the work done by Brahme *et al* in the early 1980s [5, 30]. In their work, a cylindrical phantom with a ring shaped PTV surrounding the organ at risk at the center of the cylinder was studied (see Figure 1.7). The beam was blocked from the edge of the OAR to spare the critical structure completely (the scattering effects were ignored in their study for simplicity), so that only the PTV was irradiated. The phantom was rotated 360° while the photon beams switched on to simulate the rotational treatment. The significance of their study was that they found that in order to achieve a conformal dose distribution inside the PTV, a physical non-linear filter was required to be placed in front of the beams, see Figure 1.7. The function of the filter was to create a non-uniform beam intensity profile, thus to improve the dose uniformity inside the PTV. The comparison between dose distributions of un-modulated beam and the modulated beam is shown in

Figure 1.8. Curve 1 represents the beam intensity profile and curve 2 represents the radius dose distribution inside the PTV. The uniform beam shown in the left graph, corresponding to a conformal arc without intensity modulation, resulted in a dose distribution with a broad "shoulder" [30]. The intensity modulated beam shown in the right graph is able to increase the steepness of the dose curve so that the dose distribution in the PTV becomes more uniform.

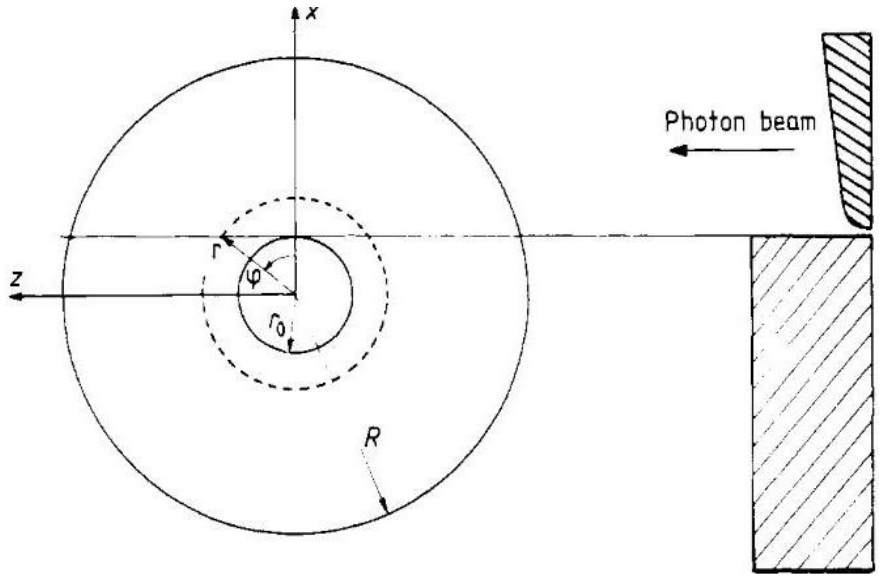

Figure 1.7: Photon beam is modulated by a filter before irradiating the cylindrical target [5].

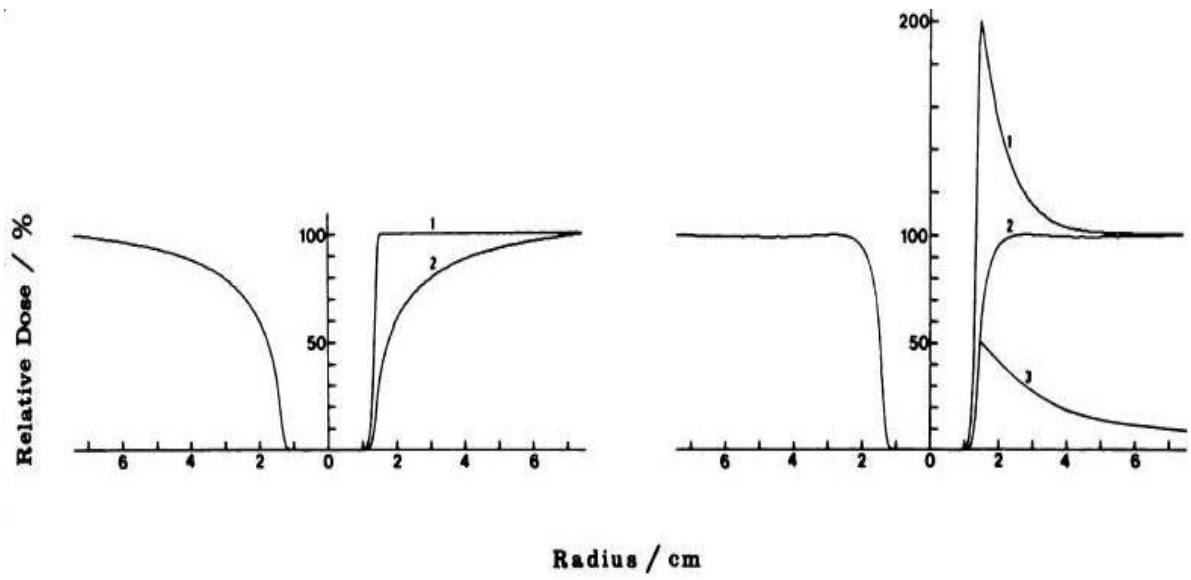

Figure 1.8: Intensity profile and dose distribution comparison of without (left) and with (right) filter modulation [5]. (Curve 1 is the beam intensity profile, curve 2 is the dose distribution and curve 3 is the fractional dose contribution resulted by the filter).

The physical filter is able to generate continuous beam intensity fluence. Different patients have different organ geometries projecting differently from different gantry angles. This requires individually shaped beam modulation for each patient and each gantry angle.

To approximate the intensity profile, one can create beam segments to generate a discrete intensity profile as shown in Figure 1.6, which is in fact the principle of the 2-step IMAT introduced by Bratengeier [4]. Because of the two distinct characteristics of the 2-step IMAT technique, i.e. continuous rotational treatment and simplified beam intensity modulation, it is hypothesized that the quality of the treatment plan can remain at a reasonable level while the complexity of the treatment planning and delivering process can be reduced.

1.5 Outline of Thesis

In this work, 2-step IMAT was implemented for the first time into a treatment planning system and an automatic process was developed to automatically generate 2-step IMAT treatment plans in the planning system. The properties of 2-step IMAT was then investigated through simulation.

The work of this thesis includes the development of the computer software module and the subsequent analysis of the 2-step IMAT technique implementation. Two software programs were developed, an automatic treatment plan generation program developed in the Prism Treatment Planning System and the treatment plan optimization scripts programmed in MATLAB. The work on the development of each program will be discussed in two separate chapters, Chapter 2 and 3, respectively. At the end of Chapter 3, the interaction between the two computer programs is described. The analysis of the 2-step IMAT implementation on the geometric phantom is discussed in Chapter 4 and 5. Finally, Chapter 6 shows the analysis of the implementation on a clinical case.

Chapter 2

Treatment Planning System

In this chapter, the treatment planning system used in this work is introduced. This is followed by a detailed discussion of the software module development that was implemented for automatic 2-step IMAT treatment plan generation.

2.1 PRISM

The treatment planning system (TPS) used in this work is the Prism TPS, which was developed at the University of Washington. The system was programmed in the Common Lisp language. The Prism source code is freely available for non-commercial use. To run Prism, the user requires a Linux environment and an Allegro Common Lisp [31]. The system-user interaction can be conducted under the X Window environment. The user can remotely connect to the Prism machine and operate the system through the X server. Once the Prism TPS is running, the user selects a patient case to be planned from the database and then creates a treatment plan manually. Within a plan, the properties of each beam may be specified from various control panels.

In order to modify and add new features to the Prism system, one needs to program in the Common Lisp language. The Common Lisp language is standardized from the previous dialects in the Lisp family of languages. A particular feature is the Common Lisp Object System (CLOS) that can build high level abstract object-oriented program. Such ability overcomes other popular language, such as C++, in the object-oriented programming sense.

The Prism TPS was chosen in this work because of the following reasons [32]:

1. Unlike other commercial software, the Prism TPS is free of charge for research purpose.

2. The existing graphical interface program, SLIK (simple Lisp interface kit) provides many common graphical interface components, such as scroll list, text box and press button. Therefore, it reduces the workload of this work in developing graphical user interfaces.

3. Unlike other languages, the Common Lisp language has the ability to run uncompiled and compiled functions alongside. This feature provides the convenience in the program development process. The programmer is able to program and test new functions while

the compiled standard Prism TPS is running, this freedom of interacting with the system increases the efficiency of the program development.

4. The Prism TPS is an object-oriented program, which allows developers to add new functionalities into the software. This ability of expansion of functions enables the system to evolve over time.

The abstract object-oriented design of the Prism TPS makes it easier to understand the existing codes and to add new software modules to the TPS. Many frequently used items in the radiotherapy treatment planning process, such as `patient`, `plan` and `beam` are defined as objects in the Prism TPS. There are attributes corresponding to each type of objects. For example, `gantry-angle`, `monitor-units` and `collimator-angle` are three of the many attributes of the `beam` object. To generate a beam irradiating the patient with 90 monitor units (MU) at a 20° gantry angle, the following Prism command is used:

```
(let ((new-plan (make-plan ‘‘My Plan’’)))
   (setf new-beam (make-beam ‘‘My Beam’’ :gantry-angle 20.0
                                         :monitor-units 90.0))
   (coll:insert-element new-beam (beams new-plan)))
```

The function of the above command is to insert a beam called “My Beam” into a plan named “My Plan”. The attributes of the `beam` object, `gantry-angle` and `monitor-units` are assigned with values during the creation of the `beam` object. It can be noticed from the last line of the commands that the `beam` object is actually an attribute of the `plan` object. Real world entities are represented by CLOS objects that interact with each other as shown in the above example. With such abstract object-oriented programming ability, the Prism TPS becomes a highly expandable system to implement new treatment techniques.

In the treatment planning and dose calculation sense, the Prism TPS is chosen for the following reasons [33, 34, 35]. The system is able to read and display clinical CT images in DICOM (digital imaging and communications in medicine) format. The treatment planner can use various control panels (see Figure 2.1), which were developed using SLIK, to design 3D CRT treatment plans and brachytherapy plans. The contours of organs are created by specifying points along the boundary of the organ. The dose calculation algorithm of the Prism TPS uses the pencil-beam, non-convolution algorithm [36]. Such algorithm may not be as dosimetrically sophisticated as the convolution/superposition algorithm or the Monte Carlo algorithm, but it is fast in calculating the dose. Therefore, it is a good choice for implementing and testing new treatment techniques.

2.2 2-Step IMAT Implementation

The Prism TPS has the ability to generate treatment plans but in a manual manner, thus the user is required to set the treatment plan parameters, such as gantry angle, couch position and beam portal for each beam in different panels. Due to the massive beam number in the 2-step IMAT treatment plan, it is extremely time consuming and heavily labor intense

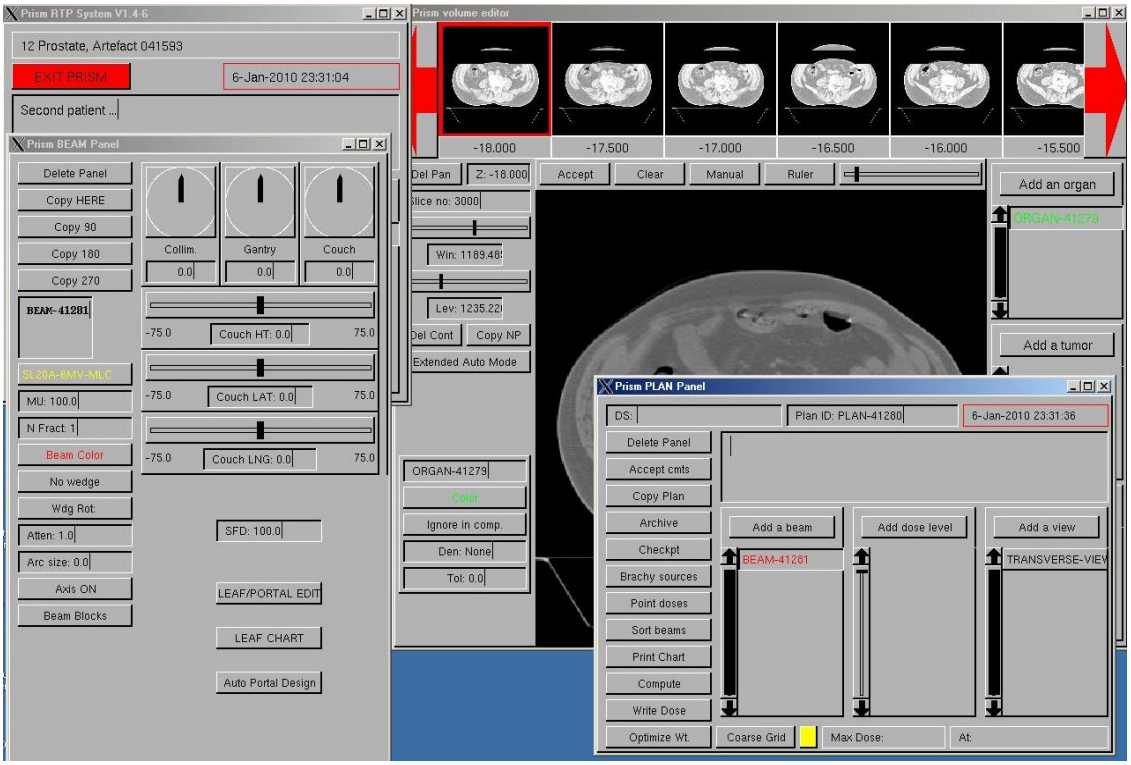

Figure 2.1: A desktop screenshot with some of the Prism TPS panels.

to manually create such a treatment plan, especially for the beam portal shaping process. Therefore, a user-friendly graphical user interface that can automatically generate the 2-step IMAT treatment plans is essentially required.

2.2.1 Graphical User Interface

Programming in the Common Lisp language, a graphical user interface (GUI) was developed for 2-step IMAT treatment planning (see Figure 2.2). The treatment planning GUI is discussed briefly in the following paragraphs in order to provide the necessary context in this thesis.

For a true full arc therapy treatment plan, there is an infinite number of beam angles because of the continuous irradiation during the gantry rotation. In the computer treatment planning simulation, a discrete number of beam angles is used to approximate the effect of the continuous arc therapy to conserve planning time. Therefore the treatment planner needs to specify the starting angle of the gantry rotational arc and the angle separation between adjacent beam angles. This operation can be completed by typing the inputs into the two textboxes at the top of the treatment planning GUI shown in Figure 2.2. The treatment planner has the freedom to specify the 2-step IMAT treatment plan parameters, such as the width of the second beam segments, in the GUI shown in Figure 2.2. The scroll lists allow planner to select the organs upon which the beam portals are designed (see Section 2.2.2 for detail).

The treatment planning GUI has three choices for different radiotherapy treatment plans, i.e. conventional arc therapy plan and two types of 2-step IMAT plans. The differences of

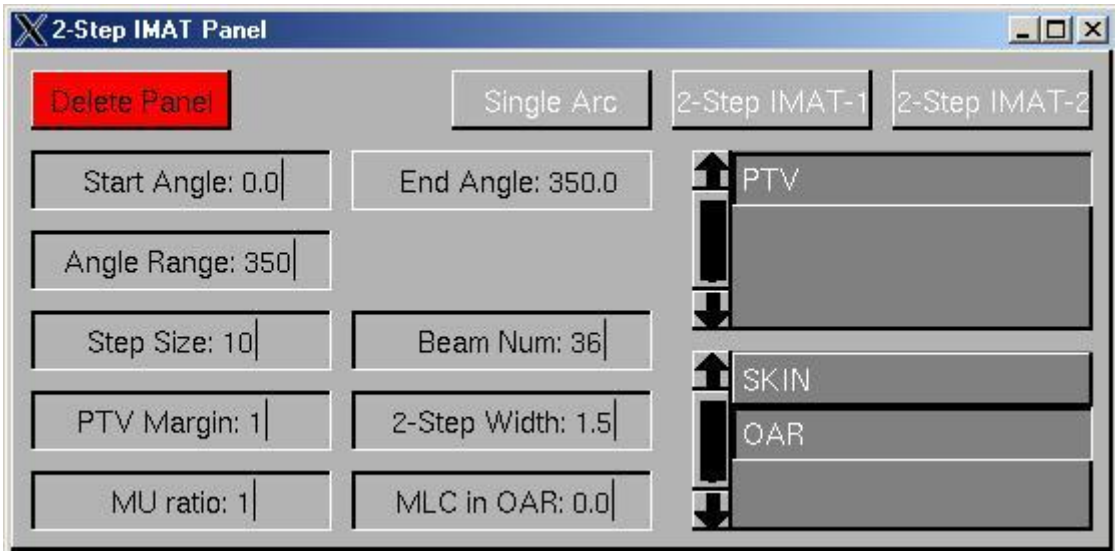

Figure 2.2: The GUI developed in this work to automatically generate 2-step IMAT treatment plan.

the two types of 2-step IMAT plans will be discussed in detail in Section 2.2.3.

By clicking on the button of a particular treatment, the treatment planning program will automatically generate the corresponding beam segments from each angle and then insert a new treatment plan into the Prism TPS. The entire operation is straightforward and easy to follow, the input into the GUI panel is sufficient for the program to generate a 2-step IMAT treatment plan.

2.2.2 Beam Portal Generation

Because of its close relation to the analysis work of this thesis (Chapter 4), the technique used for shaping the beam portals will be discussed in detail in this section.

The 3D volume information of the region of interest (ROI) can be generated by contouring structures on each CT slice. The contours of the ROIs are then used as a guide for the generation of the beam portals [2, 10].

Beam Shaping based on Ray-Tracing

The beam portal can be shaped using the ray-tracing technique. The path of all the rays are from the radiation source through the patient and then towards a distant imaginary 2D plane behind the patient. Figure 2.3 schematically illustrates the ray-tracing technique used in the beam portal shaping process [6]. Every ray from the source goes through a particular point on the 2D plane, on which all the ROI contours are also projected as shown on the leftside of Figure 2.3.

The overlap of the ROI projections and the point matrix on the 2D plane provides information on which points are within certain ROI. And then all the points within the PTV, for instance, will form the approximate shape of the PTV on the 2D plane. Among the points within the ROI, only those close to the edge of the ROI are used to set the beam

portal as the MLC leaves are pushed to these boundary points.

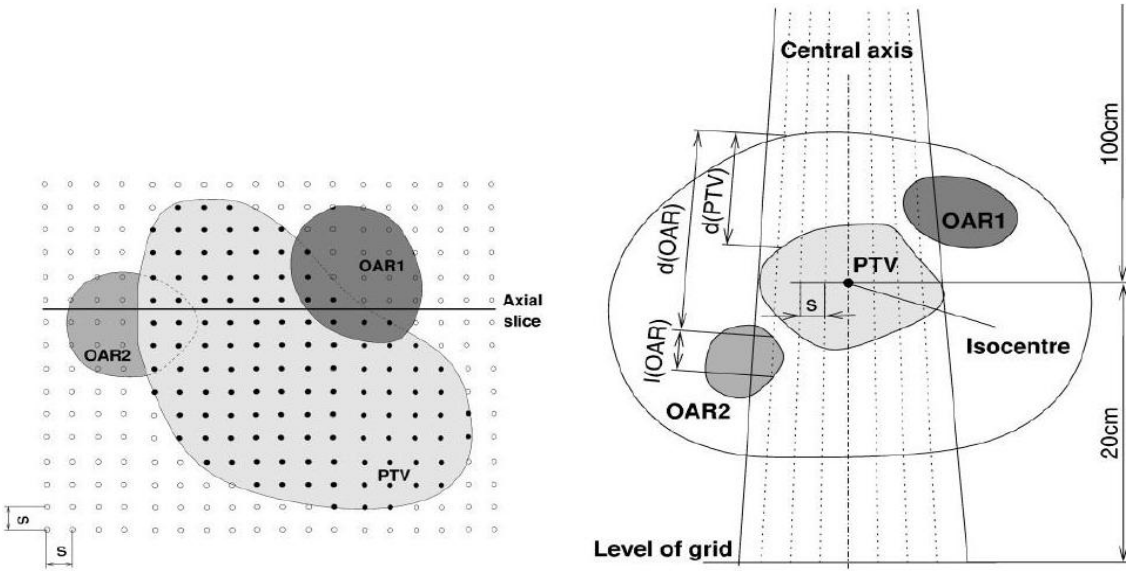

Figure 2.3: An illustration of the ray-tracing technique for beam portal generation. The leftside diagram shows the organ layout in the beams-eye-view with uniform points matrix (black points are within the PTV and white points are outside the PTV). The rightside diagram shows the transversal view of the setup. It can be seen from the left diagram that the spatial resolution of the point matrix influences the determination of the MLC setup [6].

The point separation size (or the spatial resolution) of the point matrix on the 2D plane influences the outcome of the MLC positioning in both accuracy and time consumption. On the one hand, a large separation size reduces the number of rays in consideration thus requires less time to calculate and setup the MLC leaves. On the other hand, the higher spatial resolution of the point matrix indeed improves the accuracy of the MLC setup, but the time of calculation is prolonged and more computer memory is required. Additionally, in a situation when the relatively small and big organs exist at the same time, optical nerve versus brain stem for example, the small separation size or a various spatial resolution depending on the size of the smaller organ is essential in order to detect the smaller organ. Therefore the treatment planning process will be complicated accordingly.

In this work, more efficient and less organ size dependent ray-tracing technique was developed to create the beam portal. Such a technique was implemented for one PTV and one OAR only. Future work will allow to include multiple PTV and OARs.

Beam Shaping for 2-Step IMAT

The CT images are usually in the transversal plane and all image slices represent the 3D volume of the patient. Therefore, the contour lines of the ROI are drawn on these transversal images. On each slice there is a set of 2D structures for each ROI. At any particular gantry angle, one can set the MLC leaves based on the geometry of these contours in the BEV. In the Prism TPS, the coordinates of the BEV and the gantry are defined differently, so a coordinate transformation has to be conducted during the portal shaping (the details of the coordinate transformation can be found in [37, 35]).

Assume that there is no MLC rotation and the MLC leaves slide in parallel to the transversal image slices. Take the cylindrical phantom in Figure 2.4 for example. Because of its cylindrical geometry, from each gantry angle the sum of all the contour slices of the PTV and the OAR appear as a rectangular shape in the BEV. If one wants to shape a beam portal such that it only irradiate the left part of the PTV. In the conventional technique, all the ROIs need to be projected onto a distant 2D bixel map and then the beam portal is shaped by sliding one side of MLC leaves to the points close to the left edge of the PTV and the other side to the points close to the left boundary between the PTV and the OAR. The error of the MLC setup varies depending on the size of each bixel. The modified beam portal shaping technique for 2-step IMAT is able to minimize the MLC setup error due to the spatial resolution of the point matrix. The first step is to search the boundary points on the PTV and the OAR contours on each slice, and then the MLC leaves are slided to these points to shape the beam portal (see Figure 2.4b). During the beam portal shaping, the PTV points are actually shifted to left by certain distance, so that this PTV margin is able to reduce the effect of the beam penumbra.

In the example shown in Figure 2.4, these boundary points will be the minimum contour points of the PTV and the OAR in that particular angle. As the gantry rotates around the phantom, the geometrical relation between the PTV and the OAR contours boundary points in the BEV changes accordingly, and so does the beam portal shape. For example, if the gantry rotates clockwise in Figure 2.4, the width of the beam portal will decrease. At the time when the minimum OAR points are equal or less than the PTV minimum points in the MLC coordinate, the MLC leaves are set to close in order to maximumly spare the OAR. The example shown in Figure 2.4 will not have the MLC leaves closed at any angle, since the OAR is completely within the PTV.

Comparing to the previous technique, the simplified technique is not influenced by the point separation size and it only requires the contour information and coordinate transformation calculation. Therefore, it is more efficient and accurate. Furthermore, as long as there is a contour drawn on each slice, the corresponding organ can be detected using this technique. As a result, the modified beam portal shaping technique is able to eliminate the problem encountered by the conventional technique in situation when the size difference between the PTV and the OAR is significantly large.

The beam portals for all the gantry angles are shaped using this simplified technique. In a 2-step IMAT treatment planning, the user can also use the GUI to specify the width of the second order beam segment portal and these beam portals will be shaped in a similar manner. Furthermore, certain size of margin was applied to the PTV side of the MLC leaves counter the penumbra effect.

2.2.3 PTV Coverage

At any gantry angle, the PTV has the following BEV geometry in situation when the PTV is larger than the OAR. First, the PTV is divided into two regions that do not overlap with the OAR in the BEV, such as for the gantry angle shown in Figure 2.5. Another situation occurs at certain angles where part of the PTV overlaps with the OAR and the other side does not. This is the case when the gantry irradiates the PTV horizontally in Figure 2.5.

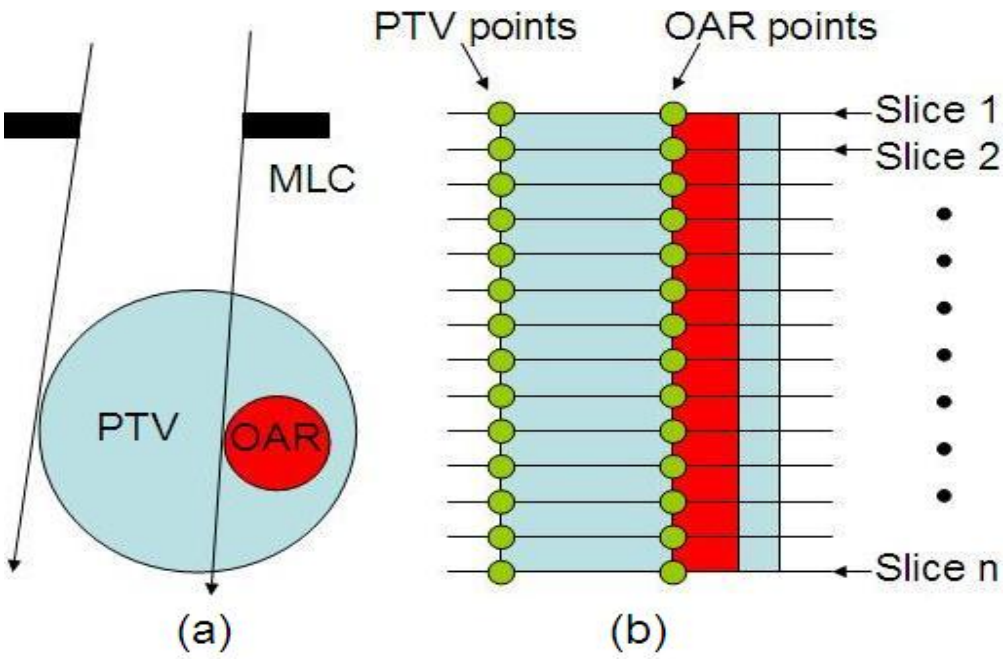

Figure 2.4: Illustration of the 2-step IMAT beam portal setup. The left diagram shows a transversal plane of the PTV, the OAR and the radiation beam. The right diagram shows the beams-eye-view. The PTV and OAR points are the boundary points on the corresponding contours, and the MLC leaves are pushed to these points to form a beam portal which provides the beam shown on left.

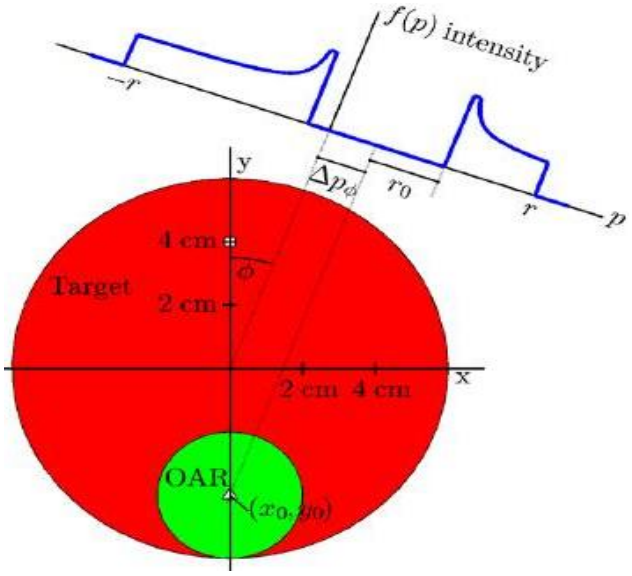

Figure 2.5: Illustration of the ideal beam intensity profiles. The geometry shown here provides two possible beam portals at this gantry angle, each portal is on one side of the OAR. Ideally, one wants to deliver both portals at the same time to reach the maximum efficiency and dose coverage [7].

In order to maximumly spare the OAR, one can irradiate only the PTV region that is not overlapped with the OAR. Ideally, the MLC leaves need to be shaped so that the OAR is always shadowed by the MLC at all gantry angles, such as the intensity profile shown in Figure 2.5. Then the ideal intensity profiles becomes as shown in Figure 2.6, in which the OAR is always spared while the efficiency of the PTV irradiation remains at a maximum [7]. However, such attempt is limited by the physical facts of the MLC, even by rotating the MLC leaves 90° the limitation still exists. Firstly, the width of the MLC leaves is constant so the leaves may not exactly shadow a random size OAR. Secondly, if the leaves are able to block the OAR (say, the width of a leaf is $0.5mm$ and the width of the OAR is $2cm$ in the BEV), the straight leaves can only shape the organ with a non-curvature side along the MLC sliding direction. As a result, only one side of the PTV in Figure 2.6 can be irradiated without rotating the MLC leaves during one gantry rotation and the two "banks" of the beam intensity becomes single "bank" as shown in Figure 2.7.

One can perform a second gantry rotation which produces the other side of the "intensity bank" to the PTV, so that the ideal intensity profile can be achieved. In Chapter 4.6 a comparison between one-side irradiation (one arc) and two-sides irradiation (two arcs) will be discussed in detail to explore this unknown.

2.3 Concluding Remarks

In this chapter the treatment planning system has been introduced, the abstract object-oriented design of the software provides the convenience to implement and study the 2-step IMAT radiotherapy technique. Furthermore, a simplified beam portal generation method has been developed in order to efficiently create the beam portal with less setup errors. In the next chapter, the treatment plan optimization concept and work will be discussed.

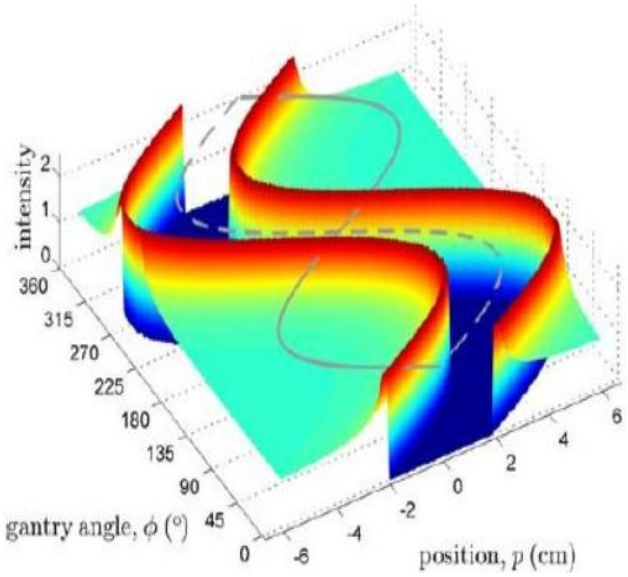

Figure 2.6: Graph of the beam intensity versus gantry angle and MLC position in an ideal arc therapy. The purpose of the middle sine wave shape intensity valley is in order to spare the OAR [7].

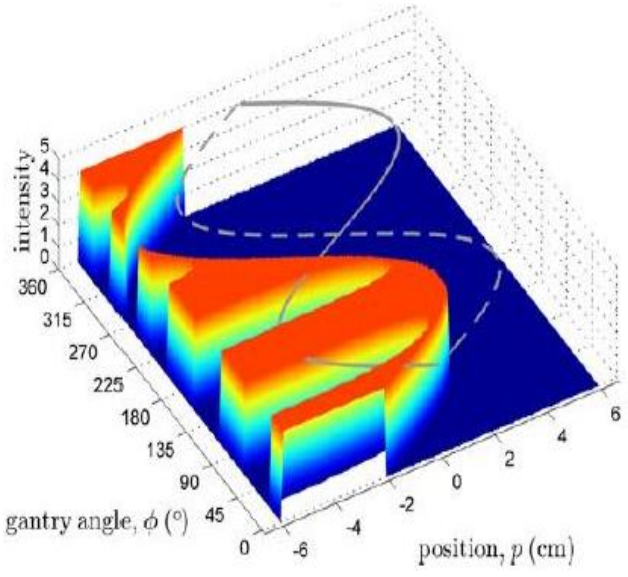

Figure 2.7: Graph of the beam intensity versus gantry angle and MLC position in a sinlge-arc therapy. Since only one side of the intensity "bank" can be delivered during one rotation, the other side of the intensity "bank" becomes null as the MLC leaves shadows from the edge of the OAR [7].

Chapter 3

Optimization

The implementation of 2-step IMAT was divided into two parts, the beam segment generation (Chapter 2) and the segment weight optimization. In the standard Prism TPS, the default setting is that plans are generated by selecting a certain number of beam directions with each beam having the same beam weight. As the MU of each beam is non-optimized to start with, the resulting dose distribution may not be optimal. As a result, the segment weight optimization is required to maximize the dose conformity inside the PTV and minimize the OAR irradiation. Beam or segment weight optimization is typically done manually for standard 3D CRT. In this chapter, the work on the development of the beam weight optimization approach as well as some improvements are discussed.

3.1 Introduction

Optimization plays an important role in treatment planning and there are two kinds of treatment plan optimization process, namely forward and inverse planning as already mentioned in Chapter 1. In the former optimization process, the treatment planner tries different parameter setups, such as various beam angles and corresponding beam weights. The dose distribution is calculated and manually adjusted if required. On the other hand, for inverse planning the planner specifies the desired dose objectives for a fixed number of beam directions and then lets the optimization find the ideal intensity maps that delivers the optimum result during the inverse planning processes. Comparing the two process, the forward optimization requires the treatment planner to have sufficient amount of clinical experiences in order to create a plan with reasonable quality with small number of tries. Forward planning becomes increasingly time consuming as the complexity of the treatment increases. The combination of all the possible gantry angles and beam weights, for example, make it impractical to find the globally optimal plan in a manual trial-and-error process. In contrast, during the inverse planning process the computer searches for the best parameter setup based on the specified plan objectives. Therefore, the planning process becomes automatized and the optimization of complex treatments becomes possible.

Ideally, one needs to optimize all possible parameters in order to achieve an optimal plan. Instead, the planner can optimize a single parameter while fixing the other parameters so that the complexity of the optimization process can be reduced. In this work, the beam energy

and the beam portal shape were selected prior to the optimization as described in Chapter 2. Only the beam weights, by means of the MUs, were varied during the optimization process in order to find the best solution so that a predefined set of plan objectives, such as a desired dose distribution and tolerance doses to the critical organs, can be satisfied.

There are two main types of objective function used in radiotherapy treatment plan optimization, physical-based and biological-based [38, 39, 40, 41, 42, 43]. The biological-based optimization uses the knowledge of the radiobiological effects on the tissues to find an optimal plan, so that the tumor control probability is maximized while keeping the normal tissue complication probability at a minimum [42, 43]. More commonly used is the physical-based optimization, which optimizes dose based objectives. In this work, the latter objective function was employed.

Appropriate definition of dose objectives is essential for the physical-based optimization. Before describing the optimization in the following sections, the method to define and represent the organs-of-interest, as well as the dose calculation for that volume will be discussed.

3.2 Volume Definition

As the shape of the typical organ is irregular, the general geometry equation does not usually apply to such shape of organ to calculate the volume. In the treatment planning process, the point sampling is often used for approximating the volume of irregular organs. There are two types of sampling method, uniform and random sampling. The uniform grid sampling method generates equally spaced points within the organ, each point represents the center of a cubic volume. By multiplying the cubic volume with the number of points lying inside the organ, the total volume of the organ can be calculated [44, 45]. Conversely, the random sampling method uses a normal probability to generate the points and then calculates the volume in a similar manner [46, 47].

In this work, the uniform sampling method was used for its simplicity to implement. During the sampling process, a cubic box was created to surround the entire volume of interest (VOI). Then points were uniformly generated in the box and each point can represent the center of a small cubic volume. As a result, the box was actually divided into many smaller cubic volumes called voxels, each of which represents a part of the cubic box and the sum of all voxels equals to the volume of the box. The center of each voxel (or each point created) is used to represent the position of that voxel. Whether a particular voxel is within the VOI is determined by whether the center of that voxel (or the point created) is within the VOI, as shown in Figure 3.1. The volume of the VOI can be determined by the total volume of voxels lying inside the VOI. The dose delivered to the VOI can be calculated using this voxel information.

One drawback of the uniform sampling is its inefficiency of using a cubic box to generate voxels, especially when the VOI is irregularly shaped. This method indeed wastes equipment resources by generating voxels outside the VOI, but it is easy to implement and guarantees the full coverage of the VOI.

Since the center of the voxels is used to define the location of the voxel, the size of the voxel is crucial to determine the volume of the VOI. As the voxel size increase, the uncertainty

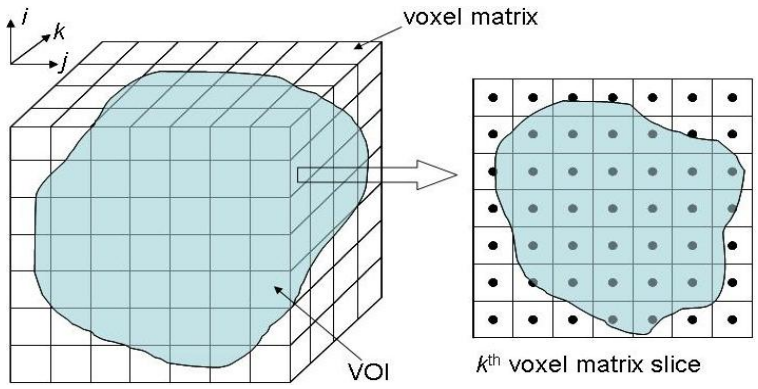

Figure 3.1: A discrete 3D matrix is created surrounding the organ, the voxels whose center points are located within the organ contour are used to represent the partial volume of the organ and the dose deposited into those voxels are the dose received by that organ.

of the VOI determination increases accordingly. Ideally, one wants to use infinitely small size voxels to determine the VOI, but it is time and equipment resource consuming and the benefits of using infinitely small voxels is unknown. This will be investigated in Section 4.2.

3.3 Dose Calculation

Depending on its direction and weight, each beam has a certain contribution on each voxel to that organ. One can construct a matrix consisting of all the contributions to the organ voxels from each of the beams. The normalized matrix can be used as a constant multiplied by the beam weights to calculate the dose to each voxel. The calculation can be expressed by the following equation:

$$\mathbf{M} \cdot \mathbf{x} = \mathbf{d} \tag{3.1}$$

The vector $\mathbf{x}$ is a collection of the beam weights. Each element in the row of the matrix $\mathbf{M}$ shows the contribution of different beams to a single point and each element in the column of the matrix $\mathbf{M}$ shows the contribution of a single beam to different points. For example, if a plan consists of three beams $((x_1, \ldots, x_3))$ and there are four points $(d_1, \ldots, d_4)$ are sampled inside the organ, the calculation of the dose deposited to the four points is given by Equation 3.2. For a pencil beam dose calculation, this matrix can be used as a constant.

$$\begin{pmatrix} m_{11} & m_{12} & m_{13} \\ m_{21} & m_{22} & m_{23} \\ m_{31} & m_{32} & m_{33} \\ m_{41} & m_{42} & m_{43} \end{pmatrix} \cdot \begin{pmatrix} x_1 \\ x_2 \\ x_3 \end{pmatrix} = \begin{pmatrix} d_1 \\ d_2 \\ d_3 \\ d_4 \end{pmatrix} \tag{3.2}$$

To this point, one can consider the dose calculation as a matrix multiplication in a multi-dimensional space, where the number of the variable dimension is defined by the number of beams. Taking the beam weights, $\mathbf{x}$, as the variable, one can mathematically define a function aiming to achieve a desired dose distribution, $\mathbf{d}$, and find the optimal solution of this function. Such function is called the objective or cost function and the process to search for the optimal solution of the objective function is called the optimization, both of the above are crucial in the optimization process. The definition of a reasonable objective

function sets the goal of the optimization. The desired dose distribution is used for the physical-based optimization. The method used to search for the optimal solution affects the time and efficiency of the treatment plan optimization. Ideally one wants a search method being able to converge to the optimal solution in the shortest possible time. The details of the objective function and the optimizing method used in this work is discussed in the following two sections, respectively.

3.4 Objective Function Definition

The objective function is usually defined in the quadratic form as shown in Equation 3.3 for the physical dose-based optimization [38, 39, 40, 41, 1] .

$$f = \frac{1}{N} \cdot \sum_{i=1}^{N} (d_i - d_{pres})^2 \tag{3.3}$$

In the above generic equation, the difference between the dose deposited to the i^{th} voxel, d_i, and the prescribed dose, d_{pres}, is squared to eliminate the negative value. The sum of all the squared differences for all N voxels is divided by the number of voxels and finally results into a single cost value. In order to achieve a uniform PTV dose coverage, one needs to find the optimum set of beam weights, $\mathbf{x}$, that results in a minimum cost value of the objective function. As there is typically no set of beam weights that achieves all doses inside the PTV equal to the dose prescription, the best solution is the one that minimizes the objective function, f, so that the doses to all the voxels are similar or close to the prescribed dose.

It is clear that the only variable in Equation 3.3 is dose, so the dose-based objective function is straightforward and easy to implement. However, this objective function needs to be modified in order to improve its suitability for the clinical usage and to increase its flexibility by taking the dose-volume objectives into account.

3.4.1 Dose-Volume Objectives

Typically, a clinician may want to deliver radiation doses so that "no more than X % of the organ volume receives more than Y unit of the radiation dose". In this situation the dose-based objective function cannot satisfy the clinical goals sufficiently, because it does not include the volume information. In order to relate the dose and volume information, a plan evaluation tool, called the dose volume histogram (DVH), becomes necessary in the optimization process.

The DVH is often used to show the dose-volume information of a treatment plan. The cumulative DVH is frequently used [9]. The cumulative DVH is a graph to show the volume percentage of a given organ receiving a specific dose. The DVH provides the planner with the dose-volume information of a plan. For an ideal plan, in which the PTV receives 100 percent of the prescribed dose everywhere inside and no dose was delivered to the OAR, the cumulative DVH for a PTV is the positive-half of a top-hat function, while the OAR DVH has zero area under the curve as shown in Figure 3.2, curve 1 and 2, respectively. However, in reality the dose is not strictly as conformal as desired, because the conformity of the PTV

cannot be achieved without the compromise of the OAR sparing. The under-dosed (cold spot) and the overdosed (hot spot) regions are reflected by the inward bending and outward bending curvatures on curve 3 in Figure 3.2. If the OAR is located close to the PTV, there will be doses delivered to the OAR as shown by curve 4 in Figure 3.2.

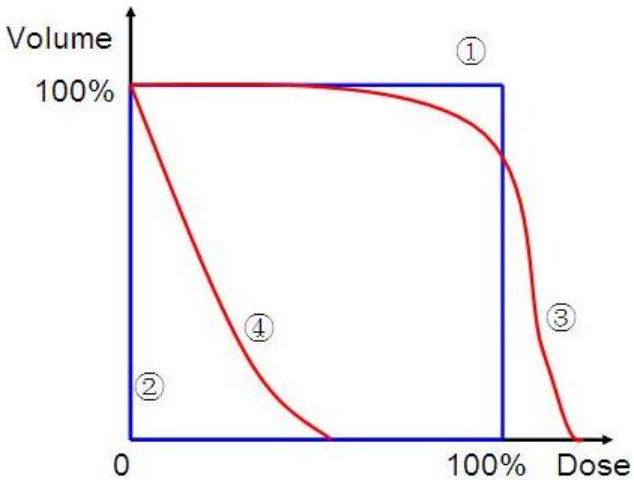

Figure 3.2: Ideal PTV and OAR DVH curves (1 & 2) and typical real PTV and OAR curves (3 & 4).

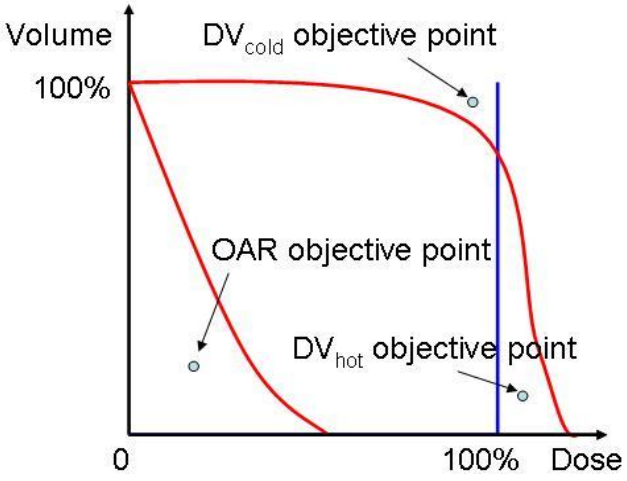

Figure 3.3: Three points can be used in the dose-volume-based optimization to increase the PTV dose uniformity and the OAR sparing.

The optimization with dose-volume objectives uses the DVH to relate the prescribed dose and volume information, so that the dose-volume objectives can be specified [38, 39, 40]. In the example shown in Figure 3.3, three basic dose-volume points are specified on the DVH, two on the PTV curve and one on the OAR curve. Since the aim of the optimization is to increase the steepness of the PTV DVH, thus improve the PTV dose uniformity, one point is specified near the cold spot region also referred as the minimum DVH objective and the other is specified in the hot spot region, referred to as maximum DVH objective. The third point is specified below the OAR DVH. With this approach the dose delivered to the OAR can be reduced. Together, the three dose-volume objectives allow the optimization to improve the general quality of the treatment plan.

Figure 3.4 illustrates using the DVH to apply the specified dose-volume objectives [38, 39]. In this example, the objective is defined as no more than V_{pres}% of the OAR should receive d_{pres} amount of radiation dose. Therefore, the aim of this example is to find beam segment weights which result in the DVH passing through or below the objective point (d_{pres}, V_{pres}). Graphically, as long as a plan results in a DVH with the shadowed area in Figure 3.4 to be zero, the plan satisfies the dose-volume objective.

In terms of implementation of the dose-volume objectives, during each iteration the DVH needs to be calculated before the objective function is calculated. The algorithm then searches on the current DVH to find the dose, d_n, that is received by the objective volume, V_{pres}. Any dose between d_{pres} and d_n is then penalized, so that the shadowed area shown in Figure 3.4 reduces to zero. The beam weights are then re-adjusted in order to minimize the objective function.

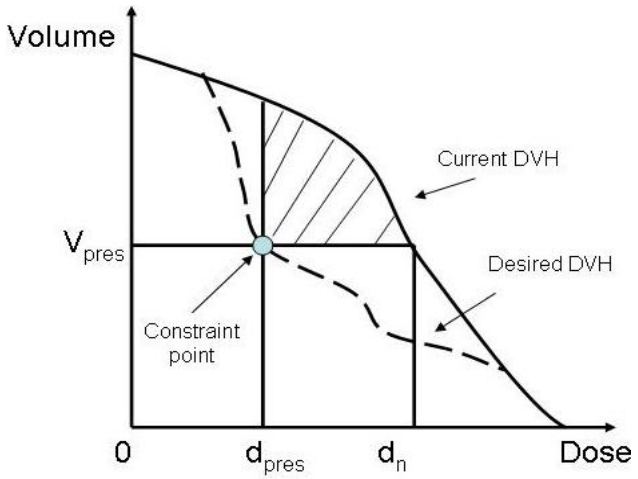

Figure 3.4: Illustration of the implementation of the dose-volume objective point in the optimization.

One can modify the dose-based objective function shown in Equation 3.3 to implement the dose-volume objectives. Since the only variable in the objective function is dose, the Heaviside function is useful in the determination and calculation of the objective function here. The Heaviside function is a step function shown in Equation 3.4 and it can be used to specify the range of doses.

$$H(a-b) = \begin{cases} 1, & a-b \geq 0 \\ 0, & a-b < 0 \end{cases} \tag{3.4}$$

Using the Heaviside function to specify the dose range, the dose-based objective function in Equation 3.3 can be modified to apply the dose-volume objectives.

For a single PTV and a single OAR the dose-volume-based objective function may be defined as following:

PTV cold spot objective:

$$f_{PTV,cold} = \frac{1}{N_{PTV}} \cdot \sum_{i=1}^{N_{PTV}} H(d_i - d_{cold}) H(d_{pres} - d_i)(d_i - d_{pres})^2 \tag{3.5}$$

PTV hot spot objective:

$$f_{PTV,hot} = \frac{1}{N_{PTV}} \cdot \sum_{i=1}^{N_{PTV}} H(d_{hot} - d_i)H(d_i - d_{pres})(d_i - d_{pres})^2 \tag{3.6}$$

OAR objective:

$$f_{OAR} = \frac{1}{N_{OAR}} \cdot \sum_{i=1}^{N_{OAR}} H(d_n - d_i)H(d_i - d_0)(d_i - d_0)^2 \tag{3.7}$$

For this particular example the combined objective function is:

$$f_{total} = \omega_{PTV,cold} \cdot f_{PTV,cold} + \omega_{PTV,hot} \cdot f_{PTV,hot} + \omega_{OAR} \cdot f_{OAR} \tag{3.8}$$

In Equation 3.5 - 3.7, N_{PTV} and N_{OAR} are the number of voxels in the PTV and the OAR, respectively. d_i is the dose deposited to the i^{th} voxel in the organs. d_{pres} and d_0 are the doses specified by the PTV and the OAR dose-volume objectives. d_{cold}, d_{hot} and d_n are the doses received by the constrained volumes on the current DVH, they are found using the method shown in Figure 3.4. Equation 3.8 sums all objective function results with different weighting factors, ω, to calculate the total cost value.

The role of the Heaviside functions in the above equations is to specify a range of doses to be taken into account based on the predefined dose-volume objectives. One example is shown in Figure 3.4. On the other hand, the dose-based objective function shown in Equation 3.3 takes all the unsatisfied doses into account.

Comparing with the conventional dose-based objective function, only a certain range of doses in the DVH contributes to the calculation of the objective function in the dose-volume-based objective function. With the dose-volume specification capability the dose-volume-based optimization is more flexible and suitable for clinical usage.

However, the advantage comes with a compromise. One drawback is that during every objective function calculation, the DVH has to be calculated and the corresponding dose d_n (in Figure 3.4) has to be determined on the curve in order to specify the range of doses to include in the calculation. This process of regenerating the 2D dose-volume information and searching the dose range prolongs the optimization time regardless of the speedup resulting from the reduction in the dose range. This effect becomes significant as the number of objective function calculations increases due to a random starting point that is far away from the optimal solution (details in Section 3.5).

3.4.2 Lambda Optimization Algorithm

From a mathematical point of view, one can realize that the conventional dose-based optimization algorithm is a special case of the dose-volume-based optimization algorithm. Taking the optimization of the OAR as an example, the conventional dose-based optimization penalizes the shadowed area as shown in graph in Figure 3.5, while the dose-volume-based objective function uses the 2D information from the DVH to specify the range of doses and penalizes the shadowed area shown in Figure 3.4. The specification of the dose range in Figure 3.4 allows the dose-volume-based optimization to reach a clinical acceptable solution

since less area on the DVH is penalized. It is worth noting that the optimal solution of the dose-volume-based optimization and the one of the conventional dose-based optimization are different due to the different definitions of the objective function.

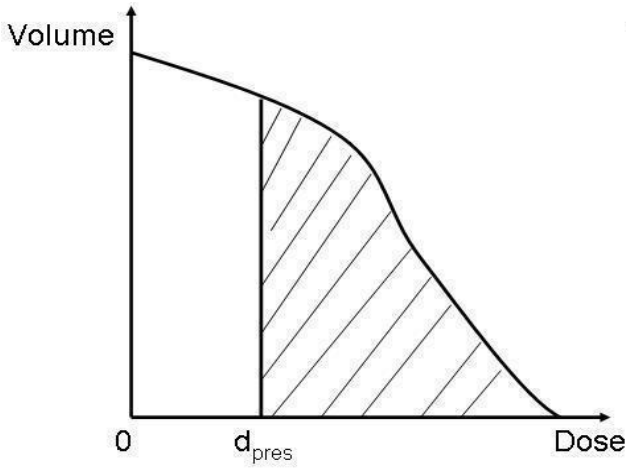

Figure 3.5: The conventional dose-based optimization penalizes the full dose range on the DVH. The d_{pres} in this example is the prescribed tolerant dose to the OAR.

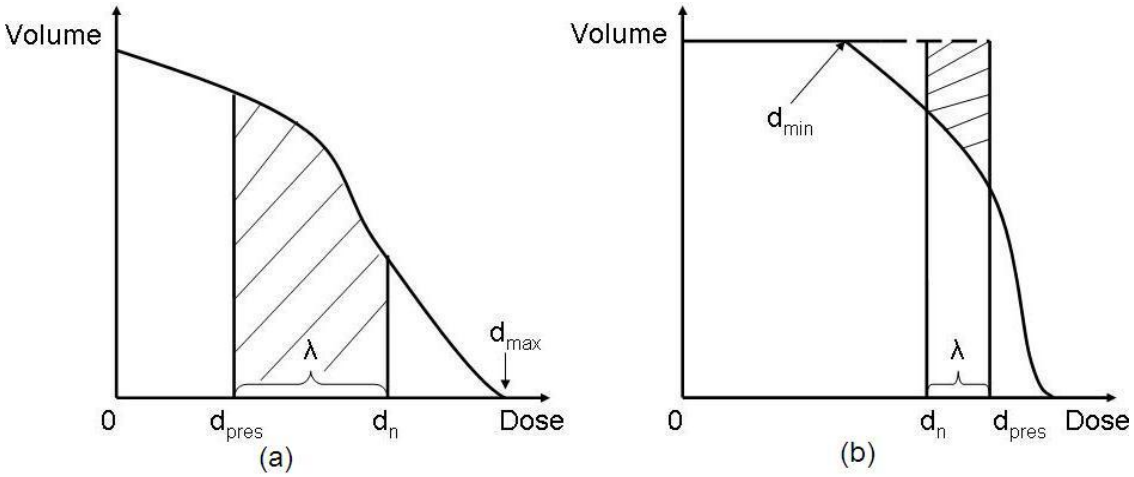

Figure 3.6: Illustration of the dose penalization using the lambda-value-dose-based objective function. The algorithm penalizes (a) the doses greater than the prescribed dose in order to reduce hot spot in an organ and (b) the doses less than the prescribed dose in order to reduce the cold spot in an organ. λ is the ratio of $d_n - d_{pres}$ to $d_{max} - d_{pres}$ in (a) and $d_{pres} - d_n$ to $d_{pres} - d_{min}$ in (b).

The dose-volume-based approach is computationally more expensive, as the dose-volume information has to be calculated during each objective function calculation. The dose points included the longer this calculation takes. In this work, a novel optimization algorithm modified from the conventional dose-based optimization, henceforth referred to as the lambda-value-dose-based objective function, was developed in order to speed up the optimization using the conventional dose-based objective function. Rather than using the volume and the DVH to specify the dose range for objective function calculation, the dose range is calculated using a λ value, which is defined as the proportion of the unsatisfied dose range to be considered in the objective calculation (see Figure 3.6).

In the implementation the objective function terms are also classified as two types depending on the side of the prescribed dose where the unsatisfied doses are calculated. The formulae of the lambda-value-dose-based optimization are shown as follows.

Objective function term for leftside of the prescribed dose:

$$f_{left} = \frac{1}{N} \cdot \sum_{i=1}^{N} H(d_i - d_n)H(d_{pres} - d_i)(d_i - d_{pres})^2 \tag{3.9}$$

Objective function term for rightside of the prescribed dose:

$$f_{right} = \frac{1}{N} \cdot \sum_{i=1}^{N} H(d_n - d_i)H(d_i - d_{pres})(d_i - d_{pres})^2 \tag{3.10}$$

Total objective function:

$$f_{total} = \sum_{k=1}^{N_{left}} \omega_{left,k} \cdot f_{left,k} + \sum_{k=1}^{N_{right}} \omega_{right,k} \cdot f_{right,k} \tag{3.11}$$

In Equation 3.9 and 3.10, N is the total number of voxel in that particular organ, d_i is the dose at the i^{th} voxel, d_{pres} is the prescribed dose for the PTV or the dose objective defined by the treatment planner for the OAR. The value of d_n is calculated using Equation 3.12 and 3.13 depending on the type of objective function.

d_n calculation for f_{left}:

$$d_n = (1 - \lambda) \cdot d_{pres} + \lambda \cdot d_{min}, \quad where\ 0 < \lambda \leq 1 \tag{3.12}$$

d_n calculation for f_{right}:

$$d_n = (1 - \lambda) \cdot d_{pres} + \lambda \cdot d_{max}, \quad where\ 0 < \lambda \leq 1 \tag{3.13}$$

The λ value is a user defined value to specify the range of the dose to be calculated in objective function. For different objectives the value of λ can be different depending on the user emphasis. N_{left} and N_{right} in Equation 3.11 are the number of objectives specified. The values of ω are the relative weighting factors for the different objectives.

According to Figure 3.3 and 3.6, the objective function term for the PTV cold spot can be replaced by f_{left} while PTV hot spot and the OAR calculation can use f_{right}. The total objective value can be calculated by multiplying each objective value with weighting factor, ω and then adding up to a single cost value using Equation 3.11.

Equations 3.9 to 3.11 are similar to Equations 3.5 to 3.7 used in the dose-volume-based optimization with the exception of the definition of the dose range. Instead of using the DVH to find the value of d_n received by $V_{pres}\%$ of organ (Figure 3.4), the modified algorithm calculates the dose range using the λ value in only the dose dimension.

Because the treatment planner can specify the range of unsatisfied doses to be considered in the optimization, the lambda-value-dose-based objective functions provide more degrees of freedom to optimize the plan, comparing to the conventional dose-based objective function shown in Equation 3.3. When $\lambda = 1$, Equation 3.9 to 3.11 become the same as the conventional dose-based objective function, Equation 3.3.

Unlike the dose-volume-based objective function in Section 3.4.1, the lambda-value-dose-based algorithm calculates the dose range in a one-dimensional space during each iteration of the objective calculation. Therefore the computational process is more straightforward and the calculation time is shortened.

However, the modified algorithm has one limitation. The simplification of dose range calculation eliminates the volume information. Since the optimization is conducted in the dose-coordinate only, the final objective value does not necessarily represent whether a certain dose is received by less than a certain volume. Thereby, it is not as clinically useful as the dose-volume-based optimization algorithm.

Based on the above limitation, one may question the reason to "degenerate" the optimization from the dose-volume-based back to the dose-based optimization in this work. The answer is two fold, firstly the introduction of the λ value increases the relaxation and flexibility of the conventional dose-based optimization by reducing the dose range to be calculated; secondly the usage of 1D calculation of the dose range improves the speed of the overall optimization comparing to the dose-volume-based optimization. Results of this improvements will be shown in Chapter 5.

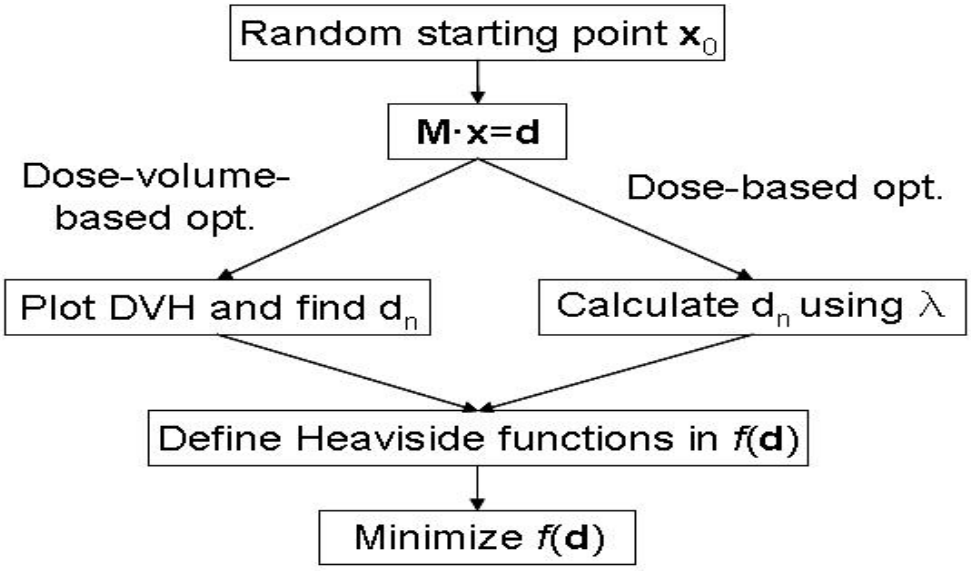

Figure 3.7: Illustration of the dose-volume-based and lambda-value-dose-based objective function optimization. The difference lies on the calculation of the value d_n to determine the dose range in the objective function calculation.

The optimization process using the dose-volume-based and dose-based objective function is shown in Figure 3.7. The optimization starts at a randomly generated starting point, $\mathbf{x}_0$, and then using Equation 3.3 to calculate the point doses, $\mathbf{d}$, received by the organ. Depending on the choice of the objective function, the program either plots the DVH and finds the value of d_n for the dose-volume-based optimization or it calculates d_n using Equation 3.12 or 3.13. Finally, the Heaviside function is defined and the objective function can be calculated and minimized. The process of looking for the value of d_n is the critical difference that defines the speed of the algorithm. Since the calculation of d_n is only in a 1D space (dose-based objective function) rather than in a 2D space (dose-volume-based objective function), the

former algorithm should be faster than the latter one. The comparison between the two optimization algorithms will be discussed in Chapter 5.

3.5 Optimal Solution Search Algorithm

As stated in Section 3.3, the two essential components of an optimization process are the definition of objective function and the optimal solution search technique. The first component has been discussed in Section 3.4; in this section the second component will be introduced.

For any given (convex or non-convex) function $f(\mathbf{x})$, one can solve the function for all possible $\mathbf{x}$ values to be guaranteed to find the minimum solution to $f(\mathbf{x})$. The number of possible combinations can be calculated using Equation 3.14 [48]. In this equation, the number of combination, C, is given by a power relationship between m and k, where the power k is the number of variables and the base m is the possible states of each variable. For example, if $\mathbf{x}$ is a vector of three components and each component can have two states (say spin-up or spin-down), $\mathbf{x}$ has 8 possible combinations of the variable components for the calculation of $f(\mathbf{x})$.

$$C = m^k \tag{3.14}$$

As the size of the vector variable and the possible states increases, the total number of combinations increases following the power curve of Equation 3.14. The vector variable $\mathbf{x}$ in the above example represents the beam segment weights vector, $\mathbf{x}$, in Equation 3.1 and the possible states represents the available weights. Obviously it becomes impractical to exhaustively search the optimal solution by calculating the values of the objective function for all possible beam weight combinations. For example, the number of beam segments used in this work is around 200 and each one may have possible beam weight ranging from 0 to 50 in step of 0.1 MU, say. As a result the total number of combination is $\tilde{}9.3 \times 10^{539}$. Techniques to search the space of $\mathbf{x}$ in a more logical manner rather than the brutal force method are required and have been studied previously.

Two of most significant and widely used search techniques in treatment plan optimization are gradient-based techniques and simulated annealing [49]. The gradient-based algorithm is classified as a deterministic algorithm. Taking a non-convex function with one variable as an example, shown in Figure 3.8. If the problem is to find the value of x that minimizes $f(x)$. The gradient-based method searches along the descent gradient, so that the following inequality is always true, where Δs is the variable increment step size [50, 51, 52].

$$f(x^k + \Delta s) < f(x^k) \tag{3.15}$$

Figure 3.8 shows that the function reaches the global minimum at $x = 7$. If the search begins at $x = 5$ or $x = 8$ and the increment step size is less than 2 or 1, respectively, the search is definitely able to find the global minimum. However, if for instance the starting point is at $x = 17$ and searches every one unit of x, then the gradient-based method will be trapped at a local minimum at $x = 14$. In another case, if the starting point is at $x = 2$ and the algorithm searches in steps of 2, the search will overlook the global minimum at $x = 7$

and give the minimum at $x = 6$. As a result, in the gradient-based search both starting point and increment step size are crucial to the result. Because it uses the gradient of the function as the basis of the search, on the one hand for any arbitrary starting point if there exists a local minimum between the starting point and the global minimum the gradient-based algorithm might be trapped at the local minimum. On the other hand, if a bigger increment step size is chosen there is a possibility to get out of the local minimum trap, but the bigger step size may result in missing the global minimum.

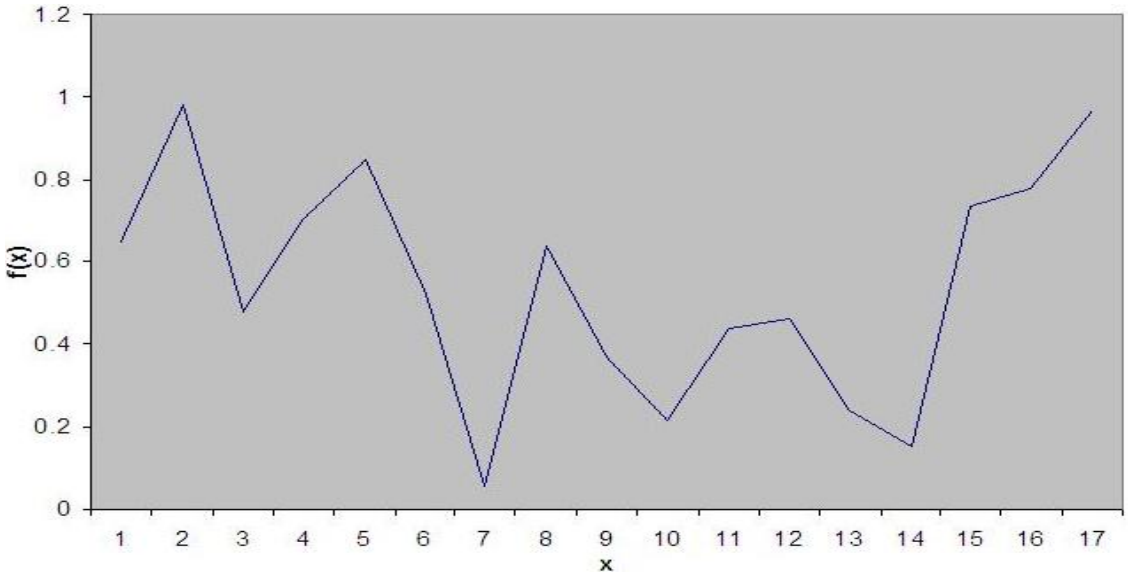

Figure 3.8: A randomly generated one-variable, non-convex function with the global minimum at $x = 7$.

Unlike the former technique, the simulated annealing is a stochastic algorithm that uses a random search technique and certain transition probability to search for the optimal solution [50, 51, 52]. The random search allows the algorithm to explore more space than just following the descent gradient from a predefined starting point. The transition probability is a decay exponential form based on the Boltzmann's distribution that enables the algorithm to "generously" accept some unexpected solution (e.g. $f(x^k + \Delta s) > f(x^k)$) during the optimization. Therefore, with enough randomness the simulated annealing algorithm is able to find the globally optimal solution with less chance to get stuck at a local minimum. However, the compromise of the bigger probability to find the optimal solution is the prolonged optimization time due to the random searching, especially for a function with a large variable set as in the case of IMAT. Furthermore, the selection of transition probability is crucial since over acceptance may lead to longer optimization time while tight acceptance may result in trapping at the local minimum.

3.6 Implementation in MATLAB

The standard Prism TPS does not have an optimization process designed for the 2-step IMAT technique. Work on developing optimization program within the Prism TPS using Common Lisp was conducted. The objective functions were programmed, but the process

stopped at the development of the optimal solution searching algorithm code for its complexity of programming in the low level language. Since the optimum search algorithm is not the main aim of this work, to simplify the work and concentrate on the radiotherapy development, MATLAB® (MathWorks^{TM}, Version 7.8.0.347($R2009a$), USA) software was chosen to perform the optimal solution search task because of its powerful optimization toolbox package.

In MATLAB the optimization consists of two parts, the objective function script and the optimal solution search algorithm script. In this work, both the dose-volume-based and the lambda-value-dose-based objective functions were programmed into the MATLAB scripts for the use of the treatment plan optimization. In the optimal solution search algorithm script, certain type of optimal solution search algorithm is called upon the objective function to look for the solution giving a minimum cost value. It contains the program to call the particular algorithm to perform the optimal solution search on an objective function. There are both gradient-based and simulated annealing algorithms pre-developed in the MATLAB software. In this work, only the gradient-based algorithm was used for the time reasons.

The MATLAB build-in function used in this work was called "fmincon", which uses the so called quadratic programming (QP) method [50, 51, 53] to solve the QP problem that have quadratic form of objective function. Since it is impossible to deliver a radiation beam with negative intensity, the lower boundary constraint of beam weight vector, $\mathbf{x}$, was set to zero. As the gradient-based algorithm is used in this work, each iteration of the optimization starts from random starting points within the space of the beam weight vector, $\mathbf{x}$ in order to reduce the chance being trapped at a local minimum.

3.7 Prism and MATLAB Data Interaction

To this point, the two main programs developed in this work have been introduced in detail. The entire treatment planning process is completed in two steps and in two separate program environments. The original radiotherapy treatment plan is generated in the Prism TPS while the treatment plan optimization process is conducted in MATLAB. This section discusses the method to connect two systems so that the treatment plan data can be transferred between two systems without confusion or unnecessary changes.

Refer back to Section 3.2, the dose points are first created inside the organs of interest. Once the treatment plan was generated in Prism, the normalized matrix, $\mathbf{M}$, is calculated. Then this matrix is saved to the local drive for further use in MATLAB.

The point doses are calculated based on Equation 3.1 in MATLAB. The MATLAB scripts will then optimize the point doses by altering the segment weights, $\mathbf{x}$ in Equation 3.1. Once a satisfactory result or the best result the optimization can achieve has been found, the optimization stops and saves the optimized segment weights to the local drive.

A Common Lisp code was developed to read the file containing all the optimized segment weights and assign each weight to the corresponding beam segment in Prism. Up to this stage, the entire treatment planning process is completed. Using the optimized segment weights, the treatment planner can calculate and display the dose distribution in Prism.

The detailed flowchart of the entire process is shown in Figure 3.9.

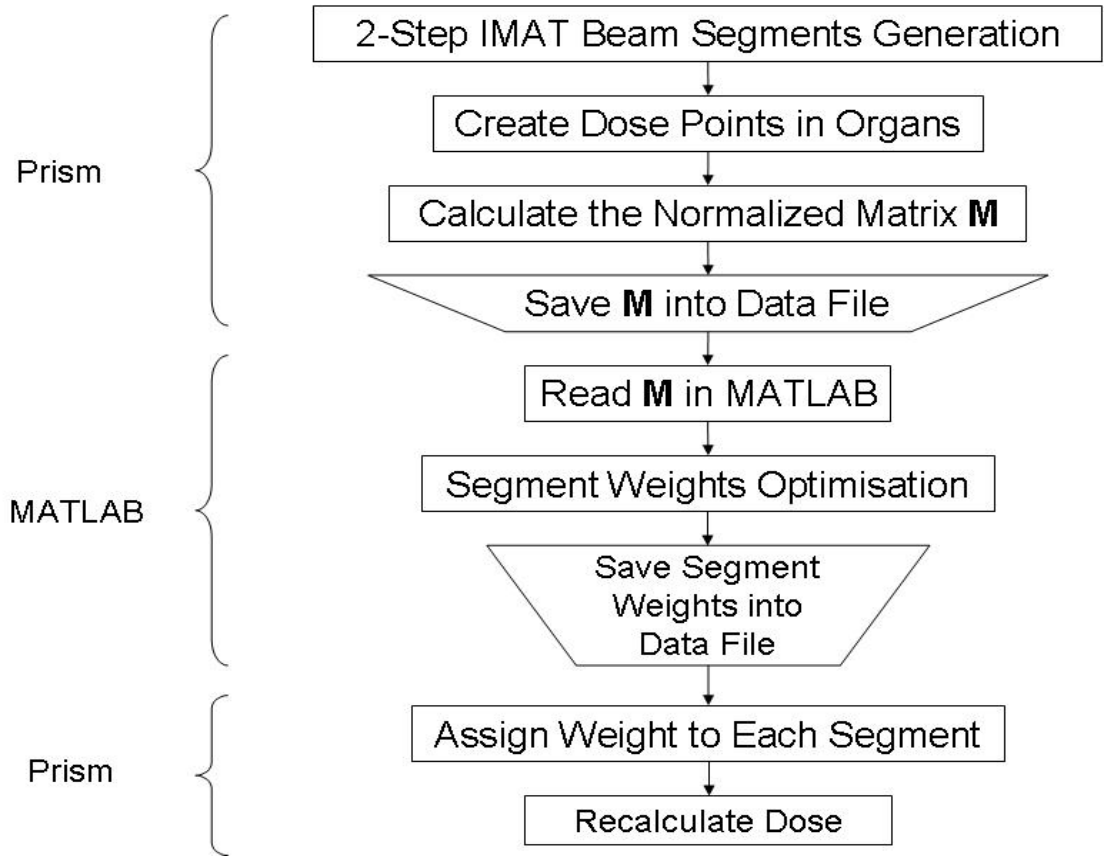

Figure 3.9: The flowchart to illustrate the working structure of the complete treatment plan generation process in both Prism and MATLAB.

3.8 Concluding Remarks

In this chapter, the concept of the treatment plan optimization has been introduced. The non-convolution dose calculation algorithm used in this work simplifies the dose calculation to matrix multiplication shown in Equation 3.1. In this work, both the dose-based and dose-volume-based optimizations were implemented and used to optimize the segment weights of a treatment plan. For the dose-based optimization, a modified objective function that uses the lambda value to specify the dose range was developed in order to increase the flexibility of the dose-based optimization. The optimal solution search algorithm used in this work is the gradient-based algorithm for its fast and simple application. The entire treatment planning process was completed in two environments, Prism and MATLAB. Both the program codes in Common Lisp and MATLAB were developed in order to transfer the data between the two programs in simple steps. Note that the main programs have been developed, so that the 2-step IMAT radiotherapy technique can be investigated. In the following chapter, an analysis on the setup parameters is performed.

Chapter 4

Analysis of Setup Parameters

Accurate dose calculation in the treatment planning system depends on the dose calculation algorithm and the size of the dose voxels. Large voxels speed up the calculation but compromise the true dose representation and vice versa. The dose sampling affects the accuracy and the speed of the dose calculation. The first analysis examines the choice of dose voxel size that keeps the dose calculation efficient. Since 2-step IMAT is a rotational treatment, a suitable number of beam angles is necessary to approximate a continuous irradiation. Therefore, the second analysis is to determine the number of angles sufficient for a reasonable approximation. After choosing suitable number of angles, the two parameters of the 2-step IMAT technique, i.e. the ratio of the two segments and the second segment width at each gantry angle are altered, one at a time, to find a suitable setup. Finally, the number of gantry rotations will be analyzed to find the effect of the gantry rotation on the quality of the plan.

4.1 Phantom

All analysis in this chapter is based on a geometrical phantom. The phantom used is shown in Figure 4.1. It is based on the horseshoe phantom used by Bratengeier [4] and has the same dimensions. This particular phantom was chosen for its concave-shaped PTV that surrounds the OAR. In such a situation it is challenging to plan a conformal dose coverage while sparing the OAR using conventional 3D CRT. It should be noted that a similar arrangement of organs commonly appears in clinical cases, such as head & neck, prostate and paraspinal tumors.

The geometric phantom consists of three organs, the PTV, the OAR and the external contour. Similar to clinical CT image data, the geometric phantom is represented by a collection of transverse slices, on which the organ contours are outlined. Practically, the phantom contours were generated using an Excel spreadsheet and then transferred into the Prism format. The Prism TPS has the ability to copy contours to other slices by clicking buttons, but it is considered too labor intensive for a phantom with many slices. For example, the user has to copy the contours 60 times for a $30cm$ long phantom with slices separated by $0.5cm$. Therefore, some Common Lisp codes were developed to read the contour data from the spreadsheet and automatically generate the entire phantom slices in the phantom file. The code was specifically designed for generating Prism file of cylindrical organ contours.

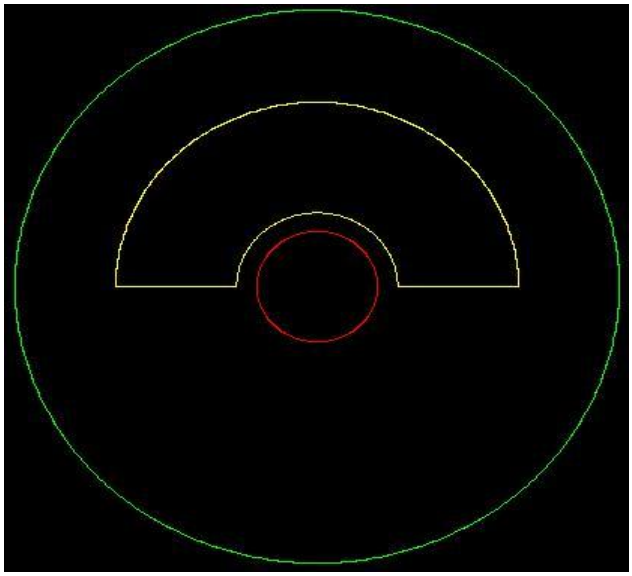

Figure 4.1: Transverse view of the geometric phantom (yellow: PTV, red: OAR, green: external contour). (Regenerated based on Bratengeier's paper [4]).

4.2 Grid Size Analysis

The dose sampling is crucial in the dose calculation during the treatment plan evaluation. A uniform sampling method is used in this work for its simplicity (refer to Section 3.2). The accuracy and the speed of the dose calculation depends on the selection of the voxel size. A small voxel size provides more accurate dose calculations, but the compromise is the prolonged time consumption and large computational cost. Ultimately, one wants to sample as many points as necessary to achieve a high accuracy within a reasonable time frame. Therefore, the aim of this first analysis was to determine a reasonable voxel size for dose sampling to achieve sufficient accuracy in the dose calculations.

A 2-step IMAT treatment plan was generated with the following constant parameters: the angle step size was 5°, the ratio of the 1^{st} beam segment to the 2^{nd} beam segment for each gantry direction was fixed to 1.5. The width of the 2^{nd} segment was fixed to $1.5cm$. The choice of the above parameters was based on the previous investigation reported elsewhere [54] (abstract in Appendix A).

The analysis is divided into two parts in order to find a reasonable voxel sizes for the PTV and OAR separately. The dose points with different voxels sizes are generated in a given organ. Prism calculates the corresponding normalized matrices, $\mathbf{M}$ shown in Equation 3.1. The matrices are then transferred into MATLAB for further calculation. Assuming the dose calculation of the smallest voxel size represents the most accurate dose result, since the finest voxel size contains the most dose points which provides more dose-volume information. The matrix of the finest voxel size is used to calculate the point doses inside that particular organ using Equation 3.1. A MATLAB code was developed to automatically adjust the segment weights vector, $\mathbf{x}$, so that the DVH is normalized to D_{95} point. The D_{95} is the dose that is received by 95% of the organ volume. In other words, on the DVH diagram the above point is located at the coordinate $(100, 95\%)$. Using the finest voxel size matrix, the DVH was calculated. The segment weights vector, that normalized the DVH to D_{95}, is then used to

calculate the DVHs of other voxel sizes.

Based on the assumption made previously, the DVH function $V(d)$ calculated from the finest voxel size is used as the reference. For all other larger voxel sizes the root mean square (RMS) difference from the reference DVH function is taken:

$$RMS = \sqrt{\sum_{i=0}^{d_{max}} (V(d_i) - V_{ref}(d_i))^2} \tag{4.1}$$

The summation range is from $i = 0$ to the maximum dose on the DVH plot, d_{max}. In this work all DVH is plotted up to 120cGy, so $d_{max} = 120$ for the increment step size of 1cGy. $V(d_i)$ and $V_{ref}(d_i)$ are the percentage volumes, that receive d_i dose, based on the dose calculation of certain voxel size and the finest voxel size, respectively. This RMS is the measure of the total percentage volume difference between the DVH calculated based on the finest voxel size and a certain larger voxel size. Therefore, the summation is not divided by the total number of dose index to give the average difference. It was expected that the RMS difference increases with voxel size.

The minimum voxel size for the PTV without running out of the computer memory was $0.3cm$, so the $0.3cm$ DVH was the reference for the RMS difference calculation. The voxel size increases to $1cm$ in $0.1cm$ steps. For voxel sizes larger than $1cm$, large increments values of the voxel size were selected up to $2.5cm$ in order to investigate the trend.

The finest voxel size for the OAR was $0.2cm$, so the $0.2cm$ DVH was the reference for the RMS difference calculation. The voxel size increases to $0.5cm$ in $0.1cm$ steps. For voxel sizes greater than $0.5cm$, arbitrary voxel sizes were chosen.

The related PTV values for different voxel sizes from $0.3cm$ to $2.5cm$ are shown in Table 4.1. A similar work was conducted to find the suitable voxel size for the OAR. Table 4.2 shows the results for voxel size from $0.2cm$ to $2.0cm$.

The time of dose calculation is consistent with the number of points inside the PTV as the voxel size decreases. The plots of the two graphs are shown in Figure 4.2. The curve suggests that as the voxel size increases beyond $1.5cm$, it will not materially improve the simulation time.

Figure 4.3 shows that the dose calculation speed increases as well as the RMS difference (Equation 4.1) as the voxel size increases. A voxel size of $0.7cm$ was decided to be a compromise between calculation speed and accuracy as shown in Figure 4.3.

Figure 4.4 shows the consistent drop in both number of dose points and the calculation time for the OAR. Figure 4.6 shows the trends of the calculation time and the RMS as the voxel size changes. The voxel size of $0.4cm$ was chosen for a good compromise between speed and accuracy. The choice is mainly based on the OAR DVH comparison shown in Figure 4.5. Assuming the $0.2cm$ voxel size provides the most accurate representation of the OAR DVH, the $0.4cm$ voxel size is the closest approximation with a shorter dose calculation time (the voxel size of $0.3cm$ for the OAR run out of memory when calculate the PTV and the OAR at the same time).

The accuracy of the dose calculation is an important process in the treatment planning, but so is the speed of the calculation. Based on this analysis it was decided that a suitable

Voxel Sizes (cm)	Number of Points	Calculation Time	RMS
0.3	48444	NA	NA
0.4	20750	22.09min	0.06
0.5	10560	11.31min	0.07
0.6	6239	6.73min	0.08
0.7	3738	3.98min	0.11
0.8	2436	2.57min	0.13
0.9	1804	1.99min	0.15
1.0	1320	1.41min	0.14
1.3	640	41.89s	0.17
1.5	406	26.62s	0.21
1.8	246	16.86s	0.29
2.0	170	10.68s	0.39
2.5	80	5.56s	0.62

Table 4.1: Results for the PTV with voxel sizes between $0.3cm$ and $2.5cm$. The calculation time of $0.3cm$ voxel size is missing because the computation run out of memory.

Voxel Sizes (cm)	Number of Points	Calculation Time	RMS
0.2	35800	39.82min	NA
0.3	10428	11.21min	0.16
0.4	4425	4.91min	0.32
0.5	2240	2.52min	0.49
0.8	516	32.24s	0.52
1.0	320	21.26s	1.17
1.5	84	5.43s	1.96
2.0	45	3.03s	2.43

Table 4.2: Results of the OAR with voxel sizes between $0.2cm$ and $2.0cm$.

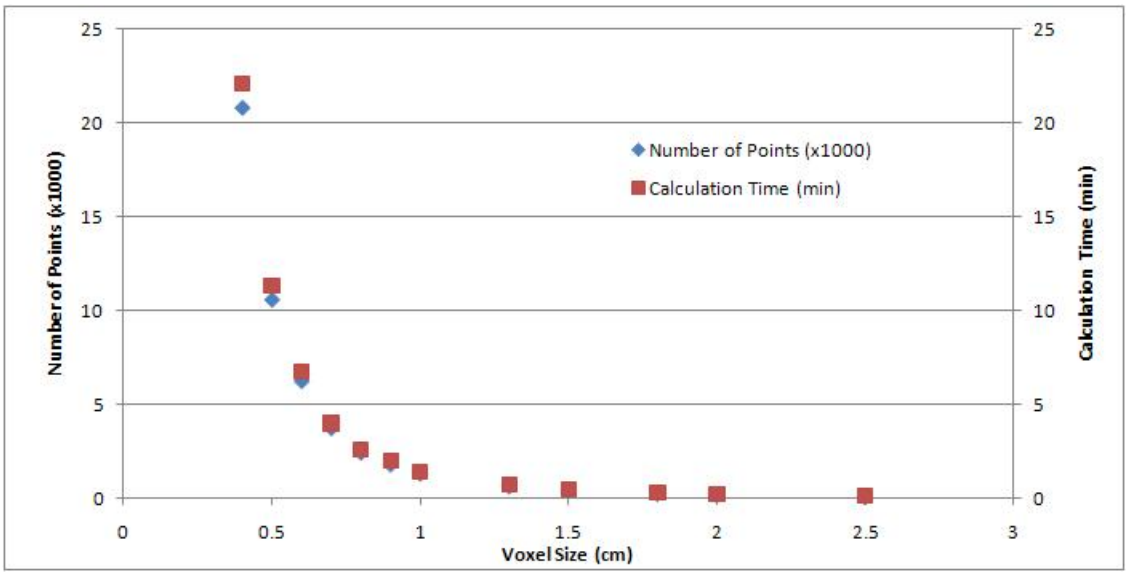

Figure 4.2: The number of points inside the PTV and the dose calculation time versus voxel sizes from $0.4cm$ to $2.5cm$.

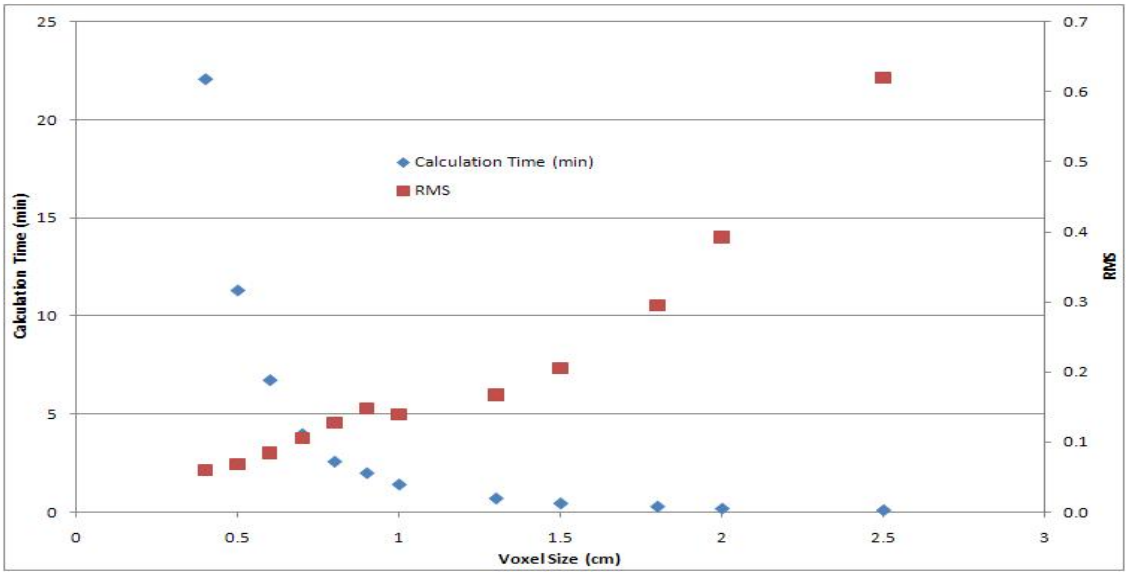

Figure 4.3: The dose calculation time and the RMS difference versus PTV voxel size.

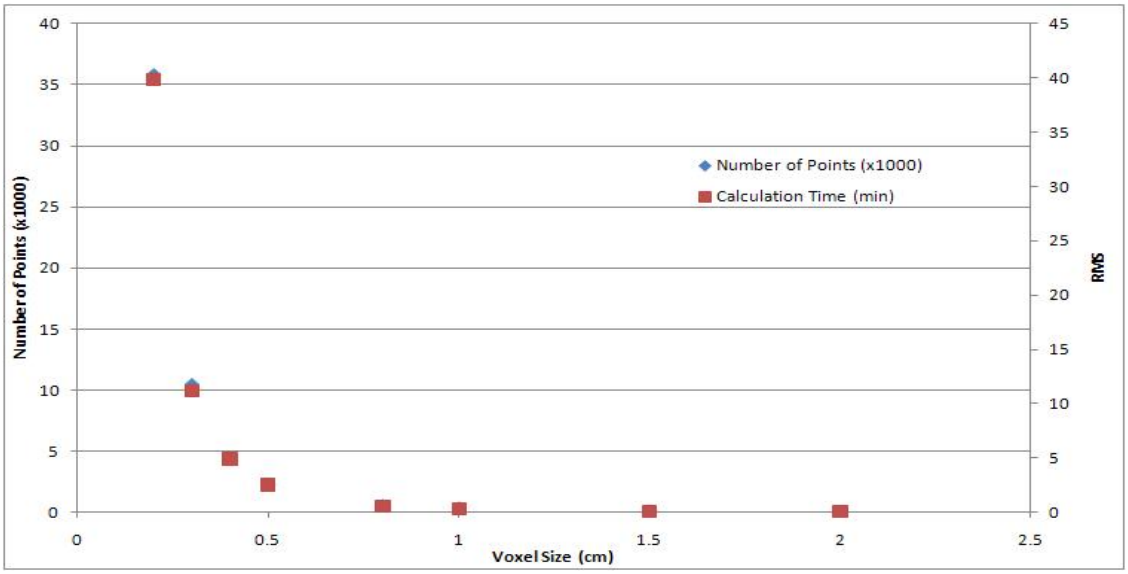

Figure 4.4: The number of points inside the OAR and the normalized matrix calculation time versus voxel size.

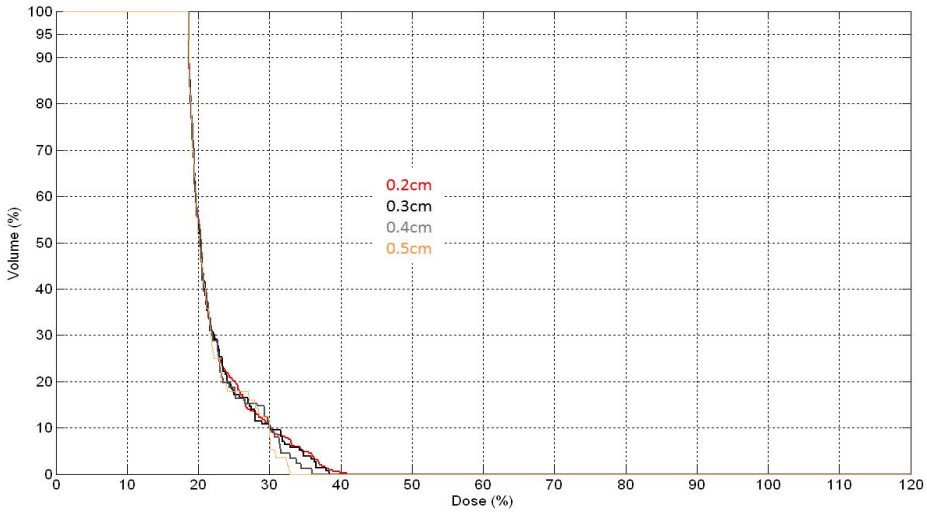

Figure 4.5: OAR DVHs plotted using the voxel sizes from 0.2cm to 0.5cm. Although about 5cGy difference of the maximum OAR dose between the 0.2cm and 0.4cm DVHs, the 0.4cm is the smallest OAR voxel size that does not run out of memory during the calculation involving both the PTV and the OAR.

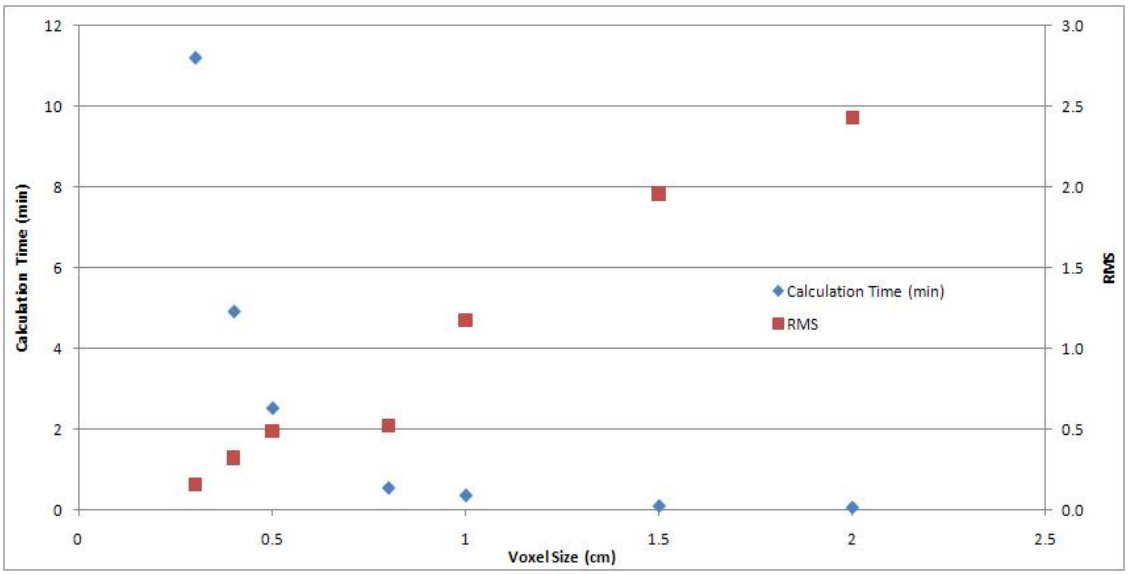

Figure 4.6: The normalized matrix calculation time and the RMS versus OAR voxel size.

voxel size for the PTV was 0.7cm and for the OAR was 0.4cm.

It was noted that for similar number of dose points, the RMS of the OAR was always larger than the one of the PTV. Take the PTV voxel sizes of 0.5cm and OAR voxel size of 0.3cm for example, the number of points inside the PTV was only 1.25% more than the number of points inside the OAR, but the RMS difference of the PTV is 56.3% better than the one of the OAR. One can also observe from Figure 4.7 that the slope of the OAR RMS curve is greater than the one of the PTV RMS. This may be explained by that there is a steep dose gradient in the OAR, so the accuracy of the DVH depends more on the voxel size in the OAR case than in the PTV case.

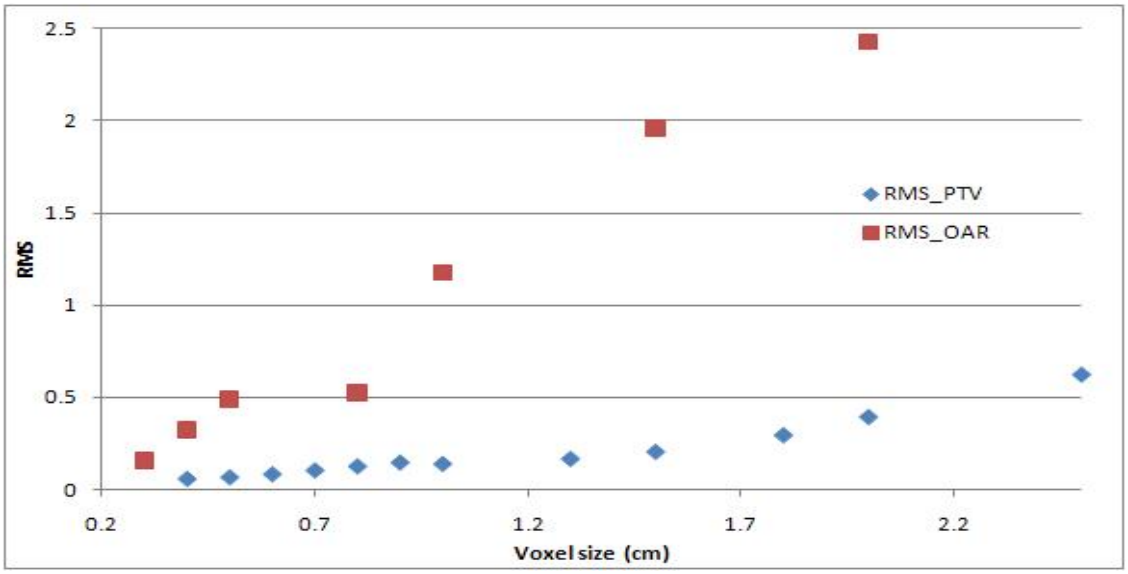

Figure 4.7: Comparison between the RMS difference of the PTV and the OAR.

4.3 Angle Step Size Analysis

2-step IMAT treatment is a rotational technique during which the target is irradiated continuously while the gantry rotates around the patient. Ideally an infinite number of beams is required to simulate such treatment, but it is not practical to do so. Therefore, only a finite number of beams is used during treatment planning to approximate the continuous treatment. In this analysis, the trade-off of using a finite number of beams in the TPS is investigated. The radiation is delivered every certain degrees and the angle separation between two adjacent beams is called the angle step size.

The number of beams used depends on the angle step size, i.e. the smaller the step size the higher the number of beams and the better the approximation. However, a large number of beams not only prolongs the time for the dose calculation, but also complicates the treatment plan optimization as the dimension of the optimization variable is defined by the number of beams (see Equation 3.1). The aim of this analysis is to find the appropriate angle step size for the 2-step IMAT treatment simulation, which gives a reasonable accuracy with as little calculation time as possible.

From the previous analysis, the voxel sizes of the PTV and the OAR were chosen to be $0.7cm$ and $0.4cm$, respectively, so that the doses can be calculated efficiently. The width of the second segment at each angle was fixed to $1.5cm$ and the ratio of two beams at each angle was kept at 1.5.

Treatment plans with different angle step sizes were generated in the Prism TPS, and the normalized matrix **M** was used to calculate the DVH of the PTV and the OAR in MATLAB. All the DVH plots were normalized to $D_{95} = 100cGy$. The number of beams and the time for the dose calculations were compared with the homogeneity index (HI) of the PTV. The HI is defined as the ratio of the maximum dose in the PTV to the PTV prescribed dose or the minimum dose in the PTV to the PTV prescribed dose [55], as shown in Equation 4.2 and 4.3.

$$HI_{max} = \frac{D_{max}}{D_{pres}} \tag{4.2}$$

$$HI_{min} = \frac{D_{min}}{D_{pres}} \tag{4.3}$$

$$HI_{diff} = HI_{max} - HI_{min} \tag{4.4}$$

For a perfectly conformal dose distribution, one expects the value of HI to be one, as the maximum and minimum doses correspond to the prescribed dose. In this work, the difference between the maximum and minimum HI was also used (see Equation 4.4) as an indication of the general homogeneity of the plan. The ideal value for HI_{diff} is zero, which corresponds to a uniform PTV coverage.

Since the simulation run out of memory for the 1° angle separation, the 2-step IMAT treatment plans were generated with the angle step size varied between 2° and 15°. The results of each run are listed in Table 4.3.

Angle Step Size(°)	2	3	4	5	10	15
Number of Beam Segments	612	412	304	244	124	84
Calculation Time (min)	21.74	14.64	10.81	8.69	4.43	3.07
$\mathbf{HI}_{max}$	1.1160	1.1179	1.1162	1.1191	1.1366	1.2402
$\mathbf{HI}_{min}$	0.9890	0.9896	0.9880	0.9886	0.9862	0.9719
$\mathbf{HI}_{diff}$	0.1271	0.1283	0.1281	0.1305	0.1504	0.2682

Table 4.3: Results of the angle step analysis.

The number of beams decreases as the angle step size increases, the time for the dose calculations follows a similar pattern as shown in Figure 4.8. Such result is expected as the more the number of beams the longer the dose matrix calculation time, since the column number of the matrix **M** in Equation 3.1 represents the number of beams.

Figure 4.9 shows the plot of the HI_{max} and the HI_{min} versus angle step size. As the angle step size decreases, the values of the HI_{max} and the HI_{min} approach unity which implies that the treatment plan becomes more homogeneous. This is due to the increased number of beams that conforms a better dose distribution for smaller angle step size. The difference

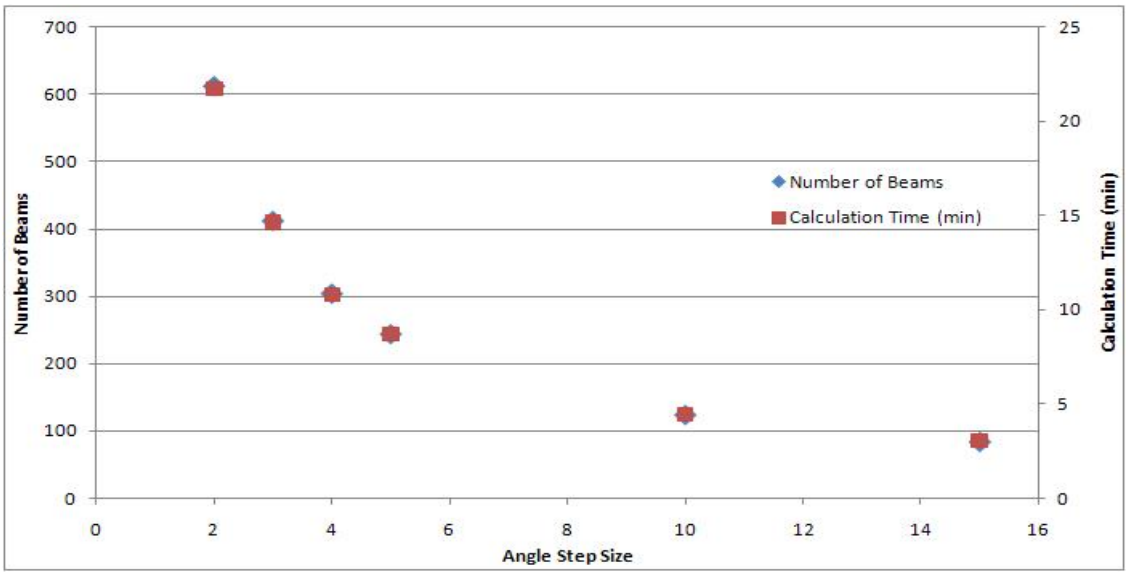

Figure 4.8: Dose calculation time and the number of beams decreases as the angle step size increases.

between the HI_{max} and the HI_{min}, HI_{diff}, is plotted in Figure 4.10. The curve suggests that the 5° angle step size may be a suitable choice for approximating the rotational treatment, since the value of the HI_{diff} does not improve significantly. The above can also be concluded from Figure 4.11, which is a plot of the calculation time versus HI_{diff}. Figure 4.11 illustrates that as the angle step size increases, the calculation time drops due to less number of beams, while the value of the HI_{diff} increases. The first four vertically distribution points represent the results of angle step size from 2° to 5° (refer to Table 4.3). The ideal solution of the curve is the one that gives minimum values for both axes but such solution does not exist in this case. The 5° angle step size was chosen, because the HI_{diff} only improves by 1.8% while the calculation time increases by 19.6% from 5° to 4°.

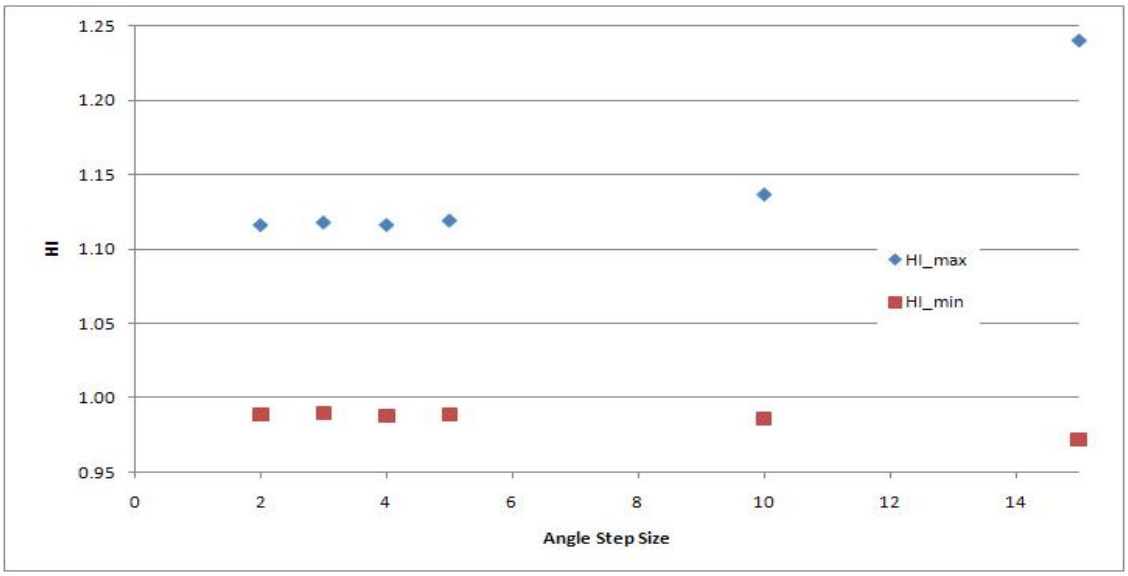

Figure 4.9: The homogeneity indices approach unity as the angle step size decreases.

Figure 4.12 shows the comparison between DVH of the 2° and 5° angle step size plan,

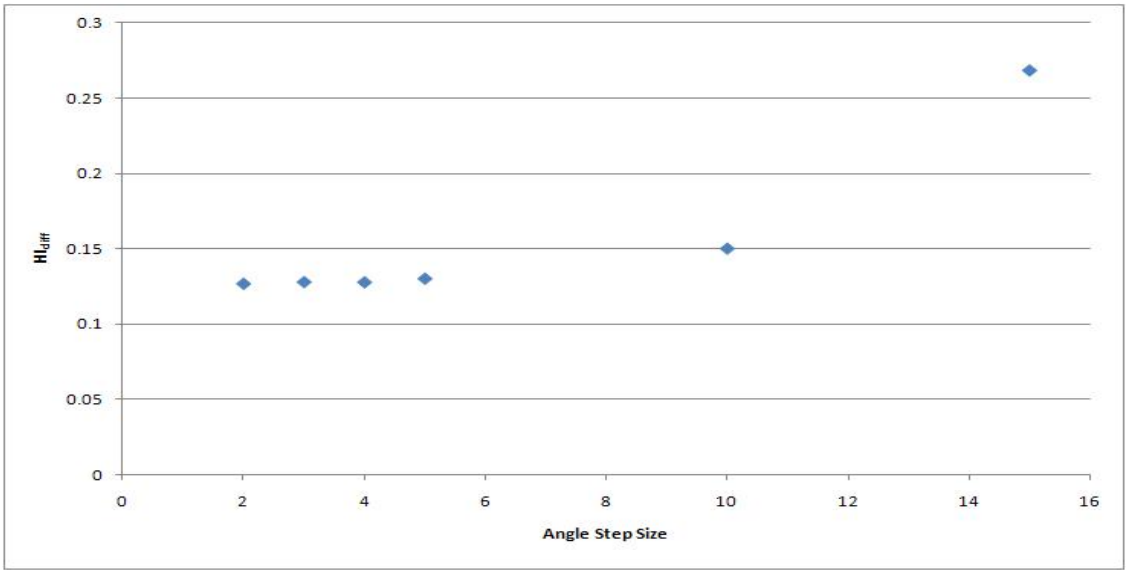

Figure 4.10: The homogeneity index difference approaches to approximately zero as the angle step size decreases.

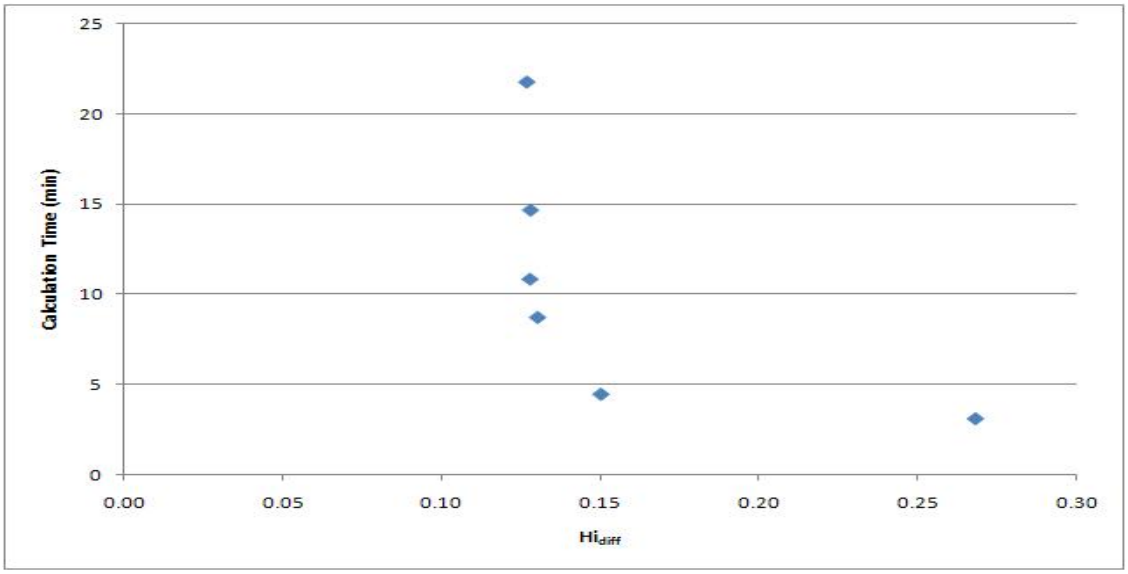

Figure 4.11: Graph of dose calculation time versus homogeneity index difference. The homogeneity index difference does not improve much as the angle step size smaller than 5°.

while Figure 4.13 shows the comparison between the DVH of the 5°, 10° and 15° angle step size plan. Assuming the 2° plan is the best approximation of a rotational treatment. Since the 2° and 5° plans are consistent with each other, this indicates that 5° is a good approximation of a rotational treatment. Considering in the number of beams, the 5° plan consists of only no more than 40% of the beam numbers of the 2° plan. As a result, the 5° plan requires less time to calculate the doses and optimize the beam weights for this reduction in the variable dimensions.

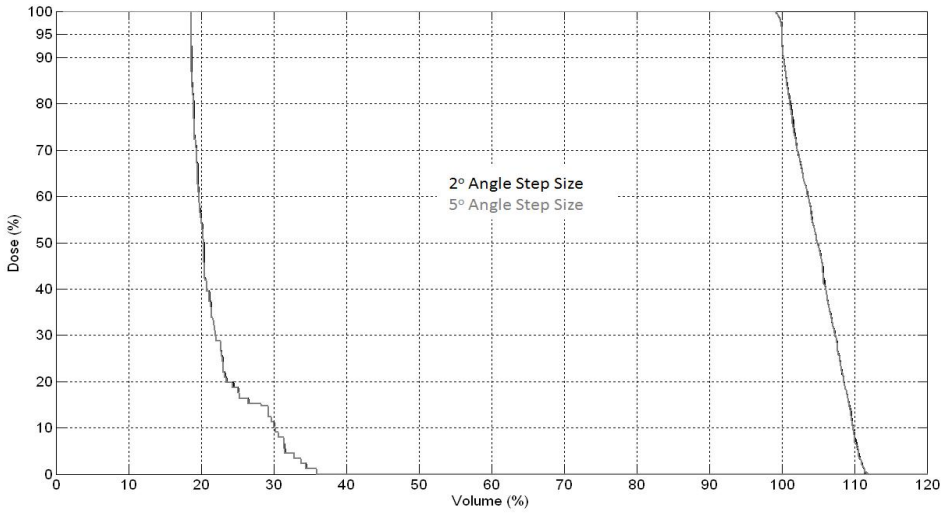

Figure 4.12: DVH comparison between 2° and 5°. (100% dose =100cGy)

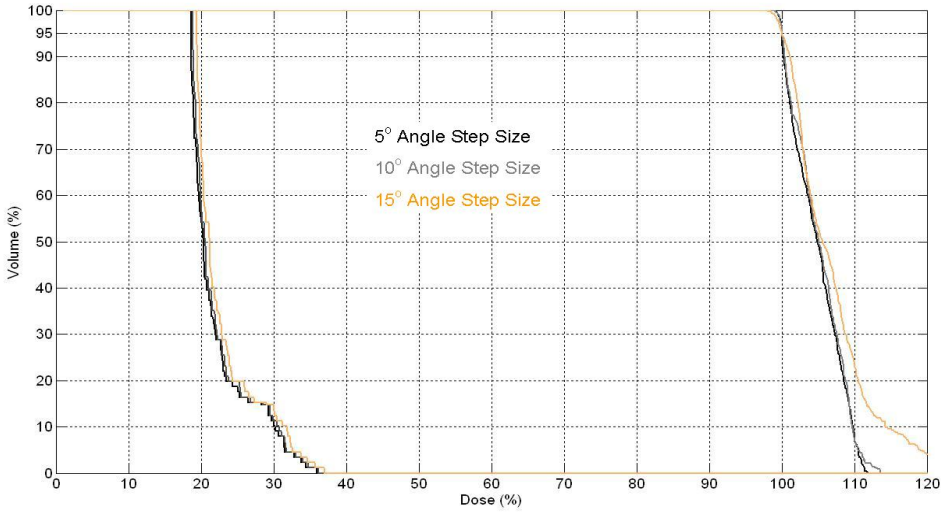

Figure 4.13: DVH comparison between 5°, 10° and 15°.

Using the homogeneity index and DVH, the angle step size was chosen to henceforth be 5° to approximate the rotational treatment during the simulation.

4.4 Segment Weight Ratio Analysis

One characteristic of the 2-step IMAT technique is its discrete approximation of the non-uniform beam intensity, see Figure 1.6. The ratio of the 2^{nd} order segment weight to the 1^{st} order segment weight is a parameter to be optimized for 2-step IMAT.

$$Weight\,Ratio = \frac{Weight_{2^{nd}segment}}{Weight_{1^{st}segment}} \tag{4.5}$$

The aim of this analysis is to find the effect of varying the fixed segment ratio on the resultant plan quality. The segment weight ratio that gives the best plan quality for the phantom will be used as a constant for later analysis. In Chapter 5, the segment weight will be optimized to increase the quality of the treatment plan.

The 2-step IMAT plans were simulated using a 5° angle step size and the second order beam segment width was set to $1.5cm$ at each angle. The dose points were sampled every $0.7cm$ in the PTV and $0.4cm$ in the OAR.

A MATLAB program was developed to calculate the doses and related parameters for segment weight ratio, in range of 0.1 to 2 in steps of 0.1. The MU of the beam segments were adjusted while keeping a constant ratio, so that the DVH of the PTV was normalized to $D_{95} = 100cGy$.

The related parameters of this analysis are listed in Table 4.4.

Segment Weight Ratio	**MU**$_{Total}$	D_{mean}	**HI**$_{max}$	**HI**$_{min}$	**HI**$_{diff}$
0.1	460.72	131.4	1.5208	0.8936	0.6272
0.2	476.02	127.3	1.4625	0.9025	0.5601
0.3	489.82	123.6	1.4102	0.9105	0.4997
0.4	502.31	120.3	1.3629	0.9178	0.4452
0.5	513.64	117.3	1.3200	0.9244	0.3956
0.6	525.40	114.8	1.2841	0.9329	0.3513
0.7	536.77	112.6	1.2524	0.9417	0.3108
0.8	548.39	110.8	1.2255	0.9517	0.2738
0.9	560.65	109.5	1.2035	0.9635	0.2399
1.0	572.28	108.2	1.1830	0.9748	0.2082
1.1	585.31	107.4	1.1679	0.9890	0.1790
1.2	597.54	106.6	1.1533	0.9892	0.1641
1.3	609.91	106.0	1.1408	0.9888	0.1520
1.4	621.91	105.4	1.1293	0.9887	0.1406
1.5	633.85	104.9	1.1191	0.9886	0.1305
1.6	645.34	104.5	1.1095	0.9857	0.1237
1.7	658.31	104.4	1.1188	0.9804	0.1383
1.8	670.05	104.2	1.1320	0.9738	0.1582
1.9	682.30	104.1	1.1463	0.9685	0.1778
2.0	693.72	104.0	1.1594	0.9628	0.1966

Table 4.4: Results of the segment weights ratio analysis.

As the segment weight ratio increases, the total number of MUs required increases linearly, as shown in Figure 4.14, while the mean dose of the PTV on the other hand decreases

as shown in Figure 4.15. A high mean dose indicates a poor dose uniformity as the plans were normalized to $D_{95} = 100cGy$. One wants to generate a plan with less number of MU while remaining the PTV mean dose at a low level. Based on the previous two graphs, it is not straightforward to select the segment weight ratio to use.

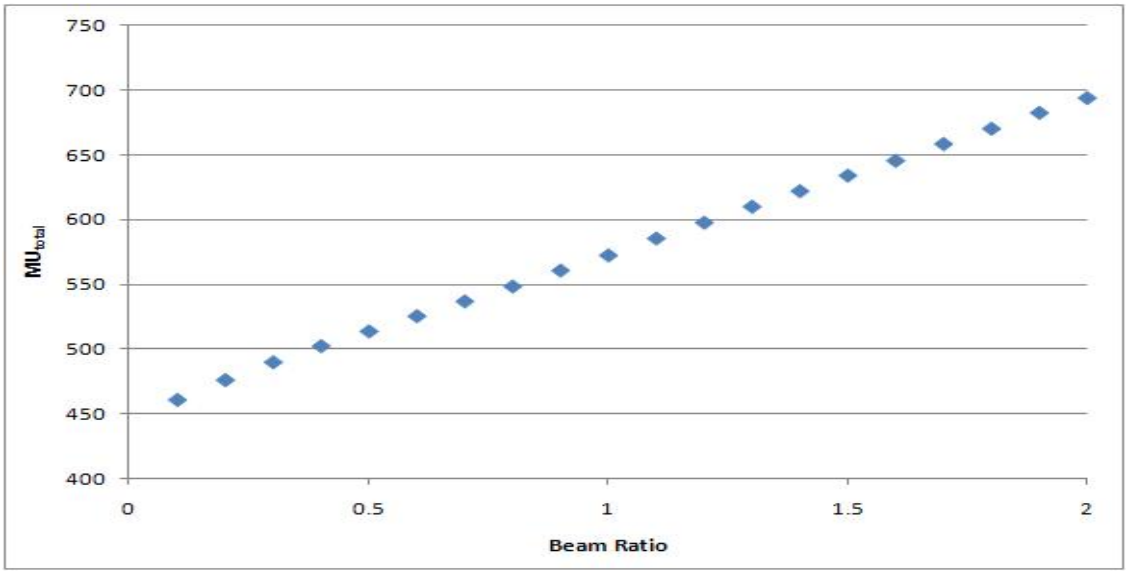

Figure 4.14: Linear relationship between the total MU and the segment weight ratio.

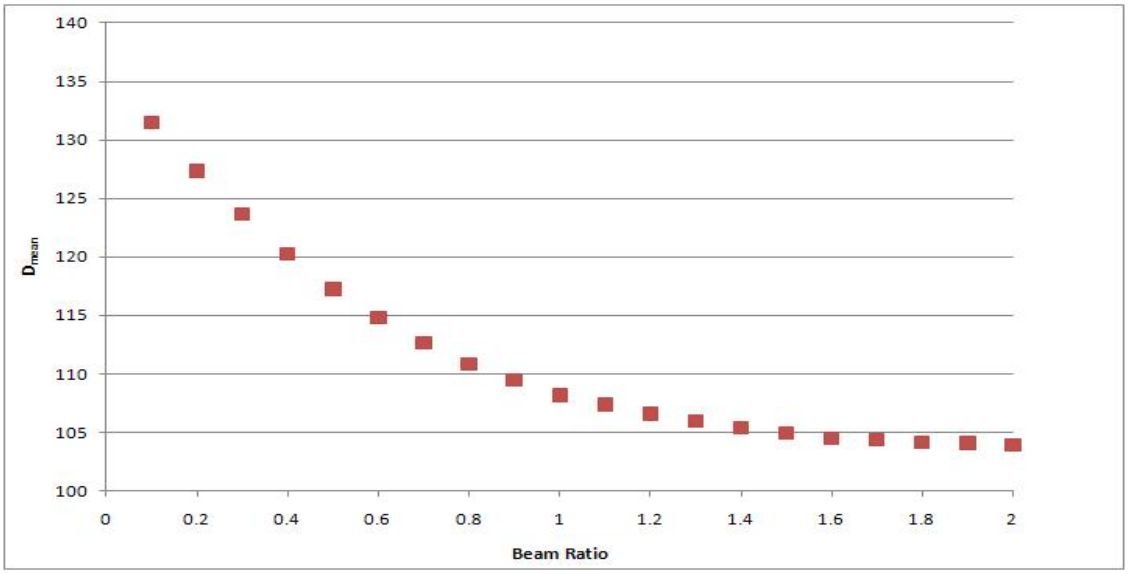

Figure 4.15: Decrease of the PTV mean dose as the segment weight ratio increases.

Figure 4.16 shows the curves of HI_{max} and HI_{min} versus the segment weight ratio. The curves indicate that a very low or high segment weight ratio degrades the plan quality. For HI_{min}, a ratio in the range between 1.1 and 1.5 is constantly close to the value one. While the value of the HI_{max} achieves a minimum at 1.6 segment weight ratio. The difference between HI_{max} and HI_{min} is plotted in Figure 4.17. The smaller the value of HI_{diff} the more homogeneous is the plan, since all plans were normalized to the same point on the DVH. Figure 4.17 suggests that by setting the segment weight ratio to 1.6, the plan becomes the most homogeneous.

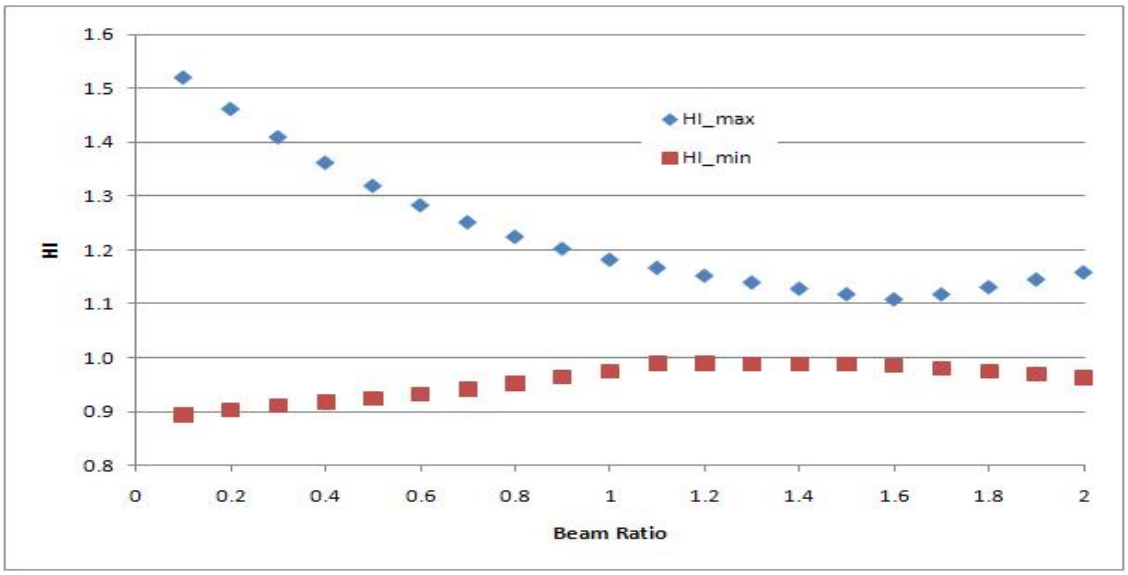

Figure 4.16: Changes in the HI_{max} and HI_{min} as the beam segment ratio increases.

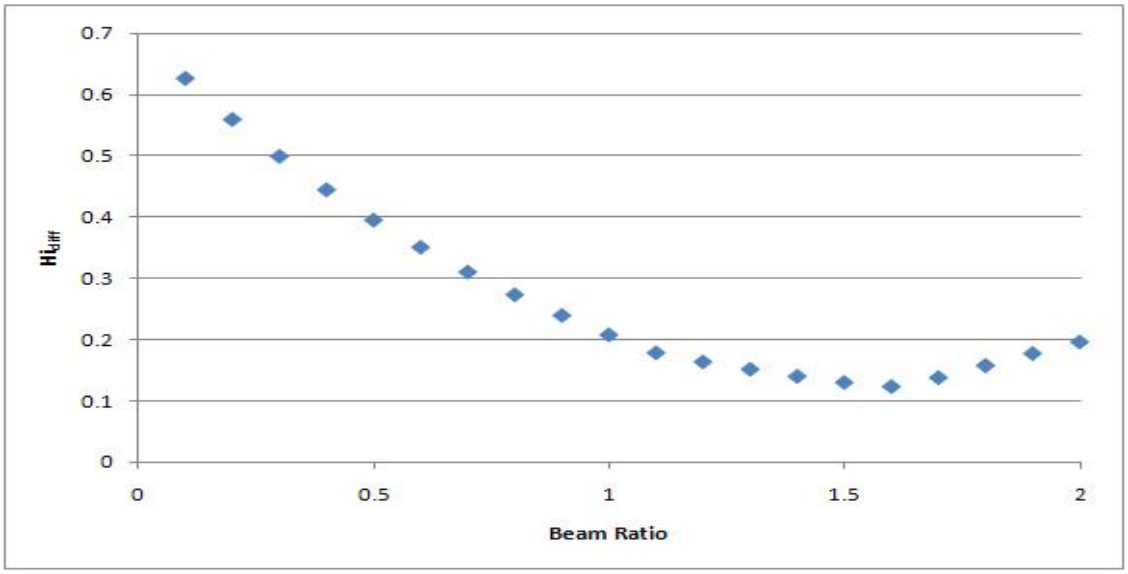

Figure 4.17: The difference of HI_{max} and HI_{min} as a function of beam segment ratio.

4.5 Second Segment Width Analysis

The 2-step IMAT technique uses two beam segments to approximate the effect of the physical filter. Since the width of the first order segment is fixed to cover the PTV, the width of the second order beam segment can be a parameter to change to achieve a plan with better quality. The aim of this analysis is to find the effect of the width of the second order segment on the quality of treatment plan for the phantom.

The segment weight ratio of the beams at each angle was set to 1.6 from the previous analysis and the beam angles were separated by 5°. Dose points were uniformly sampled using voxel size of $0.7cm$ in the PTV and $0.4cm$ in the OAR.

The gap between the PTV and the OAR was $1.0cm$ for the phantom. The second beam segment width was varied from $1.0cm$ to $2.0cm$. The plans were normalized to $D_{95} = 100cGy$

on the DVH as before. The MU_{Total}, HI, D_{mean} of the PTV and D_{max} of the OAR were recorded and compared.

Table 4.5 shows the results of the second beam width analysis. From this table it can be seen that solutions in the range $1.4cm$ to $1.7cm$ give best results. As a result, four extra widths ($1.0cm$, $1.3cm$, $1.8cm$ and $2.0cm$) were used to show the general trend.

2^{nd} **Segment Width** (cm)	$\mathbf{MU}_{Total}$	$\mathbf{D}_{mean}$	$\mathbf{D}_{OAR,max}$	$\mathbf{HI}_{max}$	$\mathbf{HI}_{min}$	$\mathbf{HI}_{diff}$
1.0	763.01	111.5	40.6	1.2208	0.9916	0.2291
1.3	679.44	106.5	37.6	1.1477	0.9906	0.1571
1.4	661.68	105.4	36.9	1.1280	0.9898	0.1382
1.5	645.34	104.5	36.3	1.1095	0.9857	0.1237
1.6	632.78	104.2	35.8	1.1158	0.9768	0.1390
1.7	620.89	104.0	35.4	1.1293	0.9684	0.1610
1.8	609.15	103.8	34.9	1.1410	0.9582	0.1828
2.0	590.16	106.6	34.9	1.1191	0.9311	0.2680

Table 4.5: Results of the second order beam segment width analysis.

Figure 4.18 shows the plot of the total MUs versus 2^{nd} beam segment widths. The dose delivery becomes more efficient as the 2^{nd} beam width increases. The mean dose in the PTV trend is shown in Figure 4.19, this general decreasing pattern is consistent with Figure 4.20 with the exception of the high mean dose for $2.0cm$ beam width. The cause of this increase of mean dose is due to the increasing underdose area in the PTV near the OAR. Figure 4.20 shows the graph of the maximum OAR dose versus the width of the 2^{nd} beam at each angle, its declining curve is consistent with the total MU curve in Figure 4.18. This consistency may relate to the setup of the beam portal of each segment. Since the MLC leaves are always pushed to the edge of the OAR regardless to the beam width, as the MU decreases the scattering contribution reduces and this is the reason of the gradually decrease in the OAR maximum dose.

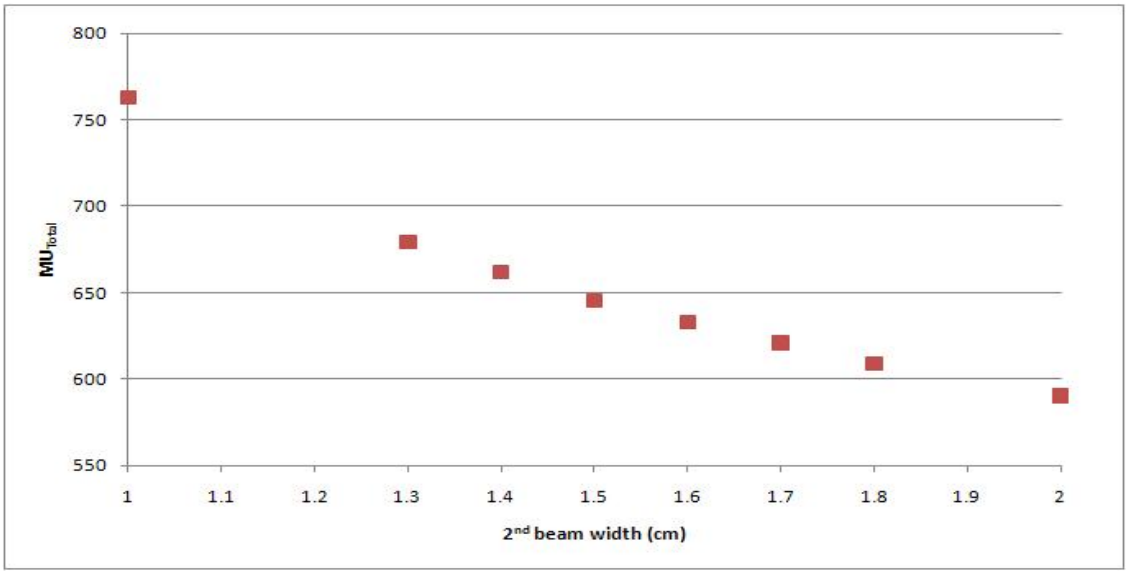

Figure 4.18: Decreasing trend of the total MU as the second segment width increases.

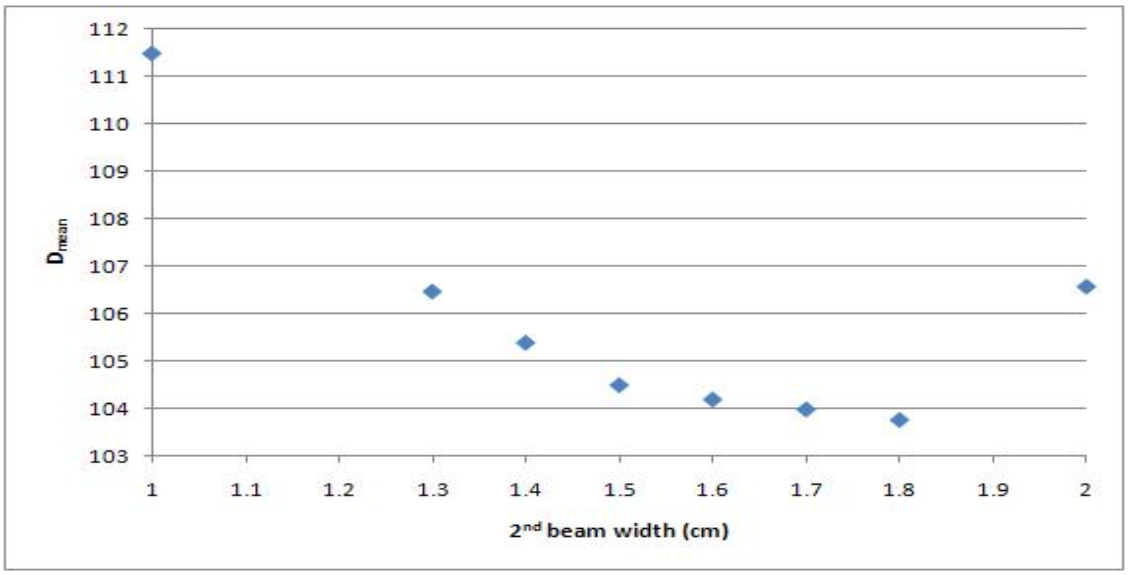

Figure 4.19: Mean PTV dose versus the second segment width.

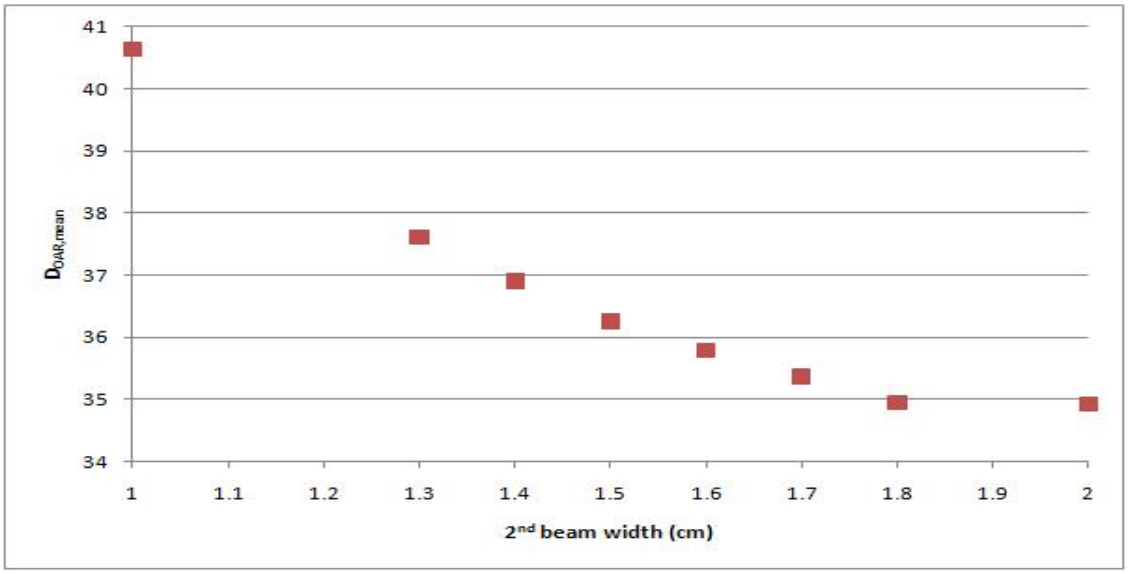

Figure 4.20: OAR mean dose decreases as the second segment width increases.

Figure 4.21 shows the comparison of the HI values. When normalized to $D_{95} = 100cGy$ on the DVH, the HI_{min} slowly decreases as the 2^{nd} segment width increases. On the other hand, the value of the HI_{max} achieves the minimum at $1.5cm$ in Figure 4.21. The homogeneity difference, HI_{diff} suggests that by setting the 2^{nd} segment width to $1.5cm$ the plan can be the most homogeneous in the absence of segment weight optimization.

Using the total MU, mean and maximum doses, the results of the 2^{nd} segment width ranging from $1.3cm$ to $1.8cm$ are consistent with each other and as the 2^{nd} segment width increases, the quality of the plan becomes better with regards to dosimetry. On the other hand, the results from the HI comparison suggests that the plan only can achieve its maximum homogeneity when the 2^{nd} segment width is set to $1.5cm$. One may use either methods to determine the suitable choice of the 2^{nd} segment width based on different aims, either reducing the dose to the patient or increasing the homogeneity in the PTV.

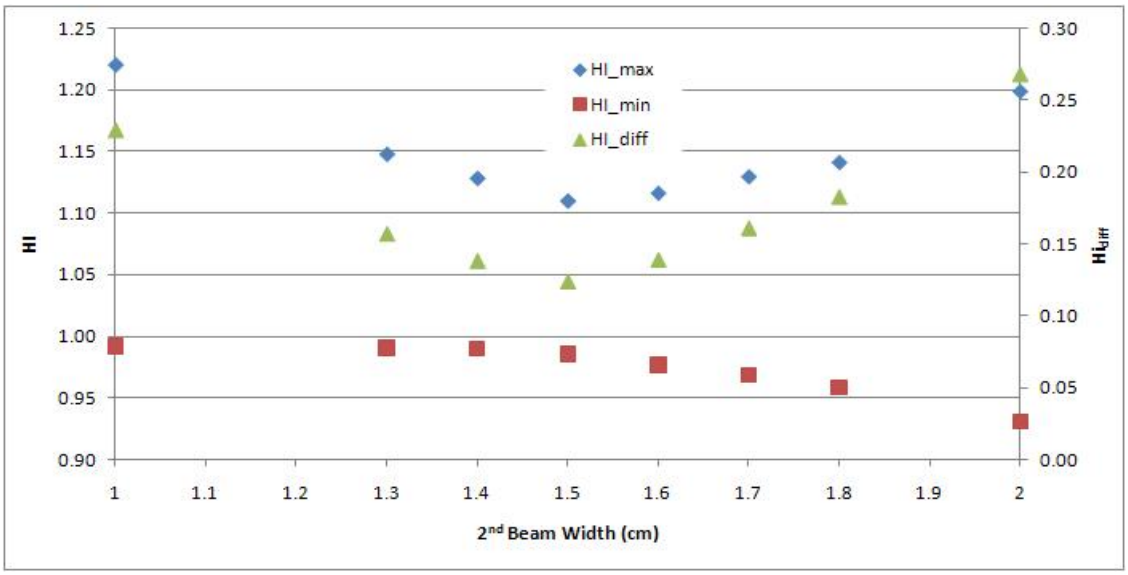

Figure 4.21: Effects of the change in second segment width on the homogeneity indices.

Figure 4.22 shows the DVH comparison of the 1.5cm and 1.8cm 2^{nd} segment width plans as an illustration of the homogeneity advantage of the 1.5cm plan.

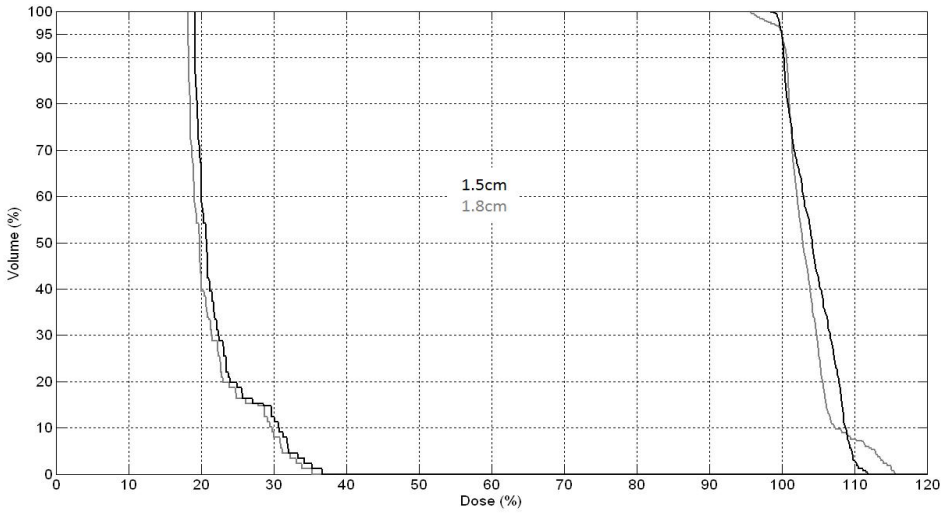

Figure 4.22: DVH comparison between the 1.5cm and 1.8cm 2^{nd} segment width plans. (100% dose =100cGy)

The 2^{nd} beam width was chosen to be 1.5cm for its higher homogeneity in the PTV. Such setup will be used in the next analysis to compare the effects of the number of rotations of the 2-step IMAT technique.

4.6 Rotation Number Analysis

As shown in Figure 2.5, there are two regions of the PTV not overlapping with the OAR, hence they are both suitable for 2-step IMAT irradiation. However, due to the physical

limitations of the MLC leaves, only one region can be irradiated at one time without rotating the MLC leaves. One can deliver radiation to both regions in two rotations with each rotation irradiating one side, or one may only irradiate one region in a single rotation to reduce the treatment time. In the case of 2-step IMAT, there are two segments for each irradiation region, so there will be four rotations required to deliver the ideal intensity profile shown in Figure 2.6.

The aim of this analysis is to find if there is any improvement in the quality of the treatment plan by doubling the number of rotations. In this work, the plan that delivers the "ideal" intensity profile as shown in Figure 2.6 is called "double side" (4-rotations) as it delivers the radiation to both PTV regions. The plan that delivers half intensity profile as shown in Figure 2.7 is called "single side" (2-rotations).

In this analysis, two 2-step IMAT treatment plans were generated with the same parameters selected in the previous sections. The voxel size of the PTV was $0.7cm$ and the voxel size of the OAR was $0.4cm$ for the dose calculation. The beam angles were sampled every $5°$. The beam segment ratio at each angle was fixed to 1.6 and the width of the second beam segment was set to $1.5cm$.

The only difference between the two treatment plans was that the "single side" plan only irradiates the PTV on one side of the OAR from every gantry angle, while the "double side" plan irradiates both regions of the PTV that do not overlap with the OAR. The beam segments are illustrated in Figure 4.23. The "single side" plan only requires two rotations to deliver the first and second order beam segments of the 2-step IMAT treatment, while the "double side" plan requires four rotations.

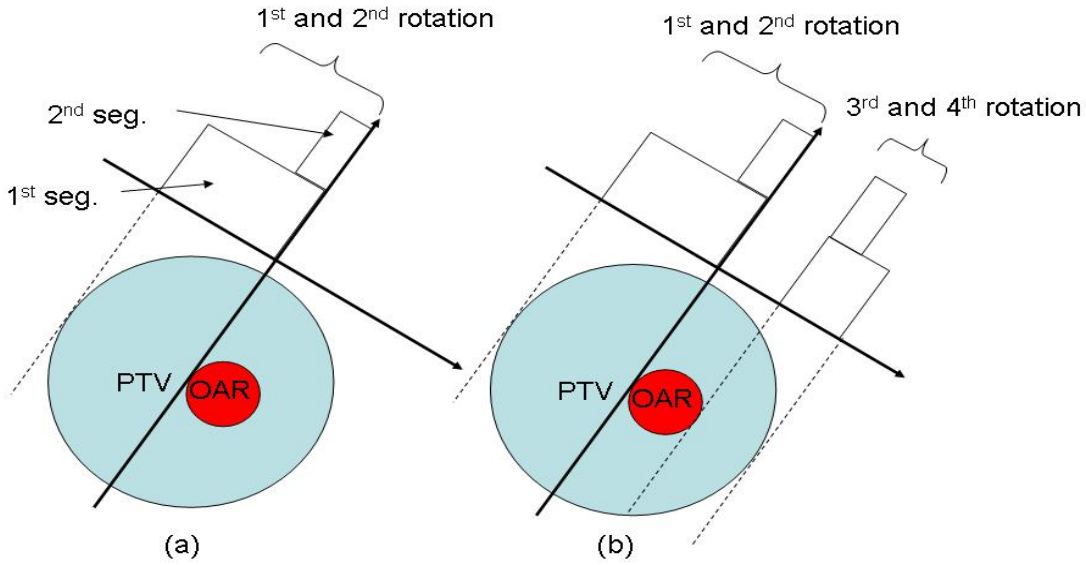

Figure 4.23: The "single side" plan (a) only irradiates one side of the PTV, while the "double side" plan (b) irradiates both sides of the PTV. For a 2-step IMAT, each segment requires one gantry rotation to deliver.

The normalized results are shown in Table 4.6.

It shows in the Table 4.6 that the dose calculation time of the "double side" plan is about twice of the one of the "single side" plan, since the number of beams is doubled. This may

	Single Side	Double Side	Change (%)
Number of Beams	112	244	NA
Calculation Time (min)	4.47	8.69	+48.6
$\mathbf{MU}_{Total}$	667.42	645.34	-3.3
$\mathbf{HI}_{max}$	1.1921	1.1095	-6.9
$\mathbf{HI}_{min}$	0.9128	0.9857	+7.4
$\mathbf{HI}_{diff}$	0.2793	0.1237	-55.7
$\mathbf{D}_{PTV,mean}$	108.0	104.5	-3.3
$\mathbf{D}_{OAR,max}$	49.0	36.3	-26.0
$\mathbf{D}_{OAR,mean}$	23.0	22.3	-3.3

Table 4.6: Results of the rotation number analysis.

be the most convincing argument for the speed advantage of the "single side" treatment plan. However, the rest of parameters all show the improvement by irradiating both regions of the PTV.

The total MU of the "double side" plan was 3.3% less than the one of the "single side" plan. Both HI_{max} and HI_{min} approach unity by around 7% after irradiating the other part of the PTV. The most significant of all is that the value of the HI_{diff} dropped by 55.7%, which indicates that the "double side" plan is more homogeneous than the "single side" plan. Such improvement in the homogeneity can be observed from the DVH of the two plans shown in Figure 4.24.

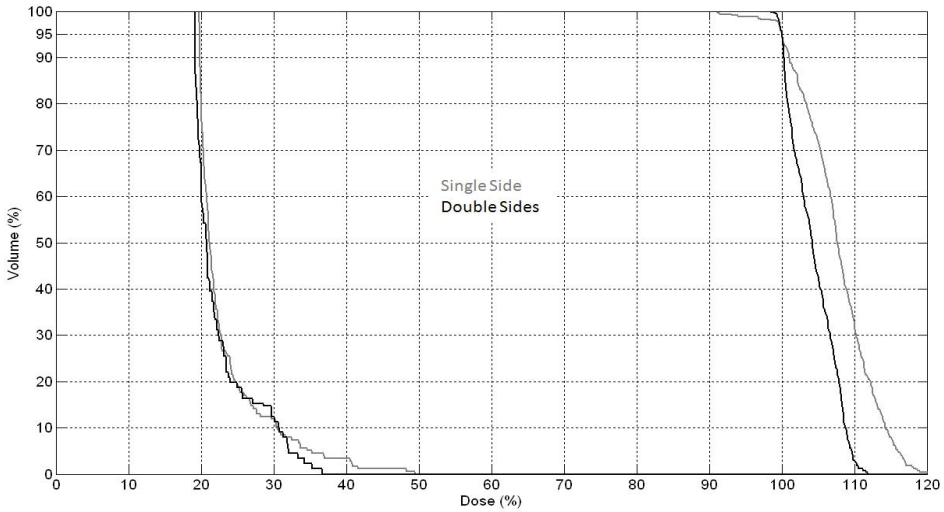

Figure 4.24: PTV and OAR DVH comparison of the "single side" and "double side" treatment plans. (100% dose =100cGy)

Dosimetrically, the "double side" plan is able to reduce the mean dose to the PTV and the OAR by about 3% and the maximum dose delivered to the OAR was reduced by 26%. These three parameters indicate that a more conformal does distribution can be achieved using the "double side" plan and the OAR can also be more spared.

The dose distribution shown in Figure 4.25 are the results from this analysis for "single side" and "double side" plans, respectively. The asymmetrical dose distribution in the "single

side" plan shown in Figure 4.25a results from delivering one side of the intensity bank as shown in Figure 2.7. Previous literature also indicated a similar asymmetrical pattern shown in the transversal plane, see Figure 4.26 [4].

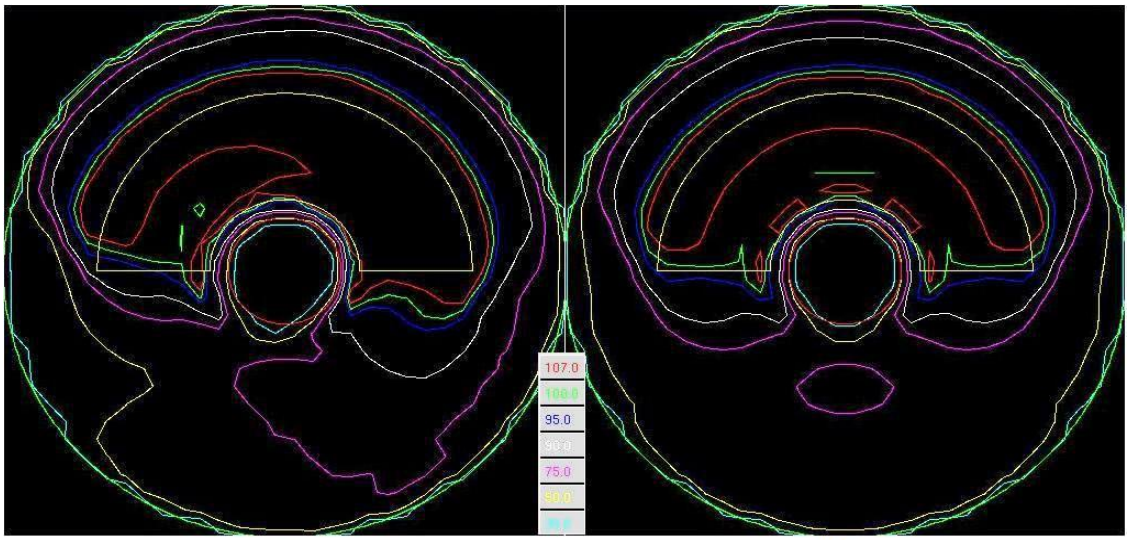

Figure 4.25: Dose distribution of the "single side" plan (a) and the "double side" plan (b). The improved symmetry can be observed. (red: 107cGy, green: 100cGy, blue: 95cGy, white: 90cGy, purple: 75cGy, yellow: 50cGy, cyan: 30)

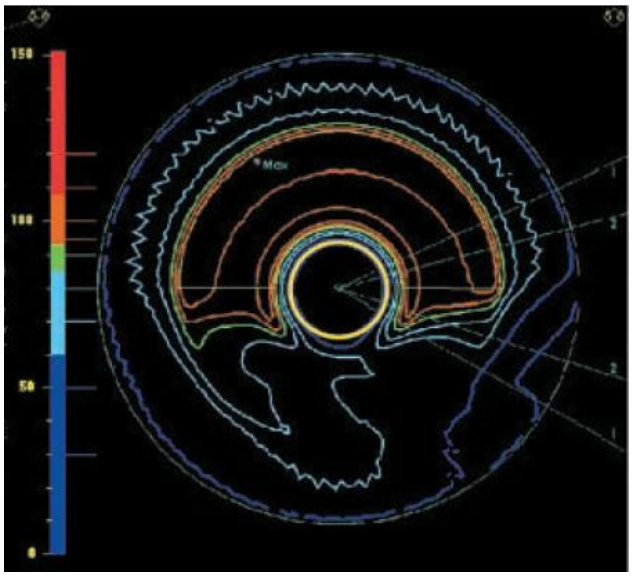

Figure 4.26: The dose distribution of a 2-step IMAT treatment plan from Bratengeier's paper [4]. The asymmetrical distribution of 70% to 80% isodose lines can be observed.

4.7 Concluding Remarks

In this chapter, the study on the 2-step IMAT was conducted in a geometric phantom based on the Bratengeier's previous literature [4]. The first analysis was to investigate the suitable

dose voxel size for dose sampling inside the phantom, because the voxel size affects the time and the efficiency of the dose calculation. Based on the analysis of the particular phantom used in this work, the voxel sizes of $0.7cm$ and $0.4cm$ were chosen for the PTV and the OAR, respectively. Since the irradiation is continuously delivered to the phantom during the gantry rotation but it is impractical to sample the beam in an infinitely small angle step size, an analysis was conducted to find a reasonable angle step size approximation which produce as few beam segments as possible while maintain the quality of the rotational plan. In a 2-step IMAT plan, there can be two parameters to adjust to improve the quality of the plan, the segment ratio between 1^{st} and 2^{nd} order segments and the width of the 2^{nd} order segment at each angle. The analysis in this chapter found that the segment ratio of 1.6 and 2^{nd} order segment width of $1.5cm$ provides the best plan quality. Finally, an analysis investigating the effect of the gantry rotation number on the quality of the plan was conducted. As the treatment delivers the ideal PTV coverage shown in Figure 2.6, the treatment time was doubled, but the homogeneity of the PTV dosage improved by more than 50% and the OAR was spared 26% more. In the next chapter, the treatment plan that is generated with the parameter setups found in this chapter will be optimized in term of segment weights, so that the quality of the plan can be improved.

Chapter 5

Segment Weight Optimization

The 2-step IMAT treatment plans generated in Chapter 4 had the segment weight ratio fixed. Such plans resulted in a high dose region at the edge of the PTV and some inner parts of the PTV as well (see Figures 4.24 and 4.25). Hot spots inside and outside the PTV reduce the general quality of the treatment plan. Therefore, treatment plan optimization is required to reduce this high dose and increase the uniformity of the PTV. In this work, both the dose-based and the dose-volume based objective functions were used to optimize the segment weights in order to further improve the quality of the plan.

5.1 Aim

The aim of this analysis was first to improve the plan quality of 2-step IMAT plans by optimizing the segment weight, i.e. MUs, of each beam using both the dose-based and the dose-volume-based objective functions. Secondly, the two optimization processes were compared in terms of time and achieved plan quality.

5.2 Method

The 2-step treatment plan with $1.5cm$ second beam segment width and 5° angle step size was generated in Prism. The plan was a "double side" plan, in which the gantry fully rotated around the phantom four times each time delivered one segment at an angle. The plan was then optimized using the dose-based and the dose-volume-based objective functions in MATLAB.

The parameters of the dose-volume-based objective functions are listed in Table 5.1, this optimization uses the objective functions shown in Equation 3.5, 3.6 and 3.7.

ω_{PTV}	ω_{OAR}	d_{cold}	V_{cold}	d_{hot}	V_{hot}	d_n	V_n
0.8	0.2	99.5	98%	102	70%	25	20%

Table 5.1: Dose-volume-based objective parameters setup. Name of parameters refers to Equations 3.5-3.7.

The parameters of the dose-based objective functions are listed in Table 5.2, this opti-

mization uses the modified dose-based objective functions, Equation 3.9, 3.10 and 3.11 in Section 3.4.2. For $\lambda = 1$, the optimization becomes the conventional dose-based objective function, which is shown in Equation 3.3, that considers the full range of the unsatisfied doses. On the other hand, the objective function terms only consider a partial range of the unsatisfied doses for $\lambda = 0.5$.

ω_{PTV}	ω_{OAR}	$\lambda_{PTV}/\lambda_{OAR}$
0.8	0.2	0.5 or 1

Table 5.2: The lambda-value-dose-based objective function parameter setup, the value of λ is set to 1 or 0.5.

5.3 Results and Discussion

The results are listed in Table 5.3. The non-optimized plan was compared with three different optimized plans, using the dose-volume-based objective function and the dose-based objective function algorithms, respectively. The last two columns are the results of the dose-based objective function, which uses the lambda-value-dose-based objective functions that uses the λ value to specify the dose range for the optimization.

	Non-Opt	**DV Opt**	**D Opt** (λ=1)	**D Opt** (λ=0.5)
Opt Time (min)	NA	11.9	2.3	1.8
Obj Value	NA	0.84	2.48	1.48
$\mathbf{MU}_{Total}$	645.34	683.70	605.23	612.47
$\mathbf{HI}_{max}$	1.1095	1.0480	1.0480	1.0545
$\mathbf{HI}_{min}$	0.9857	0.9830	0.9860	0.9830
$\mathbf{HI}_{diff}$	0.1237	0.0650	0.0620	0.0715
$\mathbf{D}_{PTV,mean}$	104.5	101.8	102.3	102.2
$\mathbf{D}_{OAR,max}$	36.3	44.7	33.1	36.4

Table 5.3: Results of the non-optimized plan (Non-Opt) and the plans optimized using dose-volume-based optimization (DV Opt) and dose-based optimization (D Opt).

As shown in Table 5.3, after optimization the quality of the treatment plan has generally improved in different aspects for different objective functions. The values of the HI_{diff} are about halved after the optimization, in other words, the dose distribution inside the PTV becomes more conformal after the optimization. Such effect can be observed in Figure 5.1, which shows the DVH of the non-optimized plan and the plan optimized using dose-based objective function with $\lambda = 1$ as an example. The improved homogeneity reduces the PTV volumes that receive high doses. The total MU after the dose-based objective function is reduced by about 6% and a general dose reduction in the OAR (see Figure 5.1). Because the beam segments of all treatment plans are the same and the MLC leaves on the OAR side shadow the OAR completely, less MU leads to less radiation leakage into the OAR through the MLC leaves. Such relationship between the MU and the maximum OAR dose can also be observed by comparing the DVH of the non-optimized plan with the plan optimized using the dose-volume-based optimization shown in Figure 5.2. Values from Table 5.3 shows

that the total MU in fact has increased by 31.9% after the dose-volume-based optimization, and this results a 18.8% increase in the OAR maximum dose in Figure 5.2. In general, the optimization is able to improve the PTV dose uniformity, the following analysis will compare the plan qualities of different objective functions.

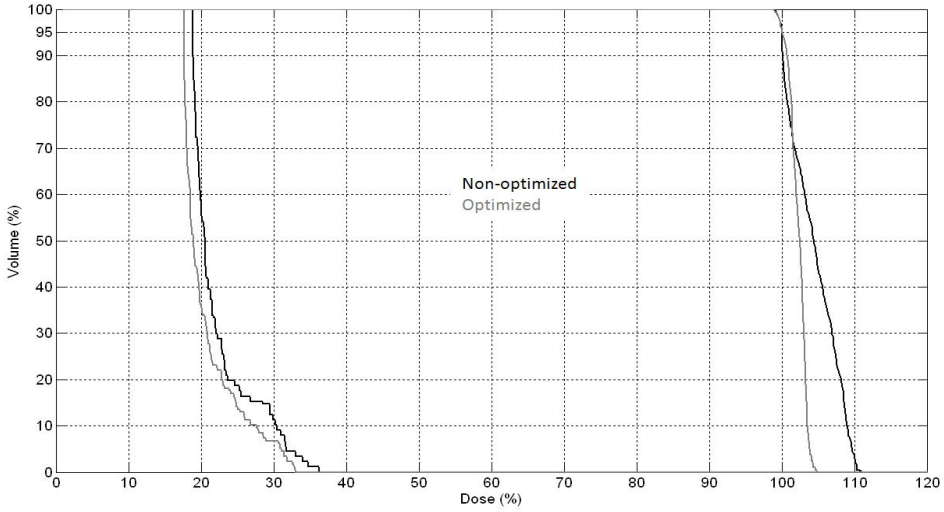

Figure 5.1: DVH comparison between non-optimized plan and the plan optimized using dose-based objective function. ($\lambda = 1$) (100% dose =100cGy)

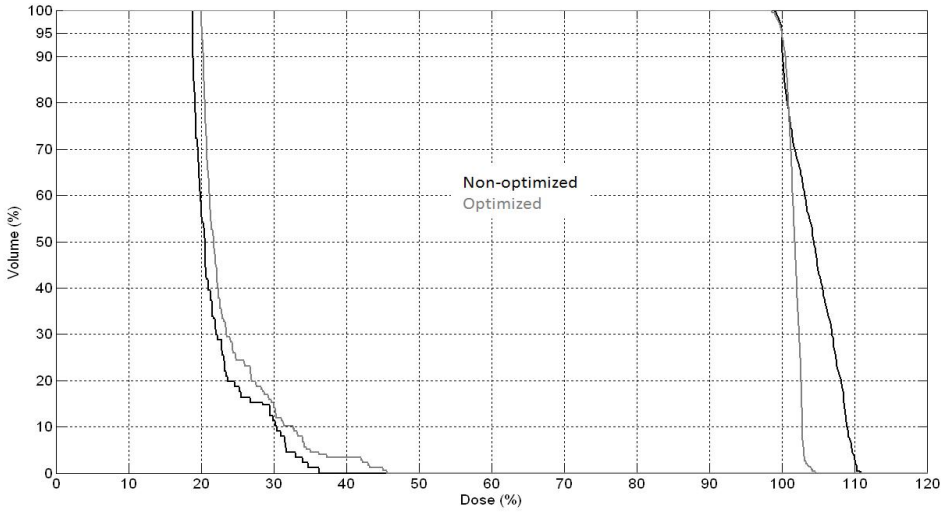

Figure 5.2: DVH comparison between non-optimized plan and the plan optimized using dose-volume-based objective function. (100% dose =100cGy)

The time taken to optimize the treatment plan is significantly different for the dose-volume-based and dose-based objective functions. Starting at the same starting point, the dose-volume-based objective function takes about six times longer to optimize the treatment plan than the dose-based optimization. This shows the speed advantage of the dose-based objective function. Additionally, the results of the dose-based objective function that includes the entire range of the unsatisfied doses (when $\lambda = 1$) are generally superior than

the dose-volume-based objective function results (see Table 5.3). Although using the dose-volume-based objective function is results 0.5% less mean dose in the PTV , the dose-based objective function is able to conform the dose distribution with 4.6% higher homogeneity.

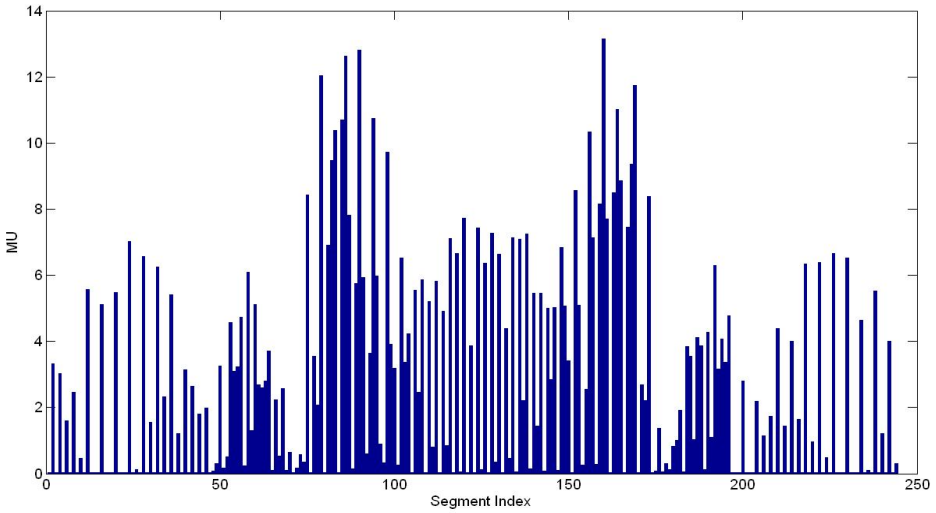

Figure 5.3: MU distribution of the plan optimized using the dose-volume-based objective function.

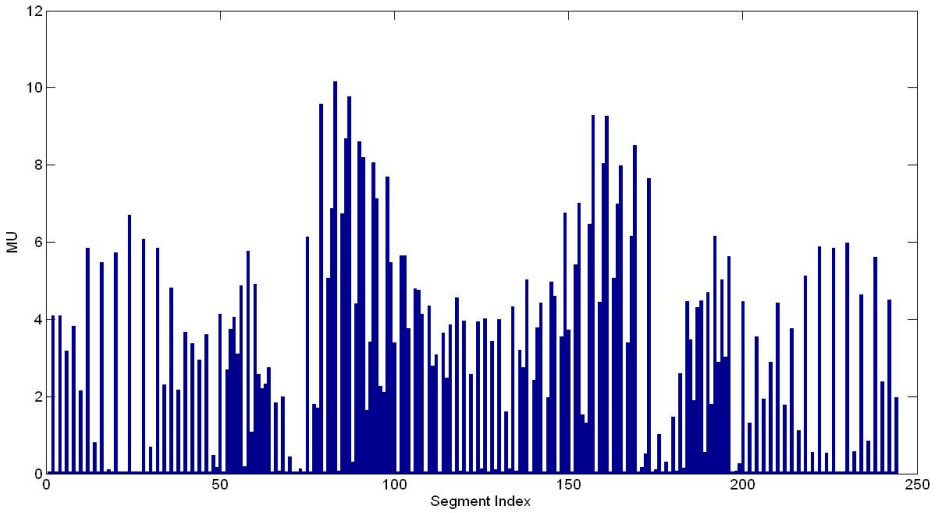

Figure 5.4: MU distribution of the plan optimized using the dose-based objective function. ($\lambda = 1$)

The total MU required by the plan optimized using the dose-based objective function was 11.5% less than the one optimized using the dose-volume-based objective function. As a result, the maximum dose inside the OAR was reduced by 30.0%. Figure 5.3 and 5.4 show the MU distribution of all the segments after dose-volume-based and dose-based optimization, respectively. The total number of the beam segments for both plans was 244. The gantry starts from 0° and rotates clockwise in a step size of 5°. At each angle, the number of beam segments is either four (two on each side of the PTV) or two (in situation when one side

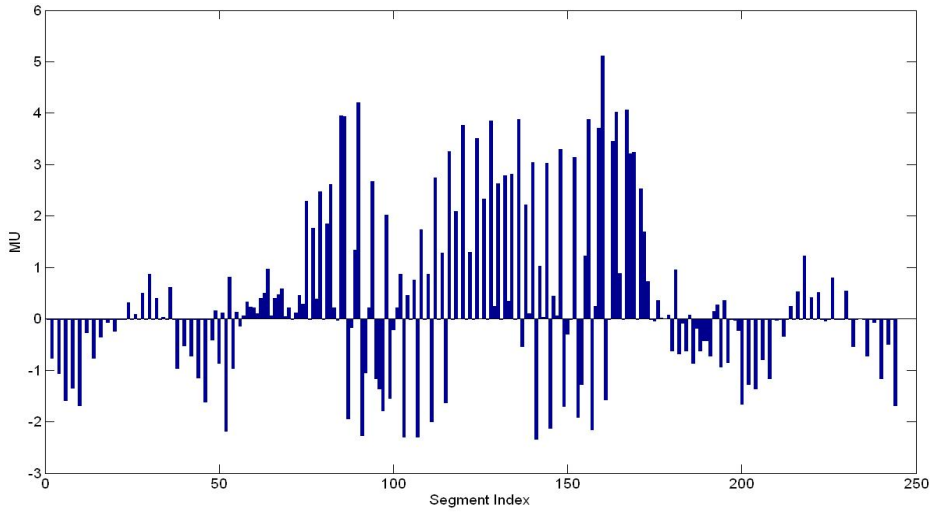

Figure 5.5: MU difference of the dose-volume-based and dose-based optimization.

of the PTV overlaps with the OAR). The two highest peak distributions of the MU values at the range between 80 and 100 and the range between 150 and 170 in Figure 5.3 and 5.4 represent the high MU of beams at gantry angle around 140° and 220°, respectively.

Figure 5.5 shows the difference between the MU distribution of the dose-volume-based and dose-based optimization. The reduction of the MU values at two peak regions and the increased MU values at other angles spreads the radiation more evenly around the phantom using the dose-based optimization. This results less radiation deposited into the lower part of the normal tissue, as shown in Figure 5.6, 5.7 and 5.8, which are the dose distribution after the dose-volume-based and dose-based optimization. Figure 5.9 shows the DVH comparison between these two plans and the slightly better OAR sparing due to the less total MU can be observed.

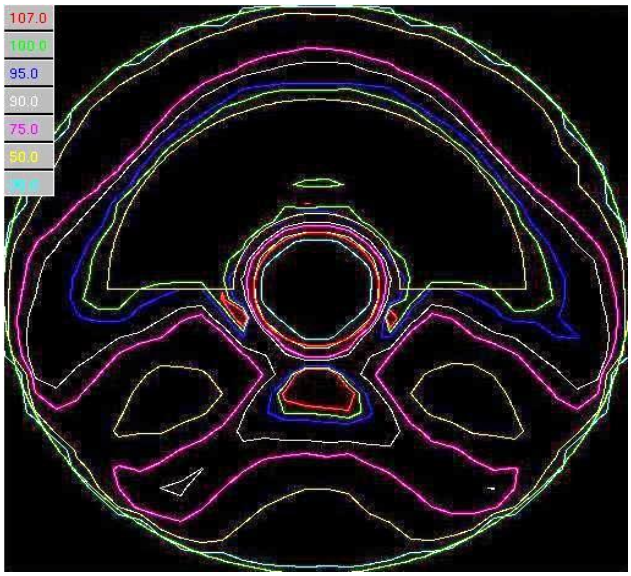

Figure 5.6: Dose distribution of the dose-volume-based optimized plan. (red: 107cGy, green: 100cGy, blue: 95cGy, white: 90cGy, purple: 75cGy, yellow: 50cGy, cyan: 30)

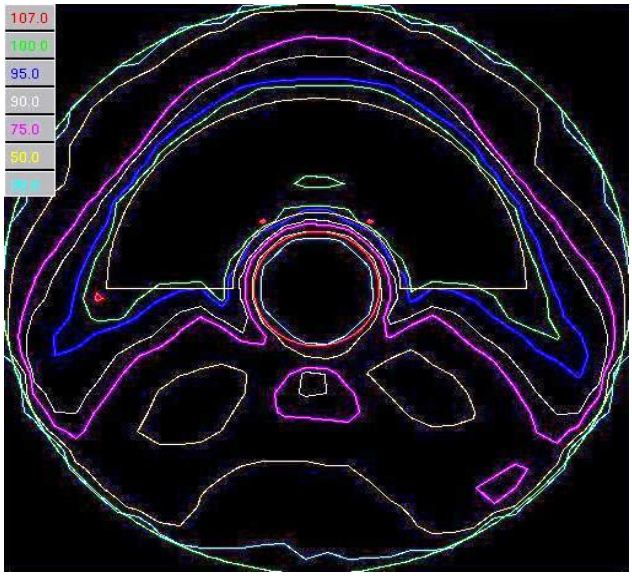

Figure 5.7: Dose distribution of the dose-based optimized plan ($\lambda = 0.5$). (red: 107cGy, green: 100cGy, blue: 95cGy, white: 90cGy, purple: 75cGy, yellow: 50cGy, cyan: 30)

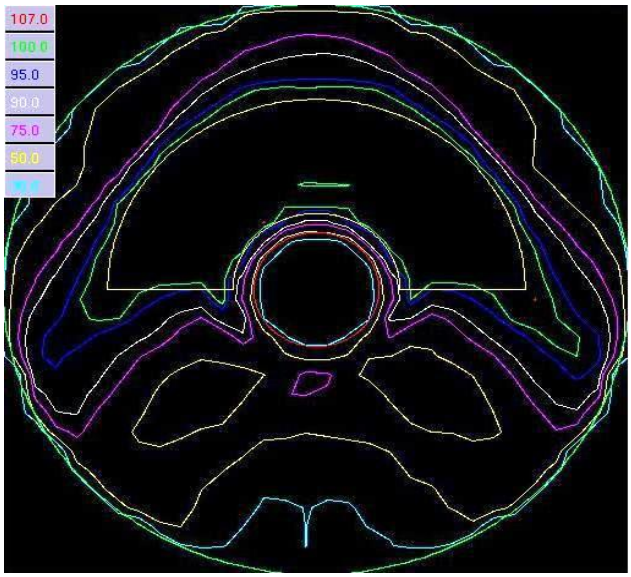

Figure 5.8: Dose distribution of the dose-based optimized plan ($\lambda = 1$). (red: 107cGy, green: 100cGy, blue: 95cGy, white: 90cGy, purple: 75cGy, yellow: 50cGy, cyan: 30)

The dose-based optimization is faster than the dose-volume-based optimization, this paragraph will compare the dose-based optimization that uses $\lambda = 1$ and $\lambda = 0.5$. By taking the full range of the unsatisfied doses, the quality of the plan can be improved more than only taking partial range of unsatisfied doses. The dose distribution shown in Figure 5.7 and 5.8 show the reduced doses to the normal tissue by setting λ to 0.5 and 1, respectively. Figure 5.10 is the DVH comparison of two λ settings and it visually presents the improved OAR sparing by setting $\lambda = 1$.

In general, both the dose-based and the dose-volume-based optimization algorithms are able to improve the quality of the treatment plan by increasing the steepness of the PTV DVH. Such improvement in the dose conformity of the PTV may compromise the sparing of

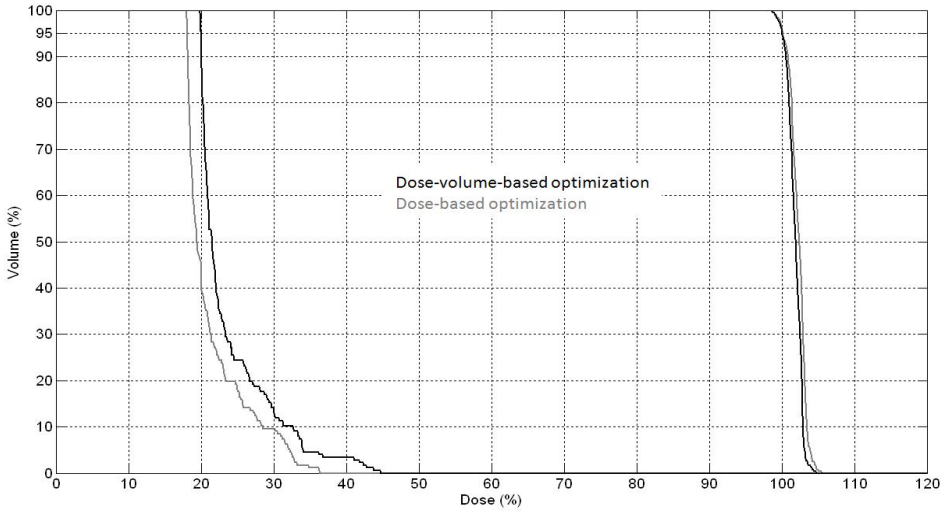

Figure 5.9: DVH comparison between dose-volume-based optimized plan and the plan optimized using dose-based optimization. ($\lambda = 0.5$) (100% dose =100cGy)

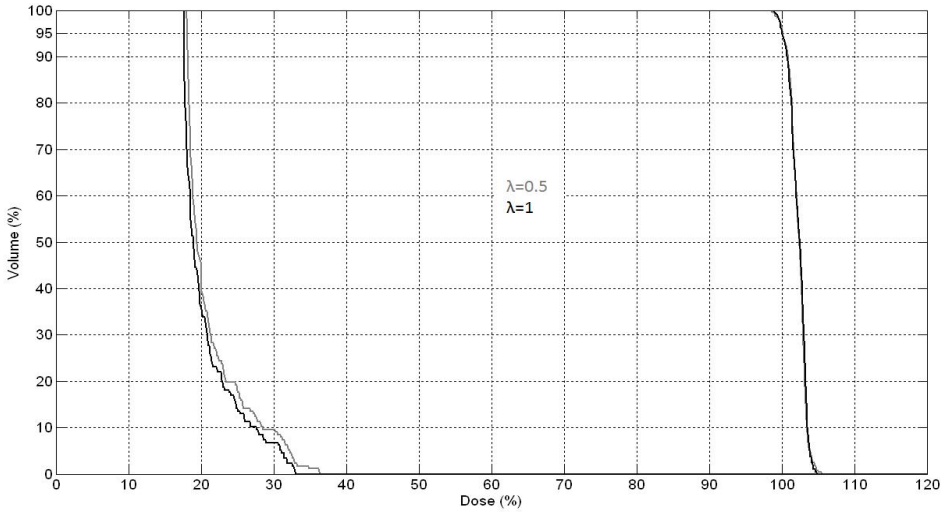

Figure 5.10: DVH comparison between the plans optimized using dose-based optimization. ($\lambda = 0.5$ and $\lambda = 1$) (100% dose =100cGy)

the OAR to some extent, but as long as the maximum OAR dose is within the tolerance dose the plan may still be acceptable. This increased maximum dose inside the OAR after the optimization may be the result of the lower value of the OAR weighting factor, ω_{OAR}, during the objective calculation. In the above analysis, the weighting factor of the OAR is set only one quarter of the weighting factor of the PTV, since the main goal of the optimization is to improve the homogeneity of the PTV dose distribution. As a result, the optimization may tolerate the unsatisfied doses in the OAR more than the PTV in turn lead to the increased maximum OAR dose. One solution may be to increase the weighting of the OAR so that the calculation of the OAR objective will contribute more in the optimization. Table 5.4 shows the results of the dose-based optimizations that use $\lambda = 0.5$ and two different settings of the

D Opt$_{\lambda=0.5}$	$\omega_{PTV} = 0.8$,$\omega_{OAR} = 0.2$	$\omega_{PTV} = 0.7$,$\omega_{OAR} = 0.3$
Opt Time (min)	1.8	2.0
Obj Value	1.48	1.33
MU$_{Total}$	612.47	600.51
HI$_{max}$	1.0545	1.0561
HI$_{min}$	0.9830	0.9825
HI$_{diff}$	0.0715	0.0736
D$_{PTV,mean}$	102.2	102.3
D$_{OAR,max}$	36.4	35.0

Table 5.4: Results of plans optimized using dose-based optimization ($\lambda = 0.5$) with different weighting factor setups.

weighting factors. As the value of the OAR weighting factor increases, the OAR becomes more important in the objective calculation. As a result, the maximum OAR dose is reduced by 3.8% which is 1.3 dose units less than the non-optimized plan. Such reduction is also linked to the smaller total MU of the newly optimized plan. Figure 5.11 shows the DVH comparison between the two ratio setups and Figure 5.12 shows the dose distribution of the plan by increasing the OAR weighting in the optimization.

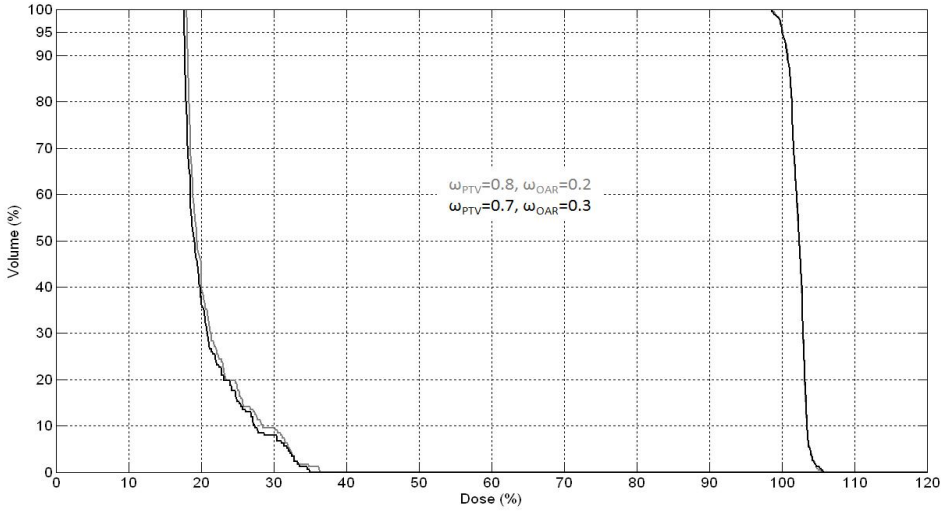

Figure 5.11: DVH comparison between the plans optimized using dose-based optimization ($\lambda = 0.5$) with different weighting factor settings. (100% dose =100cGy)

5.4 Concluding Remarks

In summary, the optimization is able to improve the uniformity of the PTV and reduces the dose to the OAR thus increases the quality of the plan. Comparing between dose-based and the dose-volume-based objective functions, the former algorithm is generally faster because it calculates the dose range (either full or partial range) one-dimensionally instead of doing so in a 2D space during every objective function calculation of the optimization. Furthermore, the

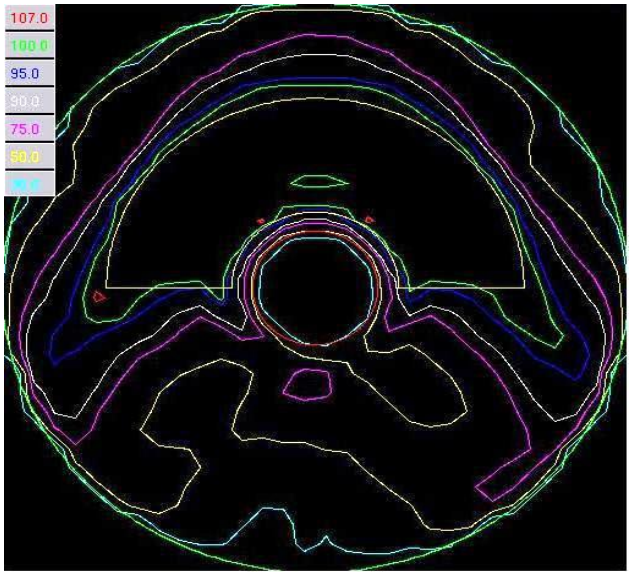

Figure 5.12: Dose distribution of the dose-based optimized plan ($\lambda = 0.5$, $\omega_{PTV} = 0.7$ and $\omega_{OAR} = 0.3$). (red: 107cGy, green: 100cGy, blue: 95cGy, white: 90cGy, purple: 75cGy, yellow: 50cGy, cyan: 30)

time required to optimize the plan is in the order of minutes. Such short time of optimization may be the result of a "fortunate" starting point and a "not-so-bad" local minimum. The lambda-value-dose-based objective functions developed in this work has the functionality to allow the planner to choose the range of unsatisfied doses to be considered in the objective function calculation. Such functionality makes the optimization more flexible, because the modified algorithm is able to relax the objective function calculation in situation when it is difficult to optimize using the full range of the unsatisfied doses.

Chapter 6

Clinical Study

In the previous chapters the segment generation and segment weight optimization have been addressed. For simplicity, the implementation of the above was tested on a semi-realistic geometrical phantom. In this chapter, the full implementation of 2-step IMAT was applied to a clinical case. Therefore, the aim of this part of work is to test the Prism and MATLAB codes on a clinical case and compare the 2-step IMAT plans with the conventional arc therapy plan.

6.1 Method

The clinical case used in this chapter is a paraspinal tumor case from the University of Würzburg. The original organs-of-interest include the PTV (concave shaped) and OARs (the spinal cord and both lungs). Due to the current implementation of the beam portal shaping program, only one PTV and one OAR can be taken into account. Therefore, the organs-of-interest in this work are the PTV and the spinal cord, as shown in Figure 6.1.

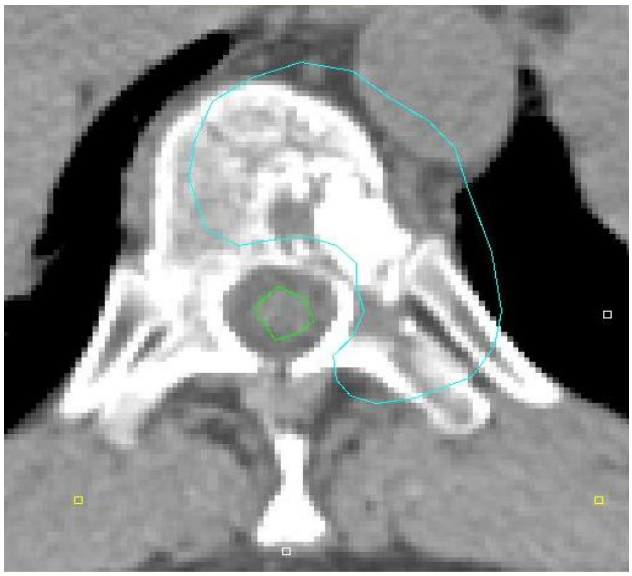

Figure 6.1: The transverse view of the PTV (cyan contour) and the spinal cord (green contour).

A conventional arc therapy treatment plan, which only delivers the first order beam segments shown in Figure 4.23b to cover the PTV at each angle, was created along with two types of the 2-step IMAT treatment plans, namely, two rotations (shown in Figure 4.23a) and four rotations (shown in Figure 4.23b). The beam angles were sampled every 5° and the dose points were sampled every $0.2cm$ and $0.1cm$ in the PTV and the OAR, respectively. The second segment width for the 2-step IMAT plan was $1.2cm$, which was chosen empirically so that the second segment was able to cover the gap between the PTV and the OAR as well as some inner part of the PTV.

The normalized matrix, $\mathbf{M}$ in Equation 3.1 was calculated in Prism and then transferred to MATLAB for optimization purpose. The segment weights were optimized using the dose-volume-based objective function as well as the lambda-value-dose-based objective function with the parameter values listed in Table 6.1 and 6.2. After the optimization, all plans were normalized to $D_{95} = 100cGy$ on the DVH.

ω_{PTV}	ω_{OAR}	d_{cold}	V_{cold}	d_{hot}	V_{hot}	d_n	V_n
0.8	0.2	99.5	98%	107	10%	45	5%

Table 6.1: Dose-volume-based objective function parameters setup. Name of parameters refers to Equations 3.5-3.7.

ω_{PTV}	ω_{OAR}	$\lambda_{PTV}/\lambda_{OAR}$
0.8	0.2	0.5 or 1

Table 6.2: The lambda-value-dose-based objective function parameter setup, the value of λ is set to 1 or 0.5.

6.2 Results and Discussion

The results of the conventional arc therapy after optimization are listed in Table 6.3. The results of the 2-rotation 2-step IMAT treatment plan after the optimization are shown in Table 6.4. The results of the 4-rotation 2-step IMAT treatment plan after the optimization are shown in Table 6.5.

Conv. Arc	**DV Opt**	**D Opt** $_{\lambda=1}$	**D Opt** $_{\lambda=0.5}$
Opt Time (s)	79.95	44.54	13.36
$\mathbf{MU}_{Total}$	301.0	292.2	293.0
$\mathbf{HI}_{max}$	1.1816	1.1540	1.1688
$\mathbf{HI}_{min}$	0.9056	0.8913	0.8964
$\mathbf{HI}_{diff}$	0.2760	0.2627	0.2724
$\mathbf{D}_{PTV,mean}$	107.0	107.5	107.5
$\mathbf{D}_{OAR,max}$	52.9	48.2	48.7

Table 6.3: Conventional arc therapy after the dose-volume-based optimization and dose-based optimizations.

Figures 6.2, 6.3 and 6.4 show the comparison of the DVH of different plans optimized by each objective function.

2 rotations	DV Opt	D Opt λ=1	D Opt λ=0.5
Opt Time (s)	130.09	39.96	30.88
$\mathbf{MU}_{Total}$	347.6	350.4	345.1
$\mathbf{HI}_{max}$	1.1082	1.1054	1.1113
$\mathbf{HI}_{min}$	0.9531	0.9121	0.9176
$\mathbf{HI}_{diff}$	0.1551	0.1933	0.1937
$\mathbf{D}_{PTV,mean}$	102.6	102.8	102.7
$\mathbf{D}_{OAR,max}$	53.8	44.4	46.2

Table 6.4: 2-rotation 2-step IMAT treatment plan after the dose-volume-based and dose-based optimizations.

4 rotations	DV Opt	D Opt λ=1	D Opt λ=0.5
Opt Time (s)	452.49	109.21	73.92
$\mathbf{MU}_{Total}$	325.5	333.7	325.2
$\mathbf{HI}_{max}$	1.0698	1.0736	1.0705
$\mathbf{HI}_{min}$	0.9366	0.9107	0.9125
$\mathbf{HI}_{diff}$	0.1332	0.1629	0.1580
$\mathbf{D}_{PTV,mean}$	102.0	102.3	102.2
$\mathbf{D}_{OAR,max}$	49.3	42.2	43.8

Table 6.5: 4-rotation 2-step IMAT treatment plan after the dose-volume-based and dose-based optimizations.

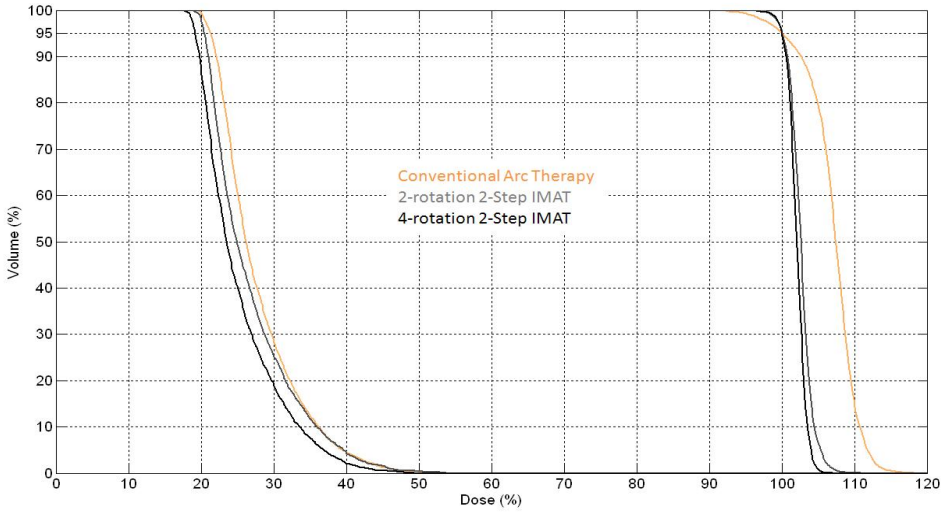

Figure 6.2: DVH comparison between the conventional arc therapy, 2-rotation and 4-rotation 2-step IMAT plans optimized by dose-volume-based objective function.

With the results shown in Tables 6.3, 6.4 and 6.5, the quality of the plan using different techniques were compared. The improvements in the maximum and minimum homogeneity indices and the decreases in the homogeneity indices difference indicated that the advantage of using the 2-step IMAT technique in unifying the PTV doses. For example, after the dose-volume-based optimization the homogeneity indices difference of the 2-step IMAT plans were about 40% and 50% lower than the one of the conventional arc therapy plan. The above

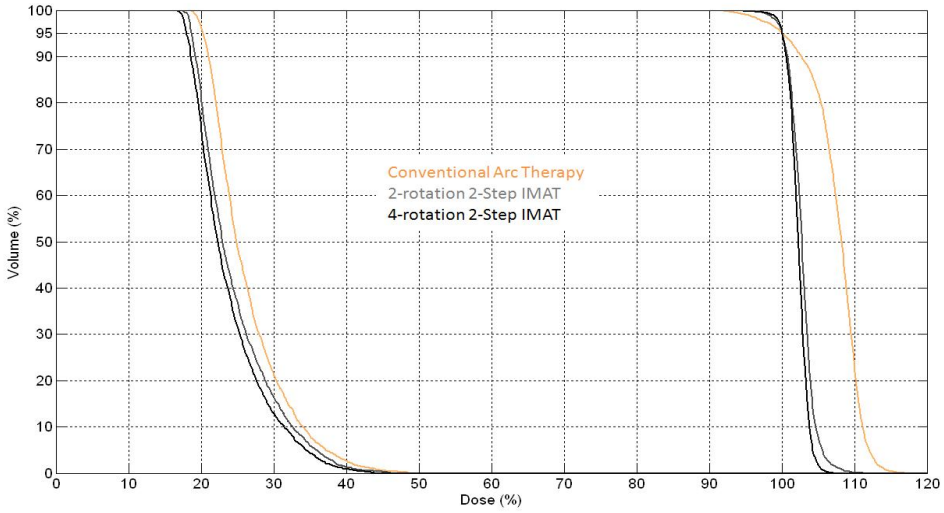

Figure 6.3: DVH comparison between the conventional arc therapy, 2-rotation and 4-rotation 2-step IMAT plans optimized by lambda-value-dose-based objective function. (λ=0.5)

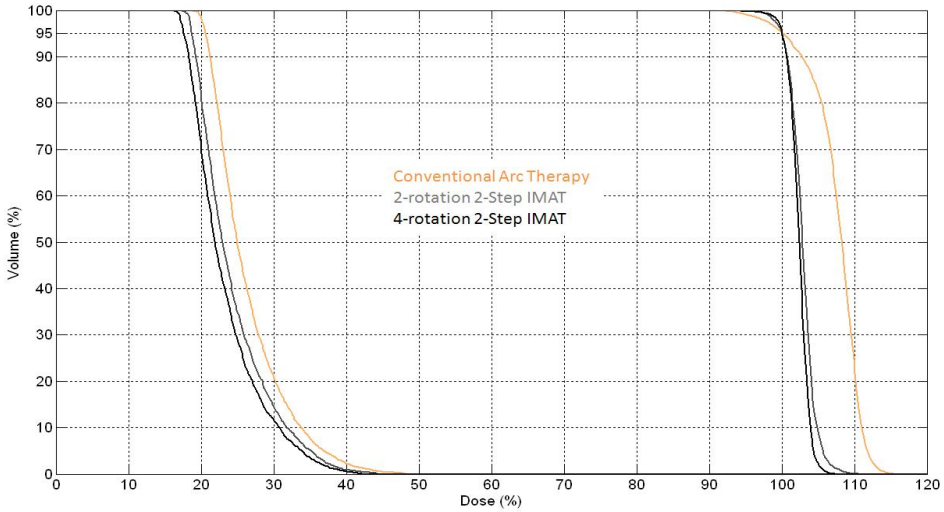

Figure 6.4: DVH comparison between the conventional arc therapy, 2-rotation and 4-rotation 2-step IMAT plans optimized by lambda-value-dose-based objective function. (λ=1)

improvements can also be observed from the DVH shown in Figures 6.2, 6.3 and 6.4 suggested consistently that the "extra" beam segment of the 2-step IMAT technique indeed improved the PTV dose uniformity. After the same optimization, the conventional arc therapy cannot achieve a PTV dose coverage as uniform as the 2-step IMAT plans. At the same time, the 2-step IMAT is able to spare the OAR slightly better than the conventional arc therapy.

It is worth to mention here that the number of beam segments of the conventional arc therapy and the 2-rotation 2-step IMAT plans were similar, both slightly over 100 segments (the former plan creates one segment for each side of the PTV in Figure 4.23b and the latter one creates two segments for one side of the PTV only in Figure 4.23a). Although the number of segments are similar, the 2-rotation 2-step IMAT was able to deliver a better

conformed plan due to the feature of the intensity modulation. As a proof-of-principle, this result agrees with the previous literatures of Bratengeier [4] and it shows the improvement of the plan quality by intensity modulation.

On the other hand, the conventional arc therapy requires less MUs to deliver, which implies that less MLC leakage dose during the treatment. However, due to the inhomogeneity of the conventional arc therapy, the mean dose of the conventional arc therapy plan is about 5cGy more than the mean dose of the 2-step IMAT plans. Depending on the optimization, the maximum OAR dose difference between the conventional arc therapy and the 2-step IMAT plans varies, but a general dose reduction in the OAR can be observed form the DVH shown in Figures 6.2, 6.3 and 6.4.

After the optimization, the beam segment weights were import back to Prism in order to determine the dose distribution of each plan. Figures 6.5 - 6.13 show the dose distributions of the transverse, coronal and sagittal planes for three types of the treatments after the dose-volume-based optimization.

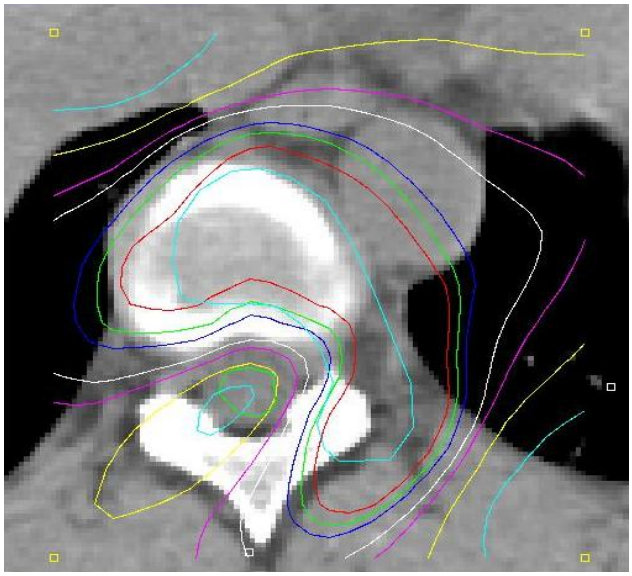

Figure 6.5: Dose distribution of the conventional arc therapy in the transverse plane. (red: 107cGy, green: 100cGy, blue: 95cGy, white: 90cGy, purple: 75cGy, yellow: 50cGy, cyan: 30)

In the transverse plane (Figures 6.5, 6.6 and 6.7), the conventional arc therapy was able to conform around the PTV but also resulted a "hot spot" around the PTV and nearby normal tissues. Conversely, the 2-step IMAT plans reduced the size of the "hot spot" within the PTV in order to achieve a uniform dose coverage. However, the optimization resulted high dose region in one side of lung. This compromise is mainly because of two reasons, the beam portal shaping program and the computer equipments limitation. The current beam portal shaping program in this work was only designed for one PTV and one OAR, none of lungs were avoided by beam segments, so the radiation to the lungs cannot be physically reduced using the MLC. Furthermore, due to the limitation of the current computer resource, the computation runs out of memory for too many dose points calculation in Prism. Therefore neither side of lung was taken into consideration during the optimization, since the dose

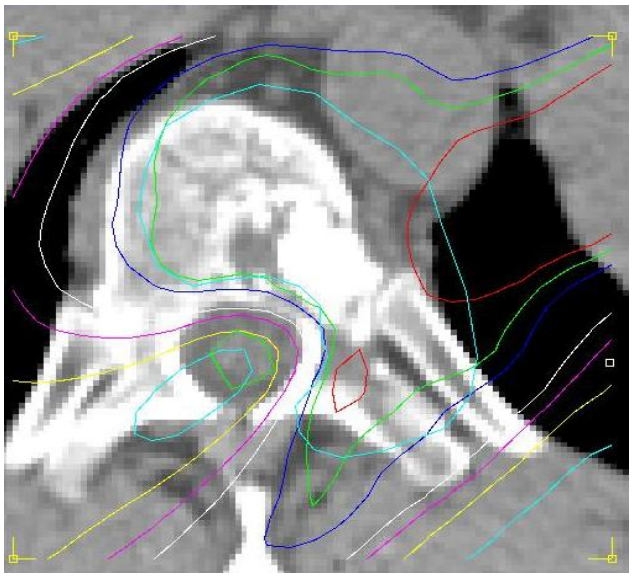

Figure 6.6: Dose distribution of the 2-rotation 2-step IMAT in the transverse plane. (red: 107cGy, green: 100cGy, blue: 95cGy, white: 90cGy, purple: 75cGy, yellow: 50cGy, cyan: 30)

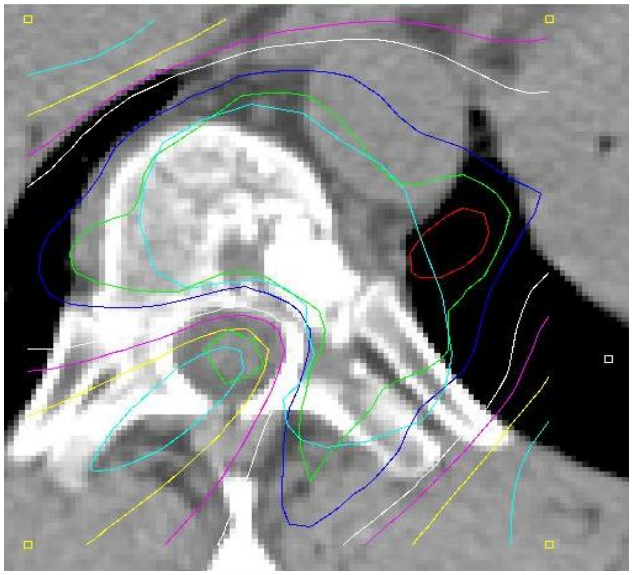

Figure 6.7: Dose distribution of the 4-rotation 2-step IMAT in the transverse plane. (red: 107cGy, green: 100cGy, blue: 95cGy, white: 90cGy, purple: 75cGy, yellow: 50cGy, cyan: 30)

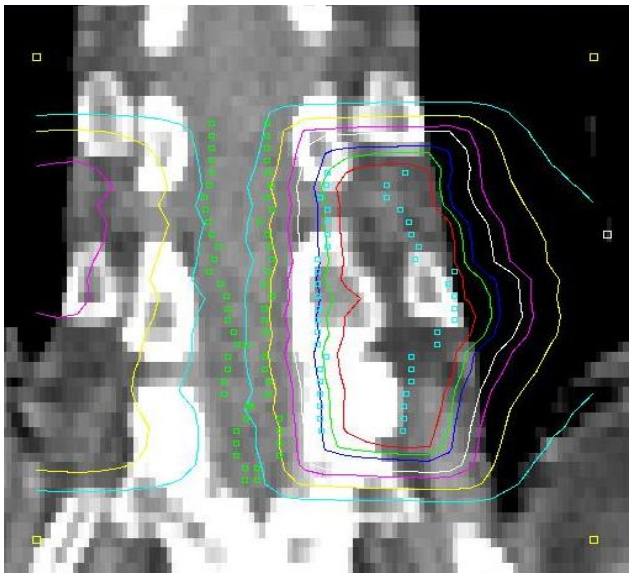

Figure 6.8: Dose distribution of the conventional arc therapy in the coronal plane. (red: 107cGy, green: 100cGy, blue: 95cGy, white: 90cGy, purple: 75cGy, yellow: 50cGy, cyan: 30)

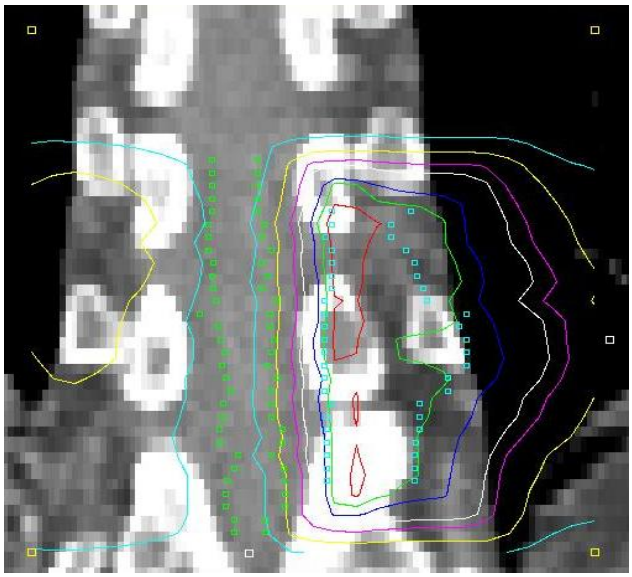

Figure 6.9: Dose distribution of the 2-rotation 2-step IMAT in the coronal plane. (red: 107cGy, green: 100cGy, blue: 95cGy, white: 90cGy, purple: 75cGy, yellow: 50cGy, cyan: 30)

Figure 6.10: Dose distribution of the 4-rotation 2-step IMAT in the coronal plane. (red: 107cGy, green: 100cGy, blue: 95cGy, white: 90cGy, purple: 75cGy, yellow: 50cGy, cyan: 30)

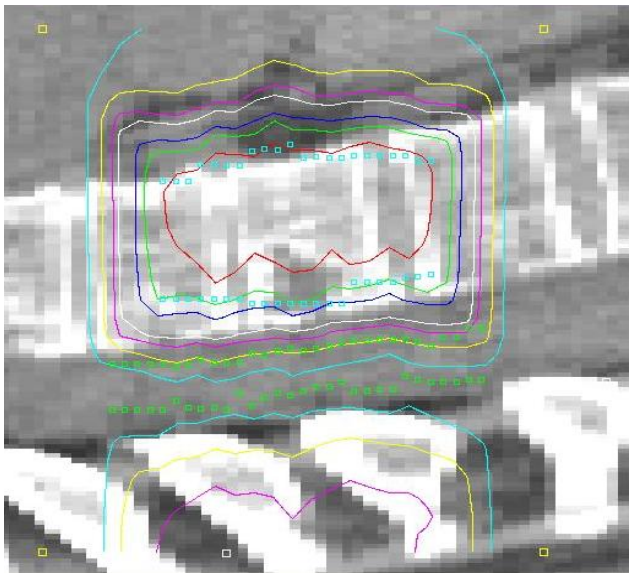

Figure 6.11: Dose distribution of the conventional arc therapy in the sagittal plane. (red: 107cGy, green: 100cGy, blue: 95cGy, white: 90cGy, purple: 75cGy, yellow: 50cGy, cyan: 30)

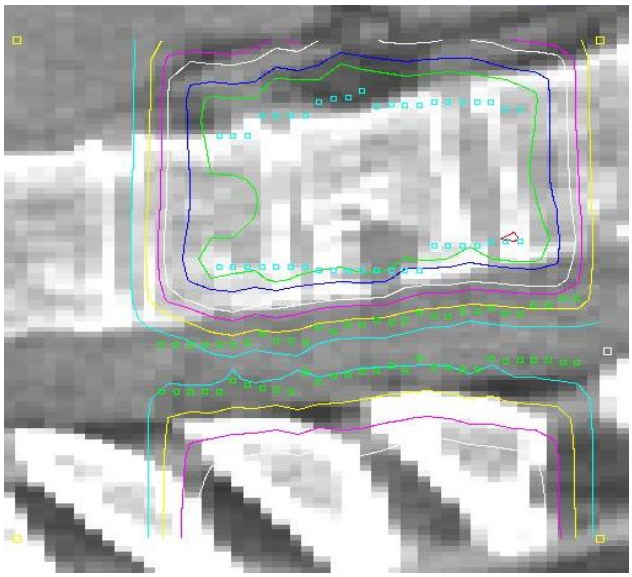

Figure 6.12: Dose distribution of the 2-rotation 2-step IMAT in the sagittal plane. (red: 107cGy, green: 100cGy, blue: 95cGy, white: 90cGy, purple: 75cGy, yellow: 50cGy, cyan: 30)

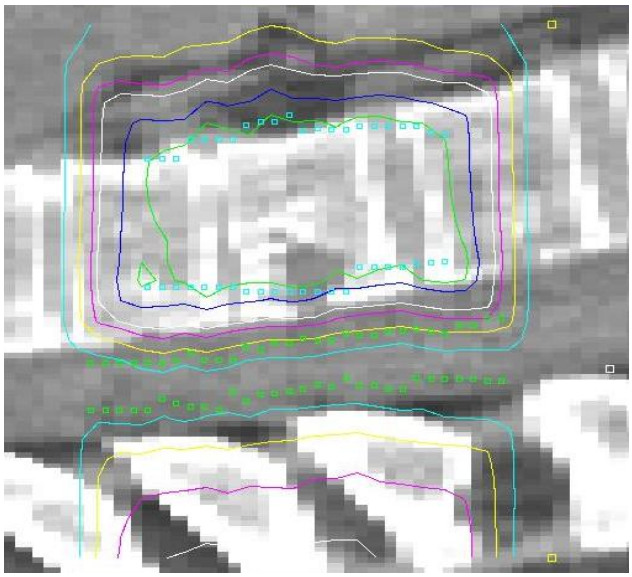

Figure 6.13: Dose distribution of the 4-rotation 2-step IMAT in the sagittal plane. (red: 107cGy, green: 100cGy, blue: 95cGy, white: 90cGy, purple: 75cGy, yellow: 50cGy, cyan: 30)

points matrix, **M**, for lungs has to be calculated first in Prism. In future work, both problems will be solved in order to improve the functionality of the 2-step IMAT implementation.

The "hot spot" region was also reduced in both the coronal and sagittal planes by using the 2-step IMAT technique (as shown in Figures 6.8, 6.9, 6.10, 6.11, 6.12 and 6.13). Such results agree with the DVH calculated in MATLAB and shows the advantage of the 2-step IMAT technique over the conventional arc therapy.

Comparing the two types of 2-step IMAT plans, the homogeneity indices difference of the 4-rotation plan was more than 10% better than the one of the 2-rotation plan. For the same optimization, the maximum OAR dose was decreased by about 5% to 8%. The improvements can also be observed on the DVH comparison in Figures 6.2, 6.3 and 6.4. The improvements can also be observed in the dose distribution, for example, the hot spot in the transverse plan was significantly reduced in the 4-rotation 2-step IMAT plan (see Figures 6.6 and 6.7).

With regards to the optimization time, the dose-volume-based optimization takes longer than the dose-based optimization, regardless to the type of treatment plan (refer to Tables 6.3 - 6.5). Furthermore, the relaxation in the dose-based optimization by reducing the value of lambda from 1 (considering the entire dose range) to 0.5 (considering partial dose range), the optimization time can be shortened while keep the quality of the plan similar.

6.3 Concluding Remarks

In summary, the work shown in this chapter demonstrated that the PTV dose uniformity advantage of the 2-step IMAT technique over the conventional arc therapy technique. This agrees with the results from the previous literature [4]. Furthermore, the implementation indicated that the 2-step IMAT program developed in this work has the potential to be applied to clinical cases. However, there are aspects of the program need to be improved in order for it to work for general cases. One urgently required improvement is to include more than one OAR in the treatment plan optimization. By increasing the computer memory and modifying the programming codes, the above problem can be solved in a future work.

Chapter 7

Discussion and Conclusion

7.1 Discussion and Future Work

In this work, the 2-step IMAT technique was implemented into the Prism TPS and a GUI was developed to allow the generation of 2-step IMAT plans in an automatic manner. The beam segments were created using a modified ray-tracing technique, which is able to generate beam segment shapes that avoid the OAR. This technique uses only the organ contours information, therefore the error due to spatial resolution of the point matrix that is created on the organ contour projection in the BEV (refer to Figure 2.3) can be eliminated. As a result, regardless of the size of the organ, any organ is "visible" in the BEV as long as there are contours plotted for the organ. However, the current implementation of the beam portal shaping technique has its limitation. It is only designed for cases consisting of one PTV and one OAR. It is an active area of future work to expand the current program code, so that the more organs can be considered during the beam portal shaping.

The dose grid size analysis suggested that a point grid size of $0.7cm$ and $0.4cm$ was accurate choice for the PTV and the OAR of the phantom, respectively, while conserving the calculation time and equipment resources. In this work, Common Lisp codes were developed to include the ability to calculate doses in different organs using different grid sizes. Such functionality is essential in order to provide equally accurate dose results for different size organs, especially when the size of the organ as well as the dose gradient is different. The angle step size analysis showed that in order to approximate the rotation treatment efficiently, the beam angle can be sampled every $5°$.

The 2-step IMAT technique uses two beam segments to approximate the ideal beam intensity profile as generated by a physical filter in Brahme's original work. As a result, during the treatment planning process there are two possible parameters that can be altered, the ratio of the two beam segments and the width of the second order segment. The setups of the above parameters that result in the best plan quality were 1.6 and $1.5cm$, respectively, for the phantom used. The analysis was conducted by changing one parameter at a time, this is not practical clinically and the result may only apply to the particular phantom used in this work. Additionally, the width of the second segment at each angle was set to be constant for simplicity. In fact, the width may vary based on the organ and gantry angle geometries, so that the quality of the plan can be maximized. Finally, the relationship of parameter setups for circle shaped PTV and OAR was illustrated in Bratengeier's previous

paper [25, 26], in future it is worth to implement such relationship into Prism.

Recall from the example shown in Section 2.2.3 and the analysis study in Section 4.6, in the case of one OAR surrounded by one PTV, at any given angle there are at most two PTV regions that do not overlap with the OAR. Due to the physical limitations of the MLC leaves, it is not always possible to deliver radiation to both regions at the same time. Therefore, only one region can be irradiated at each gantry angle during one rotation. The question comes to whether it is necessary to double the rotation numbers to deliver the ideal plan or it is sufficient enough to spend half of the time to irradiate only part of the PTV region at each angle. An analysis was performed in this work to compare the two possible plans with regards to time and dosimetry. The results of the phantom study suggested that by doubling the treatment time (i.e. the number of rotations) the homogeneity of the PTV dose coverage may be improved by more than 50% and the OAR can be spared 26% more (refer to Table 4.6).

The optimization process was conducted in MATLAB because of its build-in optimization toolbox. The dose-based objective function has a quadratic form, a so called lambda-value-dose-based objective function was developed in this work in order to increase the flexibility of the generic dose-based objective function. By letting lambda equal to one the optimization includes the entire dose range into the objective function calculation, while only partial dose range is included for the value of lambda less than one. The segment weights of treatment plans were optimized using the dose-based optimization as well as the dose-volume-based optimization. The time consumption of the dose-volume-based optimization was 5 to 6 times longer than the dose-based optimization in the phantom study. The reason is mainly due to the usage of the 2D dose-volume information (i.e. DVH) to search for the dose range for the objective function calculation in the dose-volume-based optimization. The introduction of the lambda value in the lambda-value-dose-based objective function is able to search the dose range in only 1D (dose domain), so the speed of the optimization becomes faster.

It is worth mentioning that due to this dimension reduction, the lambda-value-dose-based optimization does not provide an absolute volume objective. As a result, the optimization may continue although the plan has met the predefined dose-volume objective during the optimization.

Unfortunately, none of the optimization resulted in an objective function of zero. This means no solution is the real optimal solution in this work. From the treatment planning point of view, this may be caused by the poor choice of the dose-volume objectives in the dose-volume-based optimization. There are also two other explanations to it. Firstly, such result may be due to the physical restriction of the radiation delivery, since negative MU is impossible to achieve. This hard constraint of the optimization makes all components of the variable $\mathbf{x}$ in Equation 3.1 positive numbers, such reduction in the acceptable variable space filters out all the negative values of $\mathbf{x}$ in turn reduces the chance to find the solution that gives null result of the objective function. Secondly, the optimum search algorithm used in this work is the gradient-descend algorithm, which looking for solutions based on the objective function slope. As discussed in Section 3.5, the choice of the starting point affects the result of the search significantly. If there is local minimum along the descend gradient between the starting point and the global minimum, the gradient search will be trapped at the local minimum. Therefore, the none-zero result of the objective calculation may

also indicate that the optimization is trapped at a local minimum. Both of the above two reasons can cause the positive value of the objective calculation, the former one is impossible to change at the moment since the negative radiation is not physically possible. However, the possibility of trapping at a local minimum due to the gradient-descent search algorithm can be reduced by two means, random starting points and stochastic algorithm. In this work, the optimization iterated for many times and each time started from a randomly generated starting point. This method aims to reduce the possibility of getting trapped at local minima by exploring a larger solution space. The second way to avoid trapping at local minimum is to use a stochastic algorithm, such as simulated annealing algorithm, to search for the optimal solution. The simulated annealing was not used in this work, but its potential of avoiding the local minimum encourages that it is worth to be implemented in future work.

The second beam segment width was fixed as a constant for all gantry angles in this work, but this width can in fact be a function of gantry angle. By optimizing the width of the second segment with regards to the organ geometry, the quality of the plan may be improved. This required further study in determining the effect of the second segment width on the quality of the plan.

Finally, the 2-step IMAT treatment plans were generated on a clinical case comparing with the conventional arc therapy. After the segment weight optimization, the DVH was plotted for each plan. Regardless to the type of objective function used, the 2-step IMAT plans were more uniform than the conventional arc therapy in the PTV coverage while the OAR was generally spared better at the same time. The 2-step IMAT plans were able to improve the homogeneity of the PTV doses by about 40% to 50%. The dose distributions on the transverse plane showed that 2-step IMAT was able to significantly reduce the "hot spot" around the PTV. However, in the 2-step IMAT plans some parts of the lung received a high doses after the optimization. This is mainly because the current beam portal shaping program only works for two organs in total and the optimization did not take the lung into consideration. Once the above two problems are addressed by implementing multiple organs in both the segment generation process and the optimization and by increasing computer memory, the 2-step IMAT implementation will be able to deliver treatment plans with even better quality.

7.2 Conclusion

The 2-step IMAT that was introduced by Bratengeier has been implemented for the first time into the Prism TPS. The beam portal shaping process was developed as an automatic process. The treatment plan optimization programs using dose-based and dose-volume-based objective function were developed in MATLAB to improve the quality of the treatment plan. In this work, the dose-based optimization was performed using the so-called lambda-value-dose-based objective function in order to increase the flexibility of the optimization. The implementation of the 2-step IMAT technique into the clinical case indicated that the 2-step IMAT is feasible. The comparison between the conventional arc therapy and 2-step IMAT in the clinical case analysis demonstrated the advantage of the 2-step IMAT in the PTV dose uniformity and OAR sparing. There are future work, such as considering more than

two organs during the beam portal shaping process and optimizing segment weights using the simulated annealing algorithm, to improve the 2-step IMAT implementation in order to make it suitable for general clinical cases. In conclusion, the results from this work has shown that 2-step IMAT is a viable technique. The two-beam-segments approximation of the complex intensity profile allows 2-step IMAT to produce a uniform dose coverage while keeping the treatment planning as a simple process.

Appendix A

EPSM-ABEC Conference Abstract

Implementation of 2-Step Intensity Modulated Arc Therapy

Jidi Sun[1], Jürgen Meyer[1], Theam Yong Chew[2]

[1] Department of Physics & Astronomy, University of Canterbury, Christchurch
[2] Lincoln Ventures Ltd, Christchurch

Introduction: Intensity-modulated Arc Therapy (IMAT) allows creating highly conformal treatment plans, which are supposedly superior to conventional intensity-modulated radiation therapy in terms of treatment time and dose conformity [1]. However, planning is complex and the relative benefits are not yet fully understood [2]. In this work we describe the implementation of a simplified technique called 2-step IMAT, which requires two rotations of the gantry [3]. The beam segments for the first rotation are in analogy with a conformal arc, i.e. with one aperture for each gantry angle reflecting the shape of the target volume. The beam segments for the second rotation are narrow segments close to the organ-at-risk (OAR) in order to achieve steep dose gradients on the edge of the tumour adjacent to OARs.

Methods & Materials: 2-step IMAT was implemented into the University of Washington treatment planning system *Prism* using the Common Lisp Programming language. The segments are automatically generated using 3D-anatomy information and ray-tracing. An elliptical phantom was created with a concave planning target volume (PTV) and an OAR. The width of the narrow segments as well as its relative weight was varied in order to optimize the plan for the phantom. A comparison was carried out between a 4-field 3D-conformal plan, conformal arc plan and 2-step IMAT.

Results/Discussion: The 2-step IMAT plan showed the potential of significantly sparing the OAR with regards to the other techniques (see Figure 1). However, the target dose uniformity was not within the -5%/+7% criteria. The slight dose non-uniformity in the target was not unexpected since no beam weight adjustments had been made for the different pathlengths from different gantry angles.

Conclusion: In this proof-of-principle study we have for the first time automated and implemented the process of segment generation for 2-step IMAT and initial results indicated that with this technique it is possible to create highly conformal treatment plans with high dose gradients. To overcome the current limitations implementation of dose-volume

constraint based optimization and further investigations on the effects of beam aperture settings are required.

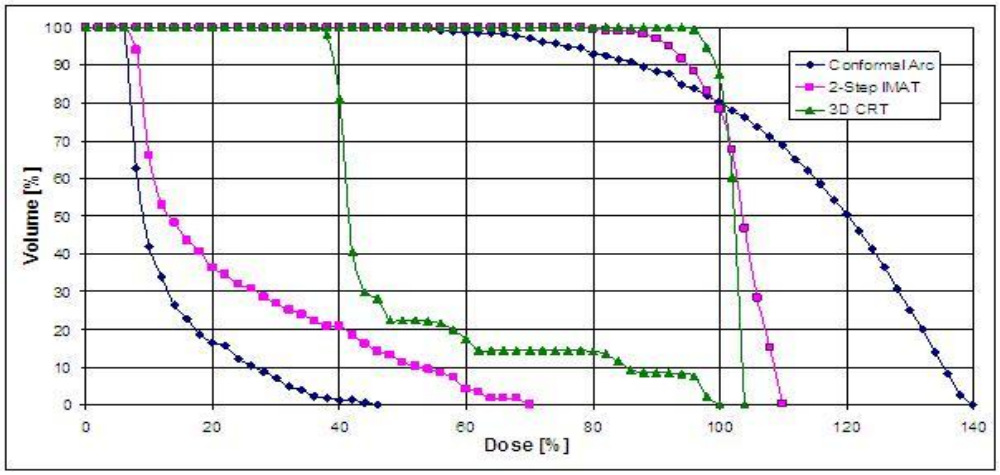

Figure 1: DVH for 3D conformal (triangle), single arc (diamond) and 2-step IMAT (square)

Reference:

1.Yu C X. Intensity-modulated Arc Therapy with Dynamic Multileaf Collimation: An Alternative to Tomotherapy. *Physics in Medicine and Biology* 1995; 40:1435-1449.

2. Bortfeld T, Webb S. Reply to 'Comments on Single-Arc IMRT?' *Physics in Medicine and Biology* 2009, 54; L35-L36

3. Bratengeier K. Applications of Two-Step Intensity Modulated Arc Therapy. *Strahlentherapie Und Onkologie* 2001; 177:394-403.

References

[1] S Webb. The physical basis of IMRT and inverse planning. *Br J Radiol*, 76:679–689, 2003.

[2] L W Brady, H-P Heilmann, and M Molls. *New Technologies in Radiation Oncology*. Springer, 2006.

[3] C X Yu. Intensit-modulated arc therapy with dynamic multileaf collimator: an alternative to tomotherapy. *Phys Med Biol*, 40:1435–1449, 1995.

[4] K Bratengeier. Applications of two-step intensity modulated arc therapy. *Strahlenther Onkol*, 177:394–403, 2001.

[5] I Lax and A Brahme. Rotation therapy using a novel high-gradient filter. *Radiology*, 145:473–478, 1982.

[6] J Meyer, S M Hummel, P S Cho, M M Austin-Seymour, and M H Phillips. Automatic selection of non-coplanar beam directions for three-dimensional conformal radiotherapy. *Br J Radiol*, 78:316–327, 2005.

[7] T Bortfeld and S Webb. Single-arc IMRT? *Phys Med Biol*, 54:N9–N20, 2009.

[8] Cancer facts & figures 2008. *American Cancer Society*, 2008.

[9] E B Podgorsak. *Radiation Oncology Physics: A Handbook for Teachers and Students*. International Atomic Energy Agency, 2005.

[10] P Mayles, A Nahum, and C Rosenwald. *Handbook of Radiotherapy Physics Theory and Practice*. Taylor and Francis, 2007.

[11] F M Khan. *The Physics of Radiation Therapy*. Lippincott Williams & Wilkins, 2003.

[12] E E Klein, J Tepper, M Sontag, M Franklin, C Ling, and D Kubo. Technology assessment of multileaf collimator: a north american users survey. *Int J of Radiat Oncol Biol Phys*, 44(3):705–710, 1999.

[13] S Takahashi. Conformation radiotherapy: rotation techniques as applied to radiography and radiotherapy of cancer. *Acta Radiol*, Suppl 242:1–142, 1965.

[14] J M Galvin, A R Smith, R D Moeller, R L Goodman, W D Powlis, L J Solin, B Michael, M Needham, C J Huntzinger, and M M Kligerman. Evaluation of multileaf collimator design for a photon beam. *Int J Radiat Oncol Biol Phys*, 23:789–801, 1992.

[15] W F A R Verbakel, S Senan, F J Lagerwaard, J P Cuijpers, and B J Slotman. Comments on 'single-arc IMRT?'. *Phys Med Biol*, 54:L31–L34, 2009.

[16] K Otto. Letter to the editor on 'single-arc IMRT?'. *Phys Med Biol*, 54:L37–L41, 2009.

[17] G Tang, M A Earl, and C X Yu. Variable dose rate single-arc imat delivered with a constant dose rate and variable angular spacing. *Phys Med Biol*, 54:6439–6456, 2009.

[18] T Bortfeld and S Webb. Reply to 'comments on 'single-arc IMRT?". *Phys Med Biol*, 54:L35–L36, 2009.

[19] T Bortfeld and S Webb. Reply to 'letter to the editor on 'single-arc IMRT?". *Phys Med Biol*, 54:L43–L44, 2009.

[20] S Webb and D McQuaid. Some considerations concerning volume-modulated arc therapy: a stepping stone towards a general theory. *Phys Med Biol*, 54:4345–4360, 2009.

[21] L Cozzi, K A Dinshaw, S K Shrivastava, U Mahantshetty, R Engineer, D D Deshpande, S V Jamema, E Vanetti, A Clivio, G Nicolini, and A Fogliata. A treatment planning study comparing volumetric arc modulation with rapidarc and fixed field IMRT for cervix uteri radiotherapy. *Radiother and Oncol*, 89:180–191, 2008.

[22] L Ma, C X Yu, M Earl, T Holmes, M Sarfaraz, X A Li, D Shepard, P Amin, S DiBiase, M Suntharalingam, and C Mansfield. Optimized intensity-modulated arc therapy for prostate cancer treatment. *Int J Cancer (Radiat Oncol Invest)*, 96:379–384, 2001.

[23] W Duthoy, W D Gersem, K Vergote, T Boterberg, C Derie, P Smeets, C D Wagter, and W D Neve. Clinical implementation of intensity-modulated arc therapy (IMAT) for rectal cancer. *Int J Radiation Oncology Biol Phys*, 60:794–806, 2004.

[24] J L Bedford, V N Hansen, A McNair, A H Aitken, J E C Brock, A P Warrington, and M Brada. Treatment of lung cancer using volumetric modulated arc therapy and image guidance: a case study. *Acta Oncologica*, 47:1438–1443, 2008.

[25] K Bratengeier. 2-step IMAT and 2-step IMRT: a geometrical approach. *Med Phys*, 32:777–785, 2005.

[26] K Bratengeier. 2-step IMAT and 2-step IMRT in three dimensions. *Med Phys*, 32:3849–3861, 2005.

[27] K Bratengeier, M Guckenberger, J Meyer, G Müller, L Pfreundner, F Schwab, and M Flentje. A comparison between 2-step IMRT and conventional IMRT planning. *Radiother and Oncol*, 84:298–306, 2007.

[28] K Bratengeier, J Meyer, and M Flentje. Pre-segmented 2-step IMRT with subsequent direct machine parameter optimisation - a planning study. *Radiation Oncology*, 3, 2008.

[29] K Bratengeier, J Meyer, F Schwab, D Vordermark, and M Flentje. Steep dose gradients for simultaneous integrated boost IMRT. *Z Med Phys*, 19:129–135, 2009.

[30] A Brahme, J-E Roos, and I Lax. Solution of an integral equation encountered in rotation therapy. *Phys Med Biol*, 27(10):1221–1229, 1982.

[31] J Meyer, B Hartmann, and I Kalet. A 'learning-by-doing' treatment planning tutorial for medical physicists. *Australas Phys Eng Sci Med*, 32(2):112–117, 2009.

[32] K J Sullivan, I J Kalet, and D Notkin. Evaluating the mediator method: Prism as a case study. *IEEE Transaction on Software Engineering*, 22(8):563–579, 1996.

[33] I J Kalet, G D Young, R S Giansiracusa, P S Cho, and J P Jacky. Prism dose computation methods version 1.3 technical report 2000-01-01. Technical report, Radiation Oncology Department, University of Washington, 2000.

[34] I J Kalet. Prism user's reference manual version 1.5 technical report 2009-06-01. Technical report, Radiation Oncology Department, University of Washington, 2009.

[35] I J Kalet, M H Phillips, R S Giansiracusa, and J Jacky. Prism system implementation version 1.3 technical report 2000. Technical report, Radiation Oncology Department, University of Washington, 2000.

[36] H Parsai, M H Phillips, P S Cho, H Kippenes, P Gavin, and D Axen. Verification of dynamic intensity-modulated beam deliveries in canine subjects. *Med Phys*, 28(11):2198–2208, 2001.

[37] R S Giansiracusa and I J Kalet. Prism/DICOM coordinate definitions and interconversion technical report 2003-08-01. Technical report, Radiation Oncology Department, University of Washington, 2003.

[38] Q Wu and R Mohan. Algorithms and functionality of an intensity modulated radiotherapy optimization system. *Med Phys*, 27(4):701–711, 2000.

[39] Q Wu and R Mohan. Multiple local minima in IMRT optimization based on dose-volume criteria. *Med Phys*, 29(7):1514–1527, 2002.

[40] C Thieke, T Bortfeld, A Niemierko, and A Nill. From physical dose constraints to equivalent uniform dose constraints in inverse radiotherapy planning. *Med Phys*, 30(9):2332–2339, 2003.

[41] Q Hou, J Wang, Y Chen, and J M Galvin. An optimization algorithm for intensity moduated radiotherapy - the simulated dynamics with dose-volume constraints. *Med Phys*, 30(1):61–68, 2003.

[42] F V Heuvel. Decomposition analysis of differential dose volume histograms. *Med Phys*, 33(2):297–307, 2006.

[43] C Schinkel, P Stavrev, N Stavreva, and B G Fallone. A theoretical approach to the problem of dose-volume constraint estimation and their impact on the dose-volume histogram selection. *Med Phys*, 33(9):3444–3459, 2006.

[44] G T Y Chen, M M Austin-Seymour, J R Castro, J M Collier, J T Lyman, S Pitluck, W M Saunders, and S R Zink. Dose volume histograms in treatment planning evaluation of carcinoma of the pancreas. In *Proceedings of the Eighth International Conference on Uses of Computers in Radiation Therapy*, pages 264–268. IEEE, IEEE Computer Society Press, 1984.

[45] R E Drzymala, R Mohan, M S Brwester, J Chu, M Goitein, W Harms, and M Urie. Dose volume histograms. *Int J Radiat Oncol Biol Phys*, 21:71–78, 1991.

[46] A Niemierko and M Goitein. Random sampling for evaluating treatment plans. *Med Phys*, 17:753–762, 1990.

[47] H M Kooy, L A Nedzi, E Alexander III, J S Loeffler, and R J Ledoux. Dose-volume histogram computations for small intracranial volumes. *Med Phys*, 20:755–760, 1993.

[48] J T McClave and T Sincich. *Statistics*. Pearson Education International, 2003.

[49] S Webb. *Intensity-Modulated Radiation Therapy*. Institute of Physics, 2002.

[50] X S Yang. *Introduction to Computational Mathematics*. World Scientific, 2008.

[51] M A Bhatti. *Practical Optimization Methods with Mathematica Application*. Springer, 2000.

[52] D Kincaid and W Cheney. *Numerical Analysis: Mathematics of Scientific Computing*. Thomson Learning, 2002.

[53] S P Han. A globally convergent method for nonlinear programming. *Journal of optimization theory and application*, page 297, 1977.

[54] J Sun, J Meyer, and T Y Chew. Implementation of 2-step intensity modulated arc therapy. In *Engineering and Physical Science in Medicine & the Australian Biomedical Engineering College Conference*, 2009.

[55] D Wolff, F Stieler, G Welzel, F Lorenz, Y Abo-Madyan, S Mai, C Herskind, M Polednik, V Steil, F Wenz, and F Lohr. Volumetric modulated arc therapy (VMAT) vs. serial tomotherapy, step-and-shoot IMRT and 3D-conformal RT for treatment of prostate cancer. *Radiother and Oncol*, 93(2):226–233, 2009.